All Theses and Dissertations

2015-01-01

Fluorescence Imaging of Analyte Profiles in an Inductively Coupled Plasma with Laser Ablation as a Sample Introduction Source

Lance Moses

Brigham Young University - Provo

Follow this and additional works at: https://scholarsarchive.byu.edu/etd

Part of the Biochemistry Commons, and the Chemistry Commons

Fluorescence Imaging of Analyte Profiles in an Inductively Coupled Plasma with

Laser Ablation as a Sample Introduction Source

Lance Moses

A dissertation submitted to the faculty of
Brigham Young University
in partial fulfillment of the requirements for the degree of

Doctor of Philosophy

Paul B. Farnsworth, Chair
David V. Dearden
Steven R. Goates
James E. Patterson
Ross L. Spencer

Department of Chemistry and Biochemistry

Brigham Young University

January 2015

ABSTRACT

Fluorescence Imaging of Analyte Profiles in an Inductively Coupled Plasma with
Laser Ablation as a Sample Introduction Source

Lance Moses
Department of Chemistry and Biochemistry, BYU
Doctor of Philosophy

Laser ablation inductively coupled plasma mass spectrometry (LA-ICP-MS) has risen to among the top tier techniques for the direct analysis of solid samples. However, significant problems remain that must be solved to achieve the full analytical potential of LA-ICP-MS. Inefficient conversion of aerosol to ions within the ICP or transmission through the MS interface may decrease precision, sensitivity, and/or accuracy. Although fundamental mechanisms that govern ion production and transmission have been studied extensively in solution-nebulization (SN) ICP-MS instruments, significant gaps in our understanding remain. Furthermore, it is unclear to what extent differences between the aerosols generated during SN and LA influence either ion production or transmission. In this work, I initially investigated differences in the spatial distributions of Ca, Ba, and Sc ions generated by LA and SN using high-resolution LIF imaging. Ions formed from aerosol generated by LA at low fluence were distributed over much greater axial and narrower radial distances than SN aerosol. Additionally, I investigated the effects of solvent, laser fluence, and ablation atmosphere (He vs Ar) on ion distributions in the ICP. Unlike solvent, changing laser fluence and ablation atmosphere produced considerable changes in the ion signal intensity and spatial distribution during LA. At greater laser fluence, the radial distance over which ions were distributed dramatically increased. Surprisingly, when helium was mixed with argon as carrier gas, ion signals decreased. Many of these effects were assumed to be related to changes in the number and size of particles generated during LA. In a follow-up study, relative contributions to ion densities in the ICP from particles of different sizes were investigated. LIF images were recorded while filtering particles above a threshold size on-line. Micron-sized particles contributed the majority of ions formed in the ICP. For Ba, Ca, and Sc, differences in the axial position where nanometer- and micron-sized particles vaporized were 2, 1, and less than 1 mm, respectively. I also performed experiments to identify changes in the ion signal related to changing ablation conditions vs. changing ICP conditions associated with helium additions to the carrier gas. LIF images were recorded during different combinations of He/Ar added upstream and/or downstream of the ablation cell. Changes in the ion signal during ablation in helium vs argon did not always match expectations based on changes in particle numbers and sizes measured with SEM. The results force re-examination of some of the fundamental assumptions about the effect of carrier gas composition on the performance of LA-ICP-MS. The research described in this dissertation provides valuable insight into fundamental aspects of key ICP processes related to LA generated aerosol.

Keywords: Laser ablation, Inductively coupled plasma, Helium, Particle size

ACKNOWLEDGEMENTS

TABLE OF CONTENTS

1   INTRODUCTION

1.1   Introduction to laser ablation inductively coupled plasma mass spectrometry

Laser ablation inductively coupled plasma mass spectrometry (LA-ICP-MS) is a widely used analytical technique for rapid, trace-elemental and isotope-ratio analysis of solid samples. Since first being introduced in 1985 [1], LA-ICP-MS has gained widespread popularity and increased applications in numerous fields of study, such as geology, forensics, counterfeit detection, material sciences, biology, and medicine [2-7]. LA sampling offers numerous advantages over traditional solution nebulization (SN) ICP-MS. Most significantly, LA requires little to no sample preparation. Sample preparation techniques, such as acid digestions, often required in SN-ICP-MS, are not only costly, time consuming, and possibly dangerous, but increase the risk of contamination and loss of volatile elements [8]. Additionally, LA offers better spatial resolution (less than 1 μm), sensitivity, and LODs compared to SN-ICP-MS. Finally, the quasi-nondestructive nature of LA, requiring as little as 0.1 μg/s, is appealing for numerous applications [9]. Consequently, as laser technology developed, many began looking towards LA as a possible sample introduction source. However, in practice, especially when matrix-matched standards are unavailable, LA-ICP-MS typically performs far below its potential in terms of sensitivity, precision, and accuracy [10-13].

In SN-ICP-MS, sophisticated methods relying on calibration strategies such as internal standardization, standard addition, and isotope dilution are routinely used to obtain high levels of precision and accuracy [14]. However these strategies are not generally possible for solid samples. And, unfortunately, LA is particularly prone to sample loss and fractionation effects. Off-axis diffusion and incompletely vaporizing particles represent two major sources of sample loss in the ICP, and may both lead to fractionation effects. Both are expected to be more

pronounced for the broad distribution of particle sizes generated during LA, compared to SN. Thus, in cases where matrix-matched standards are unavailable, analysis by LA-ICP-MS is often considered semi-quantitative. Although progress has been made in developing alternative calibration strategies for LA-ICP-MS, they are often laborious, impractical, ineffective, or have limited applications [15-20]. More research is needed to elucidate processes in LA-ICP-MS contributing to sensitivity loss and error. Currently, it is understood that fractionation effects may occur during ablation, aerosol transport, within the ICP, and during transmission from the ICP to the mass analyzer. Although initial attempts to study factors influencing sensitivity and accuracy in LA-ICP-MS focused on the ablation event [21-25], the focus has shifted more recently to ICP processes [26-30].

A major focus in our research group has been characterizing fundamental aspects of ICP processes, including those related to matrix effects, in SN-ICP-MS. Emission [31-37] and laser-induced fluorescence (LIF) [38-43] techniques have been used to probe analyte distributions in the ICP. Results from these efforts complement extensive research done in many other labs on fundamental ICP processes [8, 44-58]. Although the fundamental mechanisms governing the particle-plasma interaction in SN aerosol droplets are likely to operate in LA instruments, significant differences in aerosol properties of the two should not be overlooked. A greater understanding of how differences in the aerosol generated during SN and LA might affect ICP processes is needed to further improve the analytical capabilities of LA-ICP-MS. In this work, significant differences in the spatial distribution of ions formed from SN and LA aerosol are demonstrated using LIF. The effects of key laser ablation parameters—including solvent, laser fluence, and ablation gas environment—on ion distributions were also investigated. Significant progress was made in charactering fundamental aspects of ICP processes related to LA aerosol.

1.2   Fundamental overview of LA-ICP-MS

1.2.1   Laser systems

There has been a tremendous growth in laser technology since 1985, when Gray et al. [1] demonstrated the potential of ruby lasers as a sample introduction technique coupled to ICP-MS. Since then, Nd:YAG, excimer, and more recently Ti-Sapphire lasers have been coupled to ICP-MS [18]. Ablation patterns of these lasers are heavily dependent on wavelength, pulse duration, spot size, fluence, repetition rate, ablation mode, and gas environment [2]. Ideal laser parameters vary widely for different sample types and applications. Wavelengths in the UV range (193, 213, and 266 nm) and femtosecond pulse durations are generally preferred as they favor small particles more suitable for vaporization in the ICP [59, 60]. However, femtosecond lasers are more expensive and do not always ensure superior performance [60-62]. Consequently, Nd:YAG lasers, which are cheap, robust, reliable, and easy to operate, have been the most widely used [18].

In addition to a laser, typical components of a laser ablation system include beam steering and focusing optics, an ablation cell, and transport tubing. A variety of optics has been used to manipulate the output pulse. Beam homogenizing optics that produce a "flat-top" beam profile, compared to a Gaussian profile, improve ablation characteristics [63]. Beam energy attenuators are also commonly used to control the laser fluence. Also, typical ablation systems use a mirror to direct the beam to the sample and a lens to focus the beam near the sample surface. Samples are housed in an air-tight ablation cell mounted to a motorized XYZ stage to perform rastering ablation and allow adjusting of the laser focus. Ablation cells vary widely in design and performance [64-67]. Ideally, the design of the ablation cell and transport tubing maximizes transport efficiency and minimizes wash-out times [65, 66]. Properties that largely determine

aerosol transport efficiencies include: cell volume, laser focus, tubing diameter, tubing length, physiochemical properties of the tube, and gas composition [68-71].

1.2.2 Laser ablation

The chemical and physical mechanisms that govern laser-matter interactions are extremely complex and difficult to study. Presented here is a simplification of light-matter interaction pertaining to particle production in ultra-violet nanosecond laser ablation (UV-ns-LA); a number of detailed reviews have been published [72-76]. Ablation with UV-ns laser pulses is generally considered to operate in two regimes: surface vaporization and phase explosion [77, 78]. During surface vaporization, laser energy is absorbed by free or bound electrons and subsequently leads to excitation of lattice phonons. When phonons relax, they transfer their energy to the lattice. Phonon relaxation is considered instantaneous (0.1 ps) compared to the time-scale of a ns-LA pulse. Melting and vaporization occurs when lattice temperatures exceed the melting and vaporization points of the material. This process dominates when laser pulse energies are just above the ablation threshold energy of the material. Therefore, surface vaporization is considered to be the dominant ablation mechanism at low laser fluence.

Above a second threshold fluence, ablation mechanisms are characterized by an explosion of vapor and liquid droplets, referred to as phase explosion. This follows a process of homogenous nucleation as a material is superheated to a metastable state as it approaches its thermodynamic critical temperature ($\sim 0.9 T_c$) [78, 79]. Both surface vaporization and phase explosion primarily produce spherical particles. In addition to surface vaporization and phase explosion, non-thermal mechanisms of mass removal during ablation have been discussed. "Cleavage fragments" generated through a mechanical shock process, also referred to as exfoliation, have been described [12, 80, 81]. Following mass removal in either regime, pressure

gradients above the ablated surface lead to an expansion of ablated material away from the surface in a plume of material. If there is sufficient energy, a significant amount of the expanding plume will be ionized, leading to the formation of a surface plasma [82]. This may results in plasma shielding, where the tail end of the nanosecond laser pulse's energy is absorbed by the surface plasma through photo-ionization or inverse Bremsstrahlung. The surface plasma not only reduces ablation efficiencies [83, 84], but may lead to aerosol loss as it compresses the expanding plume of aerosol [85]. Particle formation in the expanding plasma, composed of hot atoms, ions, molecules, and particles, occur through complex nucleation and condensation mechanisms [12]. Again, it should be stressed that the predominate mechanisms governing mass removal and particle formation during ablation are highly dependent on properties of the laser, ablated material, and laser system.

1.2.3 Inductively coupled plasma

ICPs are highly efficient sources of ions, generating ions for over 90% of elements, with ionization efficiencies over 90% for elements with ionization potentials below about 8 eV. Non-selective processes, such as electron impact, are considered to be the most likely mechanism for ionization. However, charge transfer and Penning ionization have also been suggested as additional mechanisms. The extent to which each mechanism contributes is still debated by researchers [86]. An ICP has three main components: a radiofrequency (RF) generator, a coupling coil and a torch. The plasma is sustained in a torch composed of three concentric fused silica tubes; the end of the torch is surrounded by an induction coil. An RF generator, typically operating between 700-1500 W, supplies an alternating current at 27 MHz to the induction, or load coil. Argon, which possesses ideal ionization properties, is cheap, and seldom reacts with the sample, is exposed to an electric spark that generates free electrons. High-energy electrons

accelerated in the oscillating magnetic field collide with argon atoms, generating more free electrons and joule heating. The plasma is self-sustaining when the temperature reaches the ionization temperature of the gas. Additional argon flowing through the outer section of the torch acts to contain the plasma, protecting the surrounding tubing from the intense heat. The temperature is not distributed uniformly throughout the plasma. The outermost region of the plasma, that portion nearest the outer walls of the torch, is the hottest, reaching temperatures as high as 10,000 K. The axial channel, the innermost region of the plasma where the sample is introduced, is much cooler, with temperatures between 5000 and 7000 K.

Particles entering the axial channel begin vaporization in the preheating zone (PHZ) [87]. These species then enter the initial radiation zone (IRZ) where atomization occurs. Ideally, particles are completely atomized in the IRZ and form ions just upstream from the sampling cone in the normal analytical zone (NAZ). These zones represent ideal patterns of ionization within the plasma; actual patterns are highly dependent on variations in particles and plasma properties.

1.2.4 Interfacial region

Although the focus of this work pertains to processes that occur in the ICP, a brief discussion of ion transmission through the vacuum interface of the mass analyzer will be instructive. The interface regions are defined by two concentric metal cones, the sampling cone and the skimmer cone, most commonly made of nickel or platinum. Ions first enter the sampler cone orifice, typically 1 mm in diameter, ideally positioned in the NAZ. Changes in ICP conditions due to the presence of the cooled sampling cone are not trivial [43, 88]. Lower electron and gas-kinetic temperatures in the presence of the metallic sampling cone in the ICP have been reported [89, 90]. Ions passing through the sampler cone into the first vacuum chamber, which is typically around 1 Torr, expand adiabatically. Ion loss during supersonic

expansion [91] in the first vacuum chamber reduces sensitivity and accuracy [41, 92]. A skimmer cone, typically 0.5 millimeters, located a few millimeters behind the sampler cone, collects a portion of the ions that have undergone the supersonic expansion [93, 94]. Ions pass through the skimmer cone and enter the second vacuum chamber, typically held around 10^{-3} Torr. The stream of ions exiting the skimmer cone are extracted, focused, and directed to the mass analyzer by a series of ion optics. The imposed electric fields during extraction are a significant source of ion loss. Also, space charge effects within the ion beam may lead to instrument error [95]. Therefore, transmission of ions through the interface is a significant source of sensitivity loss and error [40, 42]. Processes unique to different mass analyzers used in LA-ICP-MS are beyond the scope of this work and will therefore not be addressed.

1.2.5   Method of investigation

The studies described here were performed using planar laser-induced fluorescence (LIF) to generate a 2D map of analyte ion distributions in the ICP. LIF is a powerful, non-invasive technique to probe species in the gas phase, and has been used to study ICP extensively. A detailed review of LIF can be found in ref [96]. Briefly, a laser source is used to promote a species of interest to an excited state. Fluorescence is emitted as the excited species relaxes to a lower state. Relaxation to non-ground state levels, such as the $^2D_{5/2}$ for Ba II, leads to fluorescence with a longer wavelength than the exciting pulse. The ability to detect fluorescence at wavelengths other than the excitation wavelength is ideal as it reduces background noise. Tunable dye lasers, which can access a large domain of wavelengths with narrow band widths, are commonly used in LIF. Error associated with pulse-to-pulse variations and beam inhomogeneity, common in dye lasers, can be minimized by using pulse energies sufficiently large to saturate the excitation transition. High-resolution profiles can be obtained by imaging the

LIF onto a gated, intensified charge-coupled device (iCCD). Images captured under varying instrumental conditions provide remarkable insight into the fundamental mechanisms that govern the operation of those conditions.

1.3   Background information

1.3.1   Solvent

Qualitative differences between the vaporization, atomization, and ionization patterns in the ICP of aerosol generated during SN and LA have been demonstrated using high-speed digital photography [97]. Solvent, present in SN and not in LA aerosol, is a fundamental difference in aerosol generated by SN and LA. Solvent effects on ICP conditions have been described. Higher plasma temperatures with increasing water load have been reported [98]. Oxygen from water leads to an increased amount of polyatomic oxides and hydroxides formed [99]. This increases the potential for isobaric interferences that contribute to background signal, degrading LODs. However, liquid standards used for calibration during LA sampling have led to improvements in LA-ICP-MS accuracy [100-104]. These improvements were attributed to greater plasma robustness and stability due to more efficient energy transfer between the ICP and aerosol in the presence of water [105].

More recently, Flamigni et al. [106] monitored changes in 2D optical emission spectroscopy (OES) and quadrupole mass spectrometry (QMS) signals for sodium chloride and calcium chloride in "wet" vs "dry" conditions. In "dry" conditions, OES signals from the much less refractory sodium chloride peaked at axial positions upstream from calcium chloride. However, the two profiles merged in "wet" conditions where solvent was introduced with the LA aerosol. They proposed that a greater cooling of the central channel due to the water load, combined with better heat conduction in the presence of gaseous water, led to a steeper

temperature gradient at the point of vaporization. Due to the steeper temperature gradient, particles with different thermodynamic properties experience less variation in penetration depths. Such a merging of vaporization positions could account for the improvements previously reported using liquid standards despite clear differences in the vaporization patterns of SN droplets and "dry" LA aerosol [107].

1.3.2   Helium vs argon

LA is routinely performed in argon and/or helium atmospheres. Compared to argon, helium is lighter, has a higher ionization potential, lower ionization cross section, and higher thermal conductivity [86, 108]. Effects of the carrier gas for a given application are highly dependent on laser and sample properties. Generally, few changes in the ablation rates [109] or particle size distribution (PSD) of aerosol generated during 266 nm-ns-LA have been reported with changes in carrier gas composition [110-112]. Over the nanosecond laser pulse duration, the expanding plume of removed mass dominates the plasma environment. Consequently, effects such as plasma shielding are much less dependent on carrier gas properties than on pulse duration [113]. However, the extent to which carrier gas increases or decreases plasma shielding depends heavily on other instrument parameters such as fluence [114] and wavelength, etc. [115]. For example, reduced surface plasmas leading to greater transport efficiencies in helium, compared to argon, have been reported for 193 nm-ns-LA [112]. In this case, greater dispersion in the expanding aerosol plume in the presence of helium [85], compared to argon, reduced particle deposition associated with compression of the expansion plume [105]. Loss due to deposition not only leads to a decrease in instrument sensitivity [4], but can be a source of non-stoichiometric effects. It is reasonable to assume that ablation characteristics of 266 nm-ns-LA

lead to results similar to that described for 193 nm above for certain samples under certain LA parameters [10].

The effects of helium on ICP environment in SN-ICP-MS have been described [51]. Compared to argon, helium led to significantly higher T_{gas}. Similar reports for LA-ICP-MS have been published [99, 116]. Slightly higher sensitivities, over a larger range of gas flows, have been reported using helium [117]. Also, better detection efficiencies obtained in helium have been attributed to more efficient ion production and transmission in the ICP-MS [118]. Flamigni et al. [119] found that particles had greater velocities, described as an "expansion-driven acceleration" at mixtures of He/Ar over 50%. Wang et al. [120] reported wider radial profiles obtained when adding helium.

1.3.3   Particle size effects

For both metals [121-123] and glasses [124, 125], 266 nm-ns-LA is well known to produce aerosol of a broad PSD, ranging from 10 nm to 10 μm. Common techniques to measure PSDs include differential mobility analyzer (DMA), optical particle counter (OPC), and off-line imaging techniques such as scanning electron microscopy (SEM) [76]. Although DMA and OPC provide fast, on-line quantitative results, they both suffer from limitations, most notably an upper size limit around 1 μm [126]. The omission of micron-sized particles in many discussions may be significant given the number of micron-sized particles observed using SEM of impacted particles [111, 127]. Broad PSDs are problematic for ICP-MS for a number of reasons. First, broad PSDs commonly lead to decreased sensitivity due to particle-size-related sample loss during transport to the ICP or transmission through the interface. During transport to the ICP, deposition due to diffusion of low nanometer-sized particles and gravitational settling of micron-sized particles may occur. Within the ICP, loss due to incompletely vaporizing particles has also

been well documented. The upper size limit of particles that will completely vaporize in the ICP depends on a number of instrument parameters (RF power, gas flow, sampling depth, etc.) and thermodynamic properties of the particle [128]. Not surprisingly, estimates have also varied. Kuhn et al. determined upper-size limits for completely vaporizing particles for glass to be between 90 nm and 150 nm [30]. Jackson et al. reported estimates from 250-500 nm [129].

Though less studied, there has been evidence that local cooling in the plasma due to large particles, or other mass load related effects, lead to fractionation processes in the ICP [120, 130]. Increasing the plasma temperature with the use of higher RF power or He addition, may reduce the number of incompletely vaporizing particles, but will also lead to greater loss due to off-axis diffusion. Sample loss may lead to fractionation effects, which reduce accuracy. In cases where particle composition varies within the PSD [62, 107, 131-134], particle-size-related loss through either deposition during transport [107, 122] or vaporization in the ICP [129, 135], leads to non-representative sampling. Additionally, mass-dependent off-axis diffusion in the ICP, or preferential vaporization, atomization, or ionization of less refractory elements are also possible sources of fractionation effects and error. Although significant progress has been made reducing sample loss during aerosol transport to the ICP, ensuring efficient, stoichiometric transmission of ions generated from aerosol of a broad PSD through the ICP interface remains a major obstacle in 266 nm-ns-LA-ICP-MS.

1.3.4 Laser fluence

Laser fluence is another instrument parameter that can significantly affect instrument performance. Fluence heavily influences fundamental mechanisms governing light-material interactions [136, 137] and plume expansion [114, 138]. As discussed in section 1.2.2., at laser fluences near the ablation threshold, thermal processes lead to selective vaporization [10].

Therefore, fluences well above the ablation threshold are preferred [21, 102]. In fact, it has been

shown that similar performance can be achieved at any wavelength if the fluence is optimized

[25, 139]. There have been a number of indications that improvements at higher fluences are not

related to changes in the PSD [102].

1.4 References

[1] A.L. Gray, Solid sample introduction by laser ablation for inductively coupled plasma source mass spectrometry, Analyst, 110 (1985) 551-556.
[2] D. Günther, B. Hattendorf, Solid sample analysis using laser ablation inductively coupled plasma mass spectrometry, TrAC Trends in Analytical Chemistry, 24 (2005) 255-265.
[3] J. Sabine Becker, Imaging of metals in biological tissue by laser ablation inductively coupled plasma mass spectrometry (LA–ICP–MS): state of the art and future developments, Journal of Mass Spectrometry, 48 (2013) 255-268.
[4] N.J.G. Pearce, W.T. Perkins, J.A. Westgate, S.C. Wade, Trace-element microanalysis by LA-ICP-MS: The quest for comprehensive chemical characterisation of single, sub-10 μm volcanic glass shards, Quaternary International, 246 (2011) 57-81.
[5] B. Giussani, D. Monticelli, L. Rampazzi, Role of laser ablation-inductively coupled plasma-mass spectrometry in cultural heritage research: A review, Anal. Chim. Acta, 635 (2009) 6-21.
[6] K. Smith, K. Horton, R. Watling, N. Scoullar, Detecting art forgeries using LA-ICP-MS incorporating the in situ application of laser-based collection technology, Talanta, 67 (2005) 402-413.
[7] S.F. Durrant, N.I. Ward, Recent biological and environmental applications of laser ablation inductively coupled plasma mass spectrometry (LA-ICP-MS), J. Anal. At. Spectrom., 20 (2005) 821-829.
[8] D. Beauchemin, Inductively Coupled Plasma Mass Spectrometry, Anal. Chem. (Washington, DC, U. S.), 82 (2010) 4786-4810.
[9] M. Guillong, D. Günther, Quasi 'non-destructive' laser ablation-inductively coupled plasma-mass spectrometry fingerprinting of sapphires, Spectrochimica Acta Part B: Atomic Spectroscopy, 56 (2001) 1219-1231.
[10] C.C. Garcia, H. Lindner, K. Niemax, Laser ablation inductively coupled plasma mass spectrometry-current shortcomings, practical suggestions for improving performance, and experiments to guide future development, J. Anal. At. Spectrom., 24 (2009) 14-26.
[11] S.M. Chernonozhkin, S. Goderis, S. Bauters, B. Vekemans, L. Vincze, P. Claeys, F. Vanhaecke, Evaluation of pneumatic nebulization and ns-laser ablation ICP-MS for bulk elemental analysis and 2-dimensional element mapping of iron meteorites, Journal of Analytical Atomic Spectrometry, 29 (2014) 1001-1016.
[12] R.E. Russo, X. Mao, J.J. Gonzalez, V. Zorba, J. Yoo, Laser Ablation in Analytical Chemistry, Analytical Chemistry, 85 (2013) 6162-6177.
[13] M. Walle, J. Koch, D. Tabersky, K. Hametner, N.D. Zhigadlo, S. Katrych, J. Karpinski, D. Gunther, Analyses of lithium-doped and pure magnesium diboride using ultraviolet nano- and femtosecond laser ablation inductively coupled plasma mass spectrometry, Journal of Analytical Atomic Spectrometry, 25 (2010).

[14] C. Agatemor, D. Beauchemin, Matrix effects in inductively coupled plasma mass spectrometry: A review, Analytica Chimica Acta, 706 (2011) 66-83.

[15] H. Traub, M. Wälle, J. Koch, U. Panne, R. Matschat, H. Kipphardt, D. Günther, Evaluation of different calibration strategies for the analysis of pure copper and zinc samples using femtosecond laser ablation ICP-MS, Analytical and Bioanalytical Chemistry, 395 (2009) 1471-1480.

[16] T. Pettke, F. Oberli, A. Audétat, M. Guillong, A.C. Simon, J.J. Hanley, L.M. Klemm, Recent developments in element concentration and isotope ratio analysis of individual fluid inclusions by laser ablation single and multiple collector ICP-MS, Ore Geology Reviews, 44 (2012) 10-38.

[17] Z. Chen, Inter-element fractionation and correction in laser ablation inductively coupled plasma mass spectrometry, J. Anal. At. Spectrom., 14 (1999) 1823-1828.

[18] S. F. Durrant, Laser ablation inductively coupled plasma mass spectrometry: achievements, problems, prospects, Journal of Analytical Atomic Spectrometry, 14 (1999) 1385-1403.

[19] Q. Bian, C.C. Garcia, J. Koch, K. Niemax, Non-matrix matched calibration of major and minor concentrations of Zn and Cu in brass, aluminium and silicate glass using NIR femtosecond laser ablation inductively coupled plasma mass spectrometry, J. Anal. At. Spectrom., 21 (2006) 187-191.

[20] H.-R. Kuhn, D. Gunther, A quantification strategy in laser ablation ICP-MS based on the transported aerosol particle volume determined by optical particle size measurement, Journal of Analytical Atomic Spectrometry, 21 (2006) 1209-1213.

[21] E.F. Cromwell, P. Arrowsmith, Fractionation Effects in Laser Ablation Inductively Coupled Plasma Mass Spectrometry, Applied Spectroscopy, 49 (1995) 1652-1660.

[22] D. Figg, M.S. Kahr, Elemental fractionation of glass using laser ablation inductively coupled plasma mass spectrometry, Appl. Spectrosc., 51 (1997) 1185-1192.

[23] P.M. Outridge, W. Doherty, D.C. Gregoire, Ablative and transport fractionation of trace elements during laser sampling of glass and copper, Spectrochimica Acta Part B: Atomic Spectroscopy, 52 (1997) 2093-2102.

[24] D.J. Figg, J.B. Cross, C. Brink, More investigations into elemental fractionation resulting from laser ablation–inductively coupled plasma–mass spectrometry on glass samples, Applied Surface Science, 127–129 (1998) 287-291.

[25] R.E. Russo, X.L. Mao, O.V. Borisov, H. Liu, Influence of wavelength on fractionation in laser ablation ICP-MS, Journal of Analytical Atomic Spectrometry, 15 (2000) 1115-1120.

[26] M. Guillong, D. Gunther, Effect of particle size distribution on ICP-induced elemental fractionation in laser ablation-inductively coupled plasma-mass spectrometry, Journal of Analytical Atomic Spectrometry, 17 (2002) 831-837.

[27] I. Rodushkin, M.D. Axelsson, D. Malinovsky, D.C. Baxter, Analyte- and matrix-dependent elemental response variations in laser ablation inductively coupled plasma mass spectrometry Part 1. The roles of plasma and ion sampling conditions, Journal of Analytical Atomic Spectrometry, 17 (2002) 1223-1230.

[28] I. Rodushkin, M.D. Axelsson, D. Malinovsky, D.C. Baxter, Analyte- and matrix-dependent elemental response variations in laser ablation inductively coupled plasma mass spectrometry Part 2.Implications for multi-element analyses, Journal of Analytical Atomic Spectrometry, 17 (2002).

[29] M. Guillong, H.-R. Kuhn, D. Gunther, Application of a particle separation device to reduce inductively coupled plasma-enhanced elemental fractionation in laser ablation-inductively

coupled plasma-mass spectrometry, Spectrochim. Acta, Part B, 58B (2003) 211-220.

[30] H.-R. Kuhn, M. Guillong, D. Günther, Size-related vaporisation and ionisation of laser-induced glass particles in the inductively coupled plasma, Analytical and Bioanalytical Chemistry, 378 (2004) 1069-1074.

[31] S.G. Barnhart, P.B. Farnsworth, J.P. Walters, Integrated, microcomputer-controlled, adjustable-waveform spark source for atomic emission spectrometry, Anal. Chem., 53 (1981) 1432-1436.

[32] P.B. Farnsworth, D.A. Rodham, D.W. Ririe, The use of time- and space-resolved emission data for fundamental studies of a pulsed ICP, Spectrochim. Acta, Part B, 42B (1987) 393-406.

[33] M.T. Cicerone, P.B. Farnsworth, A simple, noninvasive method for the measurement of gas flow velocities in an inductively coupled plasma, Spectrochim. Acta, Part B, 44B (1989) 897-907.

[34] A.C. Lazar, P.B. Farnsworth, Characterization of an Inductively Coupled Plasma with Xylene Solutions Introduced as Monodisperse Aerosols, Anal. Chem., 69 (1997) 3921-3929.

[35] A.C. Lazar, P.B. Farnsworth, Investigation of the analytical performance of an MDMI-ICP-AES system, Appl. Spectrosc., 51 (1997) 617-624.

[36] A.C. Lazar, P.B. Farnsworth, Characterization of an inductively coupled plasma with xylene solutions introduced as monodisperse aerosols, Anal Chem, 69 (1997) 3921-3929.

[37] A.C. Lazar, P.B. Farnsworth, Matrix effect studies in the inductively coupled plasma with monodisperse droplets. Part I: the influence of matrix on the vertical analyte emission profile, Appl. Spectrosc., 53 (1999) 457-464.

[38] A.C. Lazar, P.B. Farnsworth, Matrix Effect Studies in the Inductively Coupled Plasma with Monodisperse Droplets. Part II: The Influence of Matrix on Spatially Integrated Ion Density, Applied Spectroscopy, 53 (1999) 465-470.

[39] J.H. Macedone, D.J. Gammon, P.B. Farnsworth, Factors affecting analyte transport through the sampling orifice of an inductively coupled plasma mass spectrometer, Spectrochim. Acta, Part B, 56B (2001) 1687-1695.

[40] J.H. MacEdone, A.A. Mills, P.B. Farnsworth, Optical measurements of ion trajectories through the vacuum interface of an inductively coupled plasma mass spectrometer, Appl Spectrosc, 58 (2004) 463-467.

[41] J.H. Macedone, P.B. Farnsworth, Changes in plasma composition during the expansion into the first vacuum stage of an inductively coupled plasma mass spectrometer, Spectrochimica Acta Part B: Atomic Spectroscopy, 61 (2006) 1031-1038.

[42] A.A. Mills, J.H. Macedone, P.B. Farnsworth, High resolution imaging of barium ions and atoms near the sampling cone of an inductively coupled plasma mass spectrometer, Spectrochimica Acta Part B: Atomic Spectroscopy, 61 (2006) 1039-1049.

[43] H. Ma, N. Taylor, P.B. Farnsworth, The effect of the sampling interface on spatial distributions of barium ions and atoms in an inductively coupled plasma ion source, Spectrochimica Acta Part B: Atomic Spectroscopy, 64 (2009) 384-391.

[44] J.W. Olesik, Peer Reviewed: Fundamental Research in ICP-OES and ICPMS, Analytical Chemistry, 68 (1996) 469A-474A.

[45] J.W. Olesik, Investigating the fate of individual sample droplets in inductively coupled plasmas, Appl. Spectrosc., 51 (1997) 158A-175A.

[46] J.W. Olesik, J.A. Kinzer, G.J. McGowan, Observation of Atom and Ion Clouds Produced From Single Droplets of Sample in Inductively Coupled Plasmas by Optical Emission and Laser-Induced Fluorescence Imaging, Applied Spectroscopy, 51 (1997) 607-616.

[47] J.W. Olesik, J.A. Kinzer, Measurement of monodisperse droplet desolvation in an inductively coupled plasma using droplet size dependent peaks in Mie scattering intensity, Spectrochim. Acta, Part B, 61B (2006) 696-704.

[48] K. Niemax, Considerations about the detection efficiency in inductively coupled plasma mass spectrometry, Spectrochim. Acta, Part B, 76 (2012) 65-69.

[49] A. Murtazin, S. Groh, K. Niemax, Investigation of sample introduction- and plasma-related matrix effects in inductively coupled plasma spectrometry applying single analyte droplet and particle injection, Spectrochim. Acta, Part B, 67 (2012) 3-16.

[50] G.M. Hieftje, G.D. Rayson, J.W. Olesik, A steady-state approach to excitation mechanisms in the ICP, Spectrochim. Acta, Part B, 40B (1985) 167-176.

[51] N.N. Sesi, A. Mackenzie, K.E. Shanks, P. Yang, G.M. Hieftje, Fundamental studies of mixed-gas inductively coupled plasmas, Spectrochimica Acta Part B: Atomic Spectroscopy, 49 (1994) 1259-1282.

[52] N.N. Sesi, G.M. Hieftje, Studies into the interelement matrix effect in inductively coupled plasma spectrometry, Spectrochim. Acta, Part B, 51B (1996) 1601-1628.

[53] I.I. Stewart, C.E. Hensman, J.W. Olesik, Influence of Gas Sampling on Analyte Transport within the ICP and Ion Sampling for ICP-MS Studied Using Individual, Isolated Sample Droplets, Applied Spectroscopy, 54 (2000) 164-174.

[54] G.C.Y. Chan, W.T. Chan, X. Mao, R.E. Russo, Investigation of matrix effects in inductively coupled plasma-atomic emission spectroscopy using laser ablation and solution nebulization - effect of second ionization potential, Spectrochim. Acta, Part B, 56B (2001) 77-92.

[55] B. Hattendorf, D. Gunther, Experimental evidence for the formation of doubly charged oxide and hydroxide ions in inductively coupled plasma mass spectrometry, Fresenius Journal of Analytical Chemistry, 370 (2001) 483-487.

[56] G.C.Y. Chan, W.-T. Chan, Plasma-related matrix effects in inductively coupled plasma—atomic emission spectrometry by group I and group II matrix-elements, Spectrochimica Acta Part B: Atomic Spectroscopy, 58 (2003) 1301-1317.

[57] G.C.Y. Chan, G.M. Hieftje, Experimental evidence of state-selective charge transfer in inductively coupled plasma -atomic emission spectrometry, Spectrochim. Acta, Part B, 59B (2004) 1007-1020.

[58] G.C.Y. Chan, G.M. Hieftje, Using matrix effects as a probe for the study of the charge-transfer mechanism in inductively coupled plasma-atomic emission spectrometry, Spectrochim. Acta, Part B, 59B (2004) 163-183.

[59] J. Pisonero, D. Gunther, femtosecond laser ablation inductively coupled plasma mass spectrometry: fundamentals and capabilities for depth profiling analysis, Mass Spectrometry Reviews, 27 (2008) 609-623.

[60] J. Koch, D. Günther, Femtosecond laser ablation inductively coupled plasma mass spectrometry: achievements and remaining problems, Analytical and Bioanalytical Chemistry, 387 (2007) 149-153.

[61] M. Ohata, D. Tabersky, R. Glaus, J. Koch, B. Hattendorf, D. Gunther, Comparison of 795 nm and 265 nm femtosecond and 193 nm nanosecond laser ablation inductively coupled plasma mass spectrometry for the quantitative multi-element analysis of glass materials, Journal of Analytical Atomic Spectrometry, (2014).

[62] R. Glaus, R. Kaegi, F. Krumeich, D. Günther, Phenomenological studies on structure and elemental composition of nanosecond and femtosecond laser-generated aerosols with implications on laser ablation inductively coupled plasma mass spectrometry, Spectrochimica

Acta Part B: Atomic Spectroscopy, 65 (2010) 812-822.

[63] M. Guillong, I. Horn, D. Gunther, Capabilities of a homogenized 266 nm Nd : YAG laser ablation system for LA-ICP-MS, Journal of Analytical Atomic Spectrometry, 17 (2002) 8-14.

[64] D. Bleiner, A. Bogaerts, Computer simulations of sample chambers for laser ablation–inductively coupled plasma spectrometry, Spectrochimica Acta Part B: Atomic Spectroscopy, 62 (2007) 155-168.

[65] M.B. Fricker, D. Kutscher, B. Aeschlimann, J. Frommer, R. Dietiker, J. Bettmer, D. Gunther, High spatial resolution trace element analysis by LA-ICP-MS using a novel ablation cell for multiple or large samples, International Journal of Mass Spectrometry, 307 (2011) 39-45.

[66] H. Lindner, D. Autrique, J. Pisonero, D. Gunther, A. Bogaerts, Numerical simulation analysis of flow patterns and particle transport in the HEAD laser ablation cell with respect to inductively coupled plasma spectrometry, Journal of Analytical Atomic Spectrometry, 25 (2010).

[67] J.M. Cottle, M.S.A. Horstwood, R.R. Parrish, A new approach to single shot laser ablation analysis and its application to in situ Pb/U geochronology, Journal of Analytical Atomic Spectrometry, 24 (2009) 1355-1363.

[68] D. Bleiner, D. Gunther, Theoretical description and experimental observation of aerosol transport processes in laser ablation inductively coupled plasma mass spectrometry, Journal of Analytical Atomic Spectrometry, 16 (2001) 449-456.

[69] M.W. Loewen, A.J.R. Kent, Sources of elemental fractionation and uncertainty during the analysis of semi-volatile metals in silicate glasses using LA-ICP-MS, Journal of Analytical Atomic Spectrometry, 27 (2012) 1502-1508.

[70] R. Kovacs, D. Guenther, Influence of transport tube materials on signal response and drift in laser ablation-inductively coupled plasma-mass spectrometry, J. Anal. At. Spectrom., 23 (2008) 1247-1252.

[71] C.C. Garcia, M. Walle, H. Lindner, J. Koch, K. Niemax, D. Gunther, Femtosecond laser ablation inductively coupled plasma mass spectrometry: Transport efficiencies of aerosols released under argon atmosphere and the importance of the focus position, Spectrochimica Acta Part B-Atomic Spectroscopy, 63 (2008) 271-276.

[72] S.I. Anisimov, B.S. Luk'yanchuk, Selected problems of laser ablation theory, Phys.-Usp., 45 (2002) 293-324.

[73] R.E. Russo, X. Mao, S.S. Mao, Peer Reviewed: The Physics of Laser Ablation in Microchemical Analysis, Analytical Chemistry, 74 (2002) 70 A-77 A.

[74] S.A. Darke, J.F. Tyson, Interaction of laser radiation with solid materials and its significance to analytical spectrometry. A review, Journal of Analytical Atomic Spectrometry, 8 (1993) 145-209.

[75] N.G. Semaltianos, Nanoparticles by Laser Ablation, Critical Reviews in Solid State and Materials Sciences, 35 (2010) 105-124.

[76] R. Hergenroder, Laser-generated aerosols in laser ablation for inductively coupled plasma spectrometry, Spectrochimica Acta Part B-Atomic Spectroscopy, 61 (2006) 284-300.

[77] T.r. Özel, M. Koç, Micro-manufacturing : Design and Manufacturing of Micro-products, Wiley, Hoboken, N.J., 2011.

[78] N.M. Bulgakova, A.V. Bulgakov, Pulsed laser ablation of solids: transition from normal vaporization to phase explosion, Appl. Phys. A: Mater. Sci. Process., 73 (2001) 199-208.

[79] X. Xu, Phase explosion and its time lag in nanosecond laser ablation, Appl. Surf. Sci., 197-198 (2002) 61-66.

[80] S. Chenery, A. Hunt, M. Thompson, Laser ablation of minerals and chemical differentiation

of the ejecta, Journal of Analytical Atomic Spectrometry, 7 (1992) 647.

[81] V. Craciun, D. Craciun, M.C. Bunescu, R. Dabu, I.W. Boyd, Scanning electron microscopy investigation of laser ablated oxide targets, Journal of Physics D: Applied Physics, 32 (1999) 1306.

[82] Q.L. Ma, V. Motto-Ros, W.Q. Lei, M. Boueri, X.S. Bai, L.J. Zheng, H.P. Zeng, J. Yu, Temporal and spatial dynamics of laser-induced aluminum plasma in argon background at atmospheric pressure: Interplay with the ambient gas, Spectrochim. Acta, Part B, 65B (2010) 896-907.

[83] G. Cristoforetti, G. Lorenzetti, P.A. Benedetti, E. Tognoni, S. Legnaioli, V. Palleschi, Effect of laser parameters on plasma shielding in single and double pulse configurations during the ablation of an aluminium target, J. Phys. D: Appl. Phys., 42 (2009) 207/225201-225207/225208.

[84] V. Margetic, A. Pakulev, A. Stockhaus, M. Bolshov, K. Niemax, R. Hergenröder, A comparison of nanosecond and femtosecond laser-induced plasma spectroscopy of brass samples, Spectrochimica Acta Part B: Atomic Spectroscopy, 55 (2000) 1771-1785.

[85] J. Koch, S. Schlamp, T. Rösgen, D. Fliegel, D. Günther, Visualization of aerosol particles generated by near infrared nano- and femtosecond laser ablation, Spectrochimica Acta Part B: Atomic Spectroscopy, 62 (2007) 20-29.

[86] H. Niu, R.S. Houk, Fundamental aspects of ion extraction in inductively coupled plasma mass spectrometry, Spectrochimica Acta Part B: Atomic Spectroscopy, 51 (1996) 779-815.

[87] J.A. Horner, G.C.Y. Chan, S.A. Lehn, G.M. Hieftje, Computerized simulation of solute-particle vaporization in an inductively coupled plasma, Spectrochim. Acta, Part B, 63B (2008) 217-233.

[88] S.A. Lehn, M. Huang, K.A. Warner, G. Gamez, G.M. Hieftje, Spatially resolved ground-state number densities of calcium and strontium ion in an inductively coupled plasma in contact with an inductively coupled plasma mass spectrometry sampling interface, Spectrochimica Acta Part B: Atomic Spectroscopy, 58 (2003) 1647-1662.

[89] S.A. Lehn, K.A. Warner, M. Huang, G.M. Hieftje, Effect of an inductively coupled plasma mass spectrometry sampler interface on electron temperature, electron number density, gas-kinetic temperature and analyte emission intensity upstream in the plasma, Spectrochimica Acta Part B: Atomic Spectroscopy, 57 (2002) 1739-1751.

[90] M. Aghaei, H. Lindner, A. Bogaerts, Effect of a mass spectrometer interface on inductively coupled plasma characteristics: a computational study, Journal of Analytical Atomic Spectrometry, 27 (2012) 604-610.

[91] W.N. Radicic, J.B. Olsen, R.V. Nielson, J.H. Macedone, P.B. Farnsworth, Characterization of the supersonic expansion in the vacuum interface of an inductively coupled plasma mass spectrometer by high-resolution diode laser spectroscopy, Spectrochimica Acta Part B: Atomic Spectroscopy, 61 (2006) 686-695.

[92] P.B. Farnsworth, R.L. Spencer, W.N. Radicic, N. Taylor, J. Macedone, H. Ma, A comparison of ion and atom behavior in the first stage of an inductively coupled plasma mass spectrometer vacuum interface: Evidence of the effect of an ambipolar electric field, Spectrochimica Acta Part B: Atomic Spectroscopy, 64 (2009) 905-910.

[93] B.S. Duersch, P.B. Farnsworth, Characterization of the ion beam inside the skimmer cone of an inductively coupled plasma mass spectrometer by laser excited atomic and ionic fluorescence, Spectrochim. Acta, Part B, 54B (1999) 545-555.

[94] B.S. Duersch, Y. Chen, A. Ciocan, P.B. Farnsworth, Optical measurements of ion density in the second vacuum stage of an inductively coupled plasma mass spectrometer, Spectrochim.

Acta, Part B, 53B (1998) 569-579.

[95] A.J. Edmund, S.D. Bergeson, M. Lyon, N. Taylor, I. Kalinitchenko, P.B. Farnsworth, Evaluation of space charge effects in the second vacuum stage of a commercial inductively coupled plasma mass spectrometer by planar laser-induced fluorescence imaging, Spectrochimica Acta Part B: Atomic Spectroscopy, 76 (2012) 109-118.

[96] N. Bras, Laser Induced Fluorescence, Laser Chemistry, 10 (1990) 405-412.

[97] D.B. Aeschliman, S.J. Bajic, D.P. Baldwin, R.S. Houk, High-speed digital photographic study of an inductively coupled plasma during laser ablation: comparison of dried solution aerosols from a microconcentric nebulizer and solid particles from laser ablation, J. Anal. At. Spectrom., 18 (2003) 1008-1014.

[98] J.B. Olsen, J.H. Macedone, P.B. Farnsworth, Source gas kinetic temperatures in an ICP-MS determined by measurements of the gas velocities in the first vacuum stage, Journal of Analytical Atomic Spectrometry, 21 (2006) 856-860.

[99] T.M. Witte, R.S. Houk, Origins of polyatomic ions in laser ablation-inductively coupled plasma-mass spectrometry: An examination of metal oxide ions and effects of nitrogen and helium in the aerosol gas flow, Spectrochim. Acta, Part B, 69 (2012) 9-19.

[100] M. Walle, J. Koch, D. Gunther, Analysis of brass and silicate glass by femtosecond laser ablation inductively coupled plasma mass spectrometry using liquid standard calibration, Journal of Analytical Atomic Spectrometry, 23 (2008) 1285-1289.

[101] C. O' Connor, B.L. Sharp, P. Evans, On-line additions of aqueous standards for calibration of laser ablation inductively coupled plasma mass spectrometry: theory and comparison of wet and dry plasma conditions, Journal of Analytical Atomic Spectrometry, 21 (2006).

[102] F. Claverie, B. Fernandez, C. Pecheyran, J. Alexis, O.F.X. Donard, Elemental fractionation effects in high repetition rate IR femtosecond laser ablation ICP-MS analysis of glasses, J. Anal. At. Spectrom., 24 (2009) 891-902.

[103] J.S. Becker, C. Pickhardt, H.-J. Dietze, Determination of trace elements in high-purity platinum by laser ablation inductively coupled plasma mass spectrometry using solution calibration, J. Anal. At. Spectrom., 16 (2001) 603-606.

[104] J.J. Leach, L.A. Allen, D.B. Aeschliman, R.S. Houk, Calibration of Laser Ablation Inductively Coupled Plasma Mass Spectrometry Using Standard Additions with Dried Solution Aerosols, Anal. Chem., 71 (1999) 440-445.

[105] D. Gunther, C. A. Heinrich, Enhanced sensitivity in laser ablation-ICP mass spectrometry using helium-argon mixtures as aerosol carrier, Journal of Analytical Atomic Spectrometry, 14 (1999).

[106] L. Flamigni, J. Koch, D. Gunther, The effect of carrier gas humidity on the vaporization of laser-produced aerosols in inductively coupled plasmas, Journal of Analytical Atomic Spectrometry, 29 (2014) 280-286.

[107] J. Koch, I. Feldmann, N. Jakubowski, K. Niemax, Elemental composition of laser ablation aerosol particles deposited in the transport tube to an ICP, Spectrochimica Acta Part B: Atomic Spectroscopy, 57 (2002) 975-985.

[108] A. Fisher, S.J. Hill, Alternative and mixed gas plasmas, in, Blackwell Publishing Ltd., 2007, pp. 226-250.

[109] I. Horn, M. Guillong, D. Gunther, Wavelength dependant ablation rates for metals and silicate glasses using homogenized laser beam profiles - implications for LA-ICP-MS, Applied Surface Science, 182 (2001) 91-102.

[110] X.L. Mao, W.T. Chan, M.A. Shannon, R.E. Russo, Plasma shielding during picosecond

laser sampling of solid materials by ablation in He versus Ar atmosphere, Journal of Applied Physics, 74 (1993) 4915-4922.

[111] H.-R. Kuhn, D. Gunther, The agglomeration state of nanosecond laser-generated aerosol particles entering the ICP, Anal Bioanal Chem, 383 (2005) 434-441.

[112] I. Horn, D. Gunther, The influence of ablation carrier gasses Ar, He and Ne on the particle size distribution and transport efficiencies of laser ablation-induced aerosols: implications for LA-ICP-MS, Appl. Surf. Sci., 207 (2003) 144-157.

[113] R.E. Russo, LASER-ABLATION, Applied Spectroscopy, 49 (1995) A14-A28.

[114] J.-F.Y. Gravel, D. Boudreau, Study by focused shadowgraphy of the effect of laser irradiance on laser-induced plasma formation and ablation rate in various gases, Spectrochim. Acta, Part B, 64B (2009) 56-66.

[115] A.M. Leach, G.M. Hieftje, Factors Affecting the Production of Fast Transient Signals in Single Shot Laser Ablation Inductively Coupled Plasma Mass Spectrometry, Applied Spectroscopy, 56 (2002) 62-69.

[116] H. Lindner, A. Bogaerts, Multi-element model for the simulation of inductively coupled plasmas: Effects of helium addition to the central gas stream, Spectrochimica Acta Part B: Atomic Spectroscopy, 66 (2011) 421-431.

[117] Z. Wang, B. Hattendorf, D. Guenther, Analyte Response in Laser Ablation Inductively Coupled Plasma Mass Spectrometry, J. Am. Soc. Mass Spectrom., 17 (2006) 641-651.

[118] M. Wälle, J. Koch, L. Flamigni, S. Heiroth, T. Lippert, W. Hartung, D. Günther, Detection efficiencies in nano- and femtosecond laser ablation inductively coupled plasma mass spectrometry, Spectrochimica Acta Part B: Atomic Spectroscopy, 64 (2009) 109-112.

[119] L. Flamigni, J. Koch, H. Wiltsche, R. Brogioli, S. Gschwind, D. Guenther, Visualization, velocimetry, and mass spectrometric analysis of engineered and laser-produced particles passing through inductively coupled plasma sources, J. Anal. At. Spectrom., 27 (2012) 619-625.

[120] Z. Wang, B. Hattendorf, D. Guenther, Vaporization and ionization of laser ablation generated aerosols in an inductively coupled plasma mass spectrometer-implications from ion distribution maps, J. Anal. At. Spectrom., 21 (2006) 1143-1151.

[121] N.J. Saetveit, S.J. Bajic, D.P. Baldwin, R.S. Houk, Influence of particle size on fractionation with nanosecond and femtosecond laser ablation in brass by online differential mobility analysis and inductively coupled plasma mass spectrometry, Journal of Analytical Atomic Spectrometry, 23 (2008).

[122] H.-R. Kuhn, D. Günther, Elemental Fractionation Studies in Laser Ablation Inductively Coupled Plasma Mass Spectrometry on Laser-Induced Brass Aerosols, Analytical Chemistry, 75 (2003) 747-753.

[123] J.J. Gonzalez, C. Liu, S.-B. Wen, X. Mao, R.E. Russo, Metal particles produced by laser ablation for ICP-MS measurements, Talanta, 73 (2007) 567-576.

[124] H.-R. Kuhn, D. Gunther, Laser ablation-ICP-MS: particle size dependent elemental composition studies on filter-collected and online measured aerosols from glass, Journal of Analytical Atomic Spectrometry, 19 (2004).

[125] J.J. Gonzalez, C. Liu, S.B. Wen, X. Mao, R.E. Russo, Glass particles produced by laser ablation for ICP-MS measurements, Talanta, 73 (2007) 577-582.

[126] H.-R. Kuhn, J. Koch, R. Hergenroeder, K. Niemax, M. Kalberer, D. Guenther, Evaluation of different techniques for particle size distribution measurements on laser-generated aerosols, J. Anal. At. Spectrom., 20 (2005) 894-900.

[127] D. Bleineru, P. Gasser, Structural features of laser ablation particulate from Si target, as

revealed by focused ion beam technology, Applied Physics A: Materials Science & Processing, 79 (2004) 1019-1022.

[128] M. Holá, V. Konečná, P. Mikuška, J. Kaiser, V. Kanický, Influence of physical properties and chemical composition of sample on formation of aerosol particles generated by nanosecond laser ablation at 213nm, Spectrochimica Acta Part B: Atomic Spectroscopy, 65 (2010) 51-60.

[129] S.E. Jackson, D. Gunther, The nature and sources of laser induced isotopic fractionation in laser ablation-multicollector-inductively coupled plasma-mass spectrometry, Journal of Analytical Atomic Spectrometry, 18 (2003) 205-212.

[130] I. Kroslakova, D. Guenther, Elemental fractionation in laser ablation-inductively coupled plasma-mass spectrometry: evidence for mass load induced matrix effects in the ICP during ablation of a silicate glass, J. Anal. At. Spectrom., 22 (2007) 51-62.

[131] H. Lindner, J. Koch, K. Niemax, Production of Ultrafine Particles by Nanosecond Laser Sampling Using Orthogonal Prepulse Laser Breakdown, Anal. Chem., 77 (2005) 7528-7533.

[132] M.Z. Martin, M.-D. Cheng, R.C. Martin, Aerosol measurement by laser-induced plasma technique: a review, Aerosol Sci. Technol., 31 (1999) 409-421.

[133] J. Koch, A. von Bohlen, R. Hergenroder, K. Niemax, Particle size distributions and compositions of aerosols produced by near-IR femto- and nanosecond laser ablation of brass, Journal of Analytical Atomic Spectrometry, 19 (2004).

[134] Liu, MaoMao, S.S. Mao, R. Greif, R.E. Russo, Particle Size Dependent Chemistry from Laser Ablation of Brass, Analytical Chemistry, 77 (2005) 6687-6691.

[135] P. Weis, H.P. Beck, D. Gunther, Characterizing ablation and aerosol generation during elemental fractionation on absorption modified lithium tetraborate glasses using LA-ICP-MS, Anal Bioanal Chem, 381 (2005) 212-224.

[136] O. Benavides, O. Lebedeva, V. Golikov, Reflection of nanosecond Nd:YAG laser pulses in ablation of metals, Opt. Express, 19 (2011) 21842-21848.

[137] J.S. Becker, D. Tenzler, Studies of LA-ICP-MS on quartz glasses at different wavelengths of a Nd:YAG laser, Fresenius' Journal of Analytical Chemistry, 370 (2001) 637-640.

[138] T.A. Schmitz, J. Koch, D. Guenther, R. Zenobi, Characterization of aerosol plumes in nanosecond laser ablation of molecular solids at atmospheric pressure, Appl. Phys. B: Lasers Opt., 100 (2010) 521-533.

[139] R. Huang, Q. Yu, Q. Tong, W. Hang, J. He, B. Huang, Influence of wavelength, irradiance, and the buffer gas pressure on high irradiance laser ablation and ionization source coupled with an orthogonal Time of Flight Mass Spectrometer, Spectrochimica Acta Part B: Atomic Spectroscopy, 64 (2009) 255-261.

2 Fluorescence imaging of ion distributions in an inductively coupled plasma with laser ablation sample introduction

This chapter has been published with minor modifications in Spectrochimica Acta Part B (http://dx.doi.org/10.1016/j.sab.2014.08.002)

2.1 Introduction

Ion transmission through the vacuum interface in LA-ICP-MS is a critical process that heavily influences instrument performance. For efficient, stoichiometric transmission through the interface, vaporization and particle formation should occur such that subsequent atomization and ionization processes form ions on axis in the NAZ, just upstream from the sampling cone [1-3]. Aerosol vaporization is largely a function of aerosol properties and the ICP environment. Instrument settings, including RF power, sampling distance, gas flow, etc. that regulate the ICP environment have been studied extensively and are commonly optimized to maximize ion transmission. Aerosol properties, mainly size, velocity, and thermodynamic properties, not only influence ion transmission, but also affect the ICP environment [4]. Furthermore, these effects vary widely with sample types. Consequently, experimentally determining an ideal setting for each sample to maximize ion transmission is both challenging and impractical [5]. Although a model that could reliably predict patterns in ion transmission for a given LA-ICP-MS application would eliminate the need to optimize instrumentation experimentally, significant gaps in current LA-ICP-MS theory exist. One such gap, an understanding of vaporization patterns in the ICP that are specific to LA generated aerosol, is the focal point of this work.

Recent research in our lab, often utilizing LIF, has been focused on characterizing ion transmission through the vacuum interface of SN-ICP-MS instruments [2, 3, 6-10]. Because LIF is noninvasive, it is a powerful technique to directly probe analyte species just upstream and downstream from the interface. The LIF imaging experiments cited above have provided

valuable insights into ion transmission through the vacuum interface, complementing findings published by numerous other groups [5]. Although mechanisms controlling ICP processes and ion transmission in SN instruments should also control ICP processes in LA instruments, distinct differences in LA and SN systems motivate research characterizing ion transmission through the interface in LA-ICP-MS instruments. Among these are significant differences in the aerosol produced: the aerosol produced in LA is dry, and the particles LA produces present a much broader distribution of size, morphology, and composition than do most aerosols produced by SN. Water added to the carrier gas downstream from the ablation cell has led to improvements in the analytical performance in LA-ICP-MS [11-13]. These improvements have been attributed to steeper temperature gradients in the ICP that result from improved energy coupling of the RF field in the presence of gaseous water [14]. Conversely, broader distributions of particle sizes produced during LA, ranging anywhere from 10 nm to 10 μm [15], are considered to be a major detriment to LA-ICP-MS performance. Difficulties in ensuring efficient transmission of ions formed from particles of different sizes, which experience very different penetration depths in the ICP, remain a major source of error in LA-ICP-MS.

Aerosols produced by UV-ns-LA systems are especially prone to size-related effects during vaporization. Research characterizing aerosol particles produced from metals [16, 17] and glass [18, 19] with these systems have been reported. Although particles in the range of 100-300 nm predominate both cases, large particles produced by melt splashing contribute to a much greater percentage of aerosol volume in metals than is the case with glasses [20]. Laser fluence plays a major role in the ablation process for both metals and glasses. In general, at greater fluence, ablation rates increase, leading to a greater number of aerosol particles. Decreasing fluence generally leads to a decrease in large particles [21, 22]. Advantages in the analytical performance

of LA-ICP-MS resulting from the addition of helium to the carrier gas are well documented. Improvements to sensitivity, accuracy, and precision have been reported and are generally attributed to improved energy transfer at the ablation site, leading to less particle deposition, an increase in the fraction of small particles transported to the ICP [11, 23], and improvements in the ionization efficiency of the ICP [24]. Carrier gas flow rates not only significantly alter gas temperatures in the central channel of the ICP, but there are also some indications that they influence aerosol production and transport [22]. Given the broad distributions of particle sizes, diverse morphologies, and varied compositions of aerosols produced during LA, optimizing the carrier gas flow rates to maximize ion transmission efficiency presents a serious challenge [25].

In the work presented here we examine the effects of LA parameters on aerosol formation indirectly by imaging distributions of analyte ions in an ICP in the region between the load coil and the sampling cone. This study complements work published by the Günther group, in which they mapped ions in the plasma by moving the plasma with respect to the sampling cone [26]. They were able to look at a wide range of elements, but with limited spatial resolution. Their results were also affected by the fact that each spatial point was sampled from a slightly different plasma, affected by changes in the relative positions of the torch and the sampling cone. In the current work, we examine only three elements, but with the benefit of a measurement technique that is essentially noninvasive, and which simultaneously maps the entire region between the load coil and the sampling cone with 23-μm spatial resolution.

2.2   Experimental

2.2.1   Sample

For the SN experiments, 50 mg L^{-1} solutions of Ba, Ca (J.T. Baker Chemical Co., Phillipsburg, NJ), and Sc (Fluka Analytical, St. Louis, Mo) were prepared from 1000 mg L^{-1}

stock solution of barium nitrate, calcium nitrate, and scandium nitrate, respectively, dissolved in

2% v/v nitric acid. BaF_2 windows (Laser Optex, Beijing, China) and CaF_2 windows (Exuberance

Opto-electronics Technology Co,.Ltd, Beijing, China) were purchased and used for the LA

experiments. A scandium-aluminum alloy (2% wt/wt) sample was provided by AMG Aluminum

(Robards, KY) and used for the LA studies.

2.2.2 ICP

All experiments were performed on a commercial ICP-MS (RedTop, Varian, Mulgrave,

Australia) instrument, extensively modified to accommodate the imaging optics. To allow space

for LIF imaging the RF box, gas box, nebulizer, spray chamber, and igniter assembly were

removed from the instrument and mounted to aluminum plates bolted to a steel A-frame.

Solutions were introduced into a concentric nebulizer (AR30-1-FM04, Glass Expansion, West

Melbourne, Australia) at a flow rate of 1 ml min−1. A Scott-type spray chamber was used at

room temperature. A standard one-piece, low-flow quartz torch, 2.0 mm ID injector, (800-34,

Precision Glassblowing of Colorado, Centennial, CO) was custom cut so that the torch ended 2

mm downstream from the load coil. The torch was shortened to prevent it from optically

interfering with the LIF. The position of the torch with respect to the load coil was not altered

from the manufacturer's settings. A nickel sampling cone (VG-1001-Ni, Spectron, Ventura, CA)

was mounted on a lab-constructed, water-cooled flange, which was in turn mounted to a vacuum

chamber. Two roughing pumps (Trivac D30A, Leybold, Export, PA) were used to create a

vacuum of 1.0 Torr within the vacuum chamber, which mimicked the first vacuum stage of a

working ICP-MS. Because the quadrupole mass spectrometer (QMS) was not used in this

experiment, it and many components related to it were removed completely. A chiller

(Thermoflex3500, Fisher Scientific, Hampton, NH) was used to cool the instrument. For all the

experiments, the RF power was 1300 W, the sampling depth (load coil to sampling cone) was 12 mm, and plasma, auxiliary, and sheath gas were 16.0, 2.0, and 0.2 L min^{-1}, respectively. The sheath gas is a flow of argon that is added to the nebulizer gas flow in a transfer tube between the exit of the spray chamber and the base of the injector tube.

2.2.3 Laser ablation

A pulsed Brilliant B Nd:YAG laser (Quantel, Bozeman, MT) was used for the laser ablation experiments. The output beam was 0.5 cm in diameter and averaged 40 mJ per pulse at factory settings. A high energy variable attenuator (990-0070, Eksma, Vilnius, Lithuania) was used to attenuate the output energy. The knob controlling the angle on the 4ω crystal was also used to adjust output energy. No significant change in the 4-5 ns pulse width or beam shape was observed over the range adjusted. Overall, a range of 0.5 to 40 mJ per pulse was obtained. A high energy mirror was used to reflect the attenuated beam towards a fused silica singlet focusing lens (f=128.9mm at 266 nm) mounted above the sealed ablation cell. A cylindrical ablation cell with a volume of roughly 100 cm^3, pictured in Fig. 2.1, was mounted to an XYZ stage that was controlled by 3 microstepping drivers (OEM 750, Parker Hannifin, Cleveland, OH) controlled by an ACR9000 (Parker Hannifin) control box for rastering capabilities. The laser was fired at 10 Hz and rastered at 0.1 mm s^{-1}. This yielded a steady state of aerosol production with only minor fluctuations based on the ablation position. The laser focal points were adjusted to produce crater diameters of 150 μm on scandium-aluminum alloy samples and 90 μm on the CaF_2 and BaF_2 windows. Also, a thin strip of anodized aluminum attached to a rotary solenoid was used as a shutter to stop ablation without having to disable the laser flashlamp. The LA system was controlled through LabView (National Instruments, Austin, TX). The original gas box that accompanied the Varian ICP-MS was used to control the Ar gas flow supply to the ablation cell.

A separate mass flow controller (5850, Brooks Instruments, Hatfield, PA) was used to control the He gas flow, which was mixed with the Ar upstream from the ablation chamber using a swage T-connector. A 7-mm I.D. tube exiting the ablation cell carried the ablated aerosol to the sheath torch connector of the ICP.
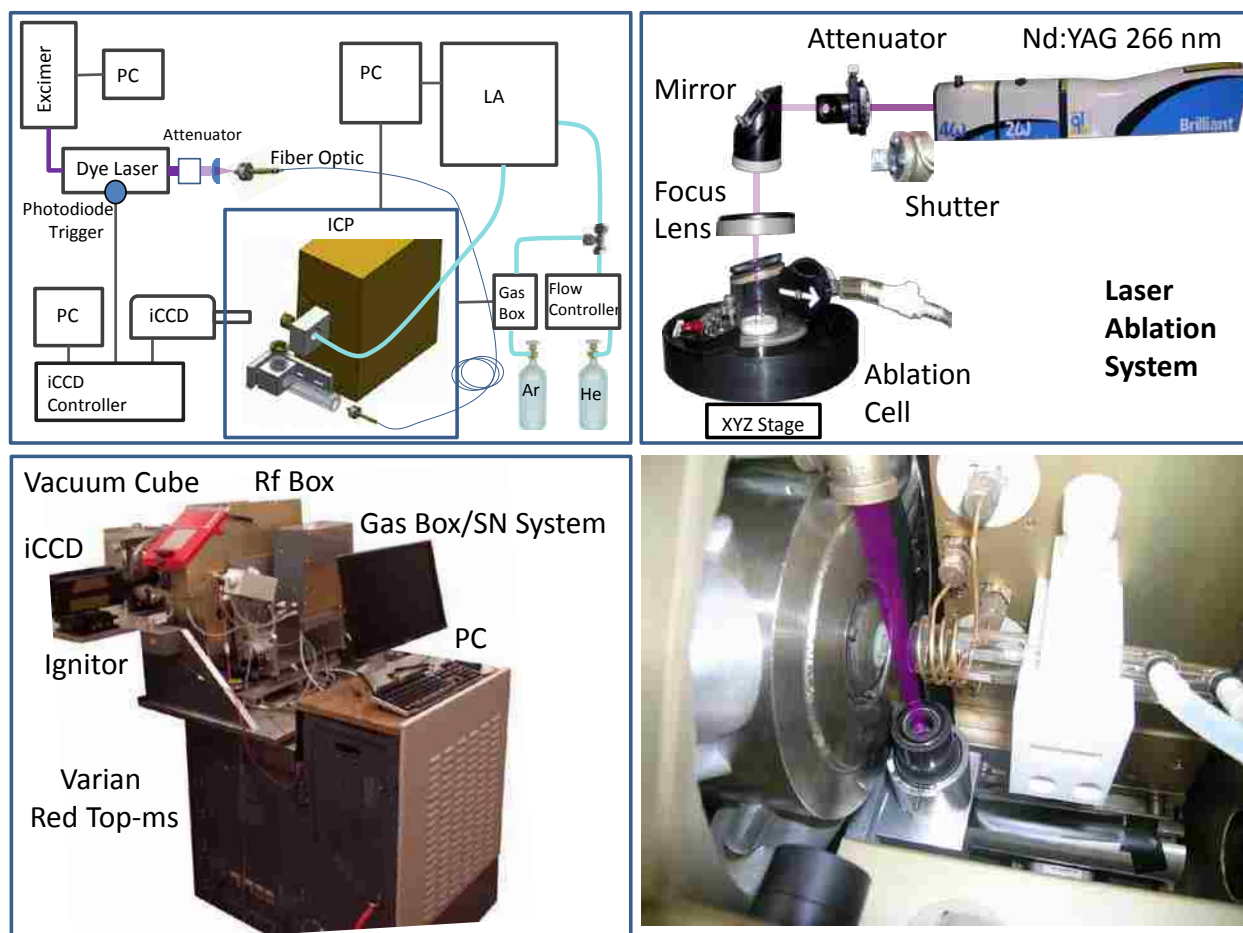
Figure 2.1 *Top left:* General overview of the instrumental setup. *Top right:* Images of the LA system developed for this work. *Bottom left:* An image of the modifications to the Varian ICP-MS. *Bottom right:* An image illustrating the orientation of the planar sheet used for LIF.

2.2.4 Laser induced fluorescence

A XeCl excimer laser (LPX 110, Lambda-Physik, Göttingen, Germany) was used to pump a dye laser (Scanmate 2, Lambda-Physik) tuned to a transition line for the ion being studied. The fluorescence schemes for each ion are presented in Table 2.1. The dye laser energy was adjusted

with a variable attenuator (M 935 10, Newport, Irvine, CA) to slightly above the value required to saturate the transition, ensuring a maximum, stable fluorescence signal with minimum interference from scattered radiation. The output from the attenuator was passed through an optical fiber, then recollimated with a fused silica plano-convex singlet lens. A prism was then used to direct the collimated light vertically upwards towards the plasma. A plano-convex cylindrical fused silica lens focused the collimated light into a sheet with a focal line that coincided with the line connecting the center of the torch injector with the center of the sampling cone. A mask, equipped with an adjustable iris, mounted above the cylindrical lens, was used to prevent the planar excitation light from scattering off of the torch or sampling cone. A beam dump was mounted above the ICP to prevent scattering off the RF box. The excitation sheet was 10 mm wide and extended from the end of the torch to less than 0.1 mm in front of the sampling cone.

A gated iCCD (7361-0001, Princeton Instruments, Trenton, NJ), triggered by a photodiode (DET210, Thorlabs, Newton, NJ) in the dye laser box, was mounted perpendicular to the plane of the excitation sheet. Twin 100 mm focal length achromatic doublets (AC254-100-A, Thorlabs) were used to focus the fluorescence onto the iCCD with unit magnification. An interference filter was placed between the achromatic doublets to isolate the desired fluorescence light. The CCD gain and number of exposures were adjusted to produce acceptable signal levels within a reasonable exposure time. The optimal exposure settings were different for images taken during SN and LA and varied between elements. However, exposure settings were held constant while imaging a given element during SN or LA at different carrier gas flow rates (including the He addition) or laser fluences. Finally, for each image, a background image was taken,

immediately before or after the fluorescence image to subtract the emission signal. Fig. 2.1 shows the general setup of the instrumentation.

2.2.5   Image processing

Using Winview software, (Princeton Instruments, Trenton, NJ), background images were subtracted from the corresponding fluorescence images. Background-subtracted images were converted to ASCII format and processed with Matlab. The signal intensities for the various carrier gas flow rates were normalized to the flow rate with the greatest signal. The intensity scales for the SN and LA, and those for the different elements are different, and thus not directly comparable. Note that in the axial cross sections, the intensities are reliable only between 2 mm and 12 mm downstream from the load coil, the region that was fully illuminated by the 10-mm-wide laser sheet. Matlab was also used to plot the various cross sections and calculate FWHM values. Unless stated otherwise, radial cross sections were plotted at axial positions where the signal intensity was greatest. Defining the radial profile this way allows direct comparison of the radial distributions at different nebulizer gas flow rates.

Table 2.1					
Fluorescence scheme					
Analyte	Excitation	Fluorescence	Filter	Dye	Gate width : delay
Ba II	455.404 nm	614.172 nm	614.2 nm (1 nm bp)	Coumarin 460	60 ns : 35 ns
Ca II	393.366 nm	854.21 nm	854.3 nm (1.1 nm bp)	PBBO	60 ns : 28 ns
Sc II	358.09 nm	432.50 nm	432.50 nm (1 mm bp)	DMQ	65 ns : 35 ns

2.3 Results and discussion

2.3.1 Scandium

2.3.1.1 Solution nebulization vs. laser ablation
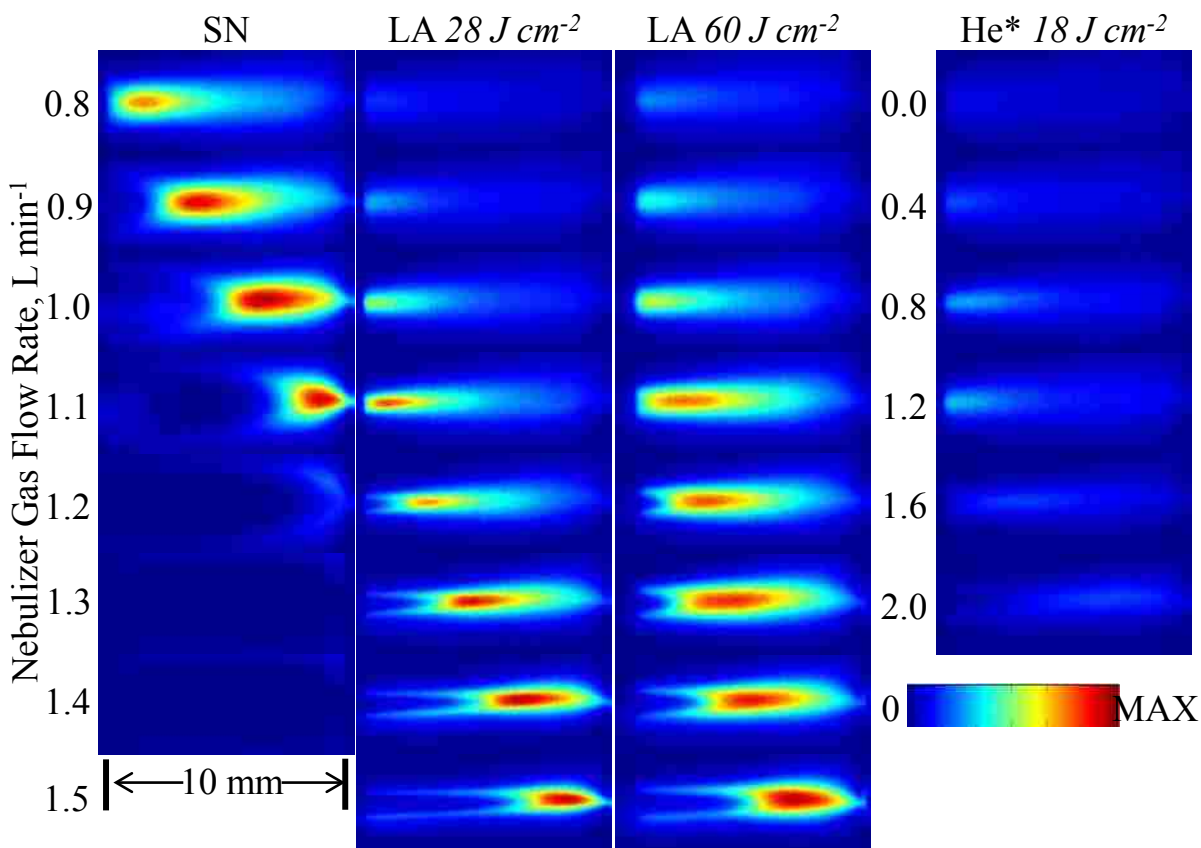
Figure 2.2 Images of Sc ions obtained using planar LIF. Flow rates on the far left indicate the flow for column 1-3. The flow rates to the left of the He images, column 4, represent additions of He to a constant flow rate of 0.7 L mn^{-1} Ar. Each image is oriented similarly with the load coil out of the image to the left and the sampling cone just protruding into the right side.

High resolution images of Sc ion densities in an ICP, obtained during SN and LA (at 28 J cm^{-2} and 60 J cm^{-2}) at varying flow rates, are presented in Fig. 2.2. These images provide direct observation of ion densities that form in the ICP subsequent to LA. Differences between the images obtained during LA and SN can be understood in terms of fundamental differences in the

aerosol properties and their complex interactions with ICP environment. As discussed

previously, when compared to SN, aerosol generated during LA lacks solvent, leading to

significantly less mass loading in the ICP (several 100 µg s^{-1} during SN and only several 10 ng

s^{-1} during LA) [26], and representing a much broader range of sizes, shapes, and morphologies.

Ablation patterns of metals have been described in a number of papers [27, 28]. Aerosols

produced during LA of Al-based alloys have been described as consisting of irregularly shaped

individual particles, clusters, and hard-agglomerates (clusters melted together) [16]. An ablation

rate of 1.04 µm per pulse at 23 J cm^{-2} and significant crater chimney formation has also been

reported [29]. As expected, significant differences can be seen qualitatively in the spatial profiles

of Sc ions obtained during SN and LA. The differences will be discussed in terms of the axial

and radial distribution of ion densities.

2.3.1.2   Axial profiles

To support the images in Fig. 2.2, axial cross sections, extracted from the center axes of the

images, are provided in Fig. 2.3. As seen in both figures, aerosol produced during LA led to peak

Sc ion fluorescence signals much farther upstream for a given nebulizer gas flow rate when

compared to SN. This observation is not unexpected. The desolvation process, required for

solvent-rich aerosol droplets produced during SN, delays atomization and ionization when

compared to "dry" aerosol produced during LA [30]. Indeed, during LA, an addition of roughly

0.4 L min^{-1} is required to shift ionization to the downstream positions of SN. It is possible that

local cooling effects associated with the desolvation of large aerosol droplets entrained to the

ICP during SN are a contributing factor. However, since gas temperatures in the central channel

of the ICP, which largely dictate the axial position that vaporization begins, are essentially

independent of sample properties, any contribution from such cooling effects would be minor

[31]. In addition to being shifted upstream relative to the SN profiles, the LA profiles rise more gradually. The change in the profile shape could be a reflection of reduced oxide formation during LA [32-34], or it could be due to a shift in the particle size distribution to favor smaller particles.
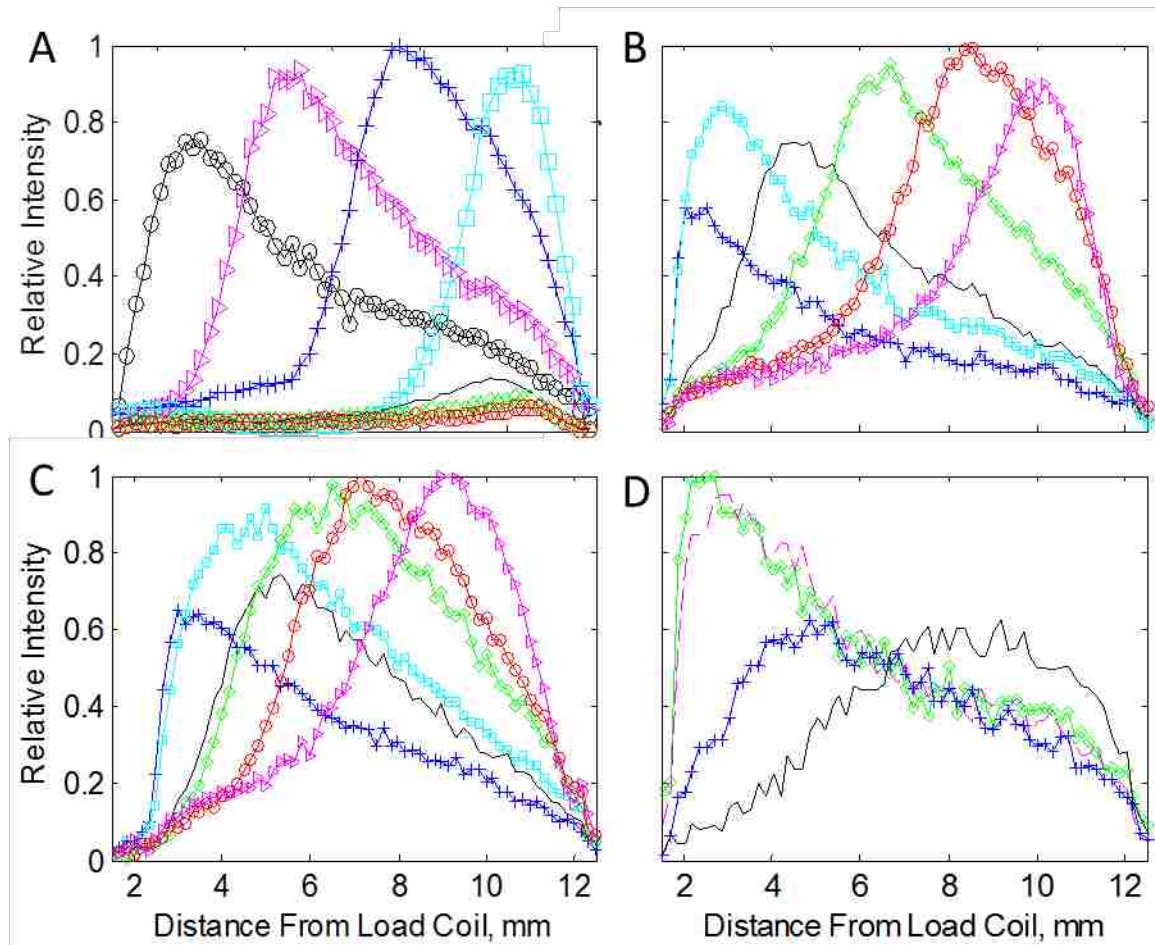
Figure 2.3 Cross-sectional plots of the axial distribution of Sc ions along the center axis taken during (a) SN, (b) LA at 28 J cm^{-2}, (c) LA at 60 J cm^{-2}, and (d) LA at 28 J cm^{-2} with added He. Flow rates for (a), (b), and (c) are labeled as follows: (—o—) 0.8 L min^{-1}, (— —) 0.9 L min^{-1}, (—+—) 1.0 L min^{-1}, (—□—) 1.1 L min^{-1}, (——) 1.2 L min^{-1}, (—◇—) 1.3 L min^{-1}, (—o—) 1.4 L min^{-1}, and (—►—) 1.5 L min^{-1}. Increments of 0.4 L min^{-1} He were added to a constant flow of 0.7 L min^{-1} Ar. He additions plotted in (d) are labeled as follows: (—◇—) 0.8 L min^{-1}, (— —) 1.2 L min^{-1}, (—+—) 1.6 L min^{-1}, and (——) 2.0 L min^{-1}.

2.3.1.3 Radial ion distributions

A significant difference between the radial distributions of ions produced during SN and LA was observed. Most apparent at low fluence, the radial profiles of ions were narrower with LA sample introduction than they were with SN. FWHM values were calculated from radial cross sections at axial positions of peak fluorescence intensities for each flow rate and are plotted in Fig. 2.4 for both SN and LA. It should be noted that due to differences in the axial profiles, the FWHM calculated for LA represents a position much farther upstream than SN. Another way to look at the data is to compare FWHM values at flow rates that give comparable axial profiles. The closest matches are at flows of 0.8 and 1.1, 0.9 and 1.3, and 1.1 and 1.5 L min^{-1}, for SN and LA, respectively. Either way of looking at the data makes it clear that SN leads to greater radial spreads in ion densities than LA. The broad profiles for LA at low flow rates are due to the fact that the peak ion densities are upstream from the imaged region and the observed images are broadened by diffusion. The sharp decrease in FWHM observed during SN at 1.1 L min^{-1}, presumably caused by "pinching" of off-axis gas being drawn into the sampling cone, was not observed during LA at high fluence and only moderately at low fluence. A number of mechanisms could be contributing to the difference in radial profiles observed here.

Our observations appear at first glance to be consistent with results recently reported by Flamigni, et al. [14]. They observed narrower radial neutral atom emission profiles for dry LA aerosols than for LA aerosols to which water had been added. They proposed that more-efficient coupling of the RF field due to the presence of gaseous water led to a steeper temperature gradient that promoted greater diffusion. However, as will be noted in section 2.3.1.4, the addition of water to a LA aerosol did not significantly broaden the radial fluorescence profiles, suggesting that differences between SN and LA other than the presence of water are affecting the

radial distributions. Differences in the flow profiles of aerosol particles produced by SN and LA in the transport tube leading to the ICP might be a contributing mechanism. Gas velocities in the laminar flow through the transport tube are greatest in the center and zero at the wall. The densities of aerosol particles across the cross section of the transfer tube have been shown to be inhomogeneous under certain conditions [21, 35-37]. Variations in radial distributions of particles in the transport tube between LA and SN could lead to differences in the radial profiles observed in the ICP. Coulomb fission of aerosol droplets, occurring during transport or desolvation, may give rise to greater radial dispersion of SN aerosol [38]. Finally, differences in flow patterns within the ICP are another possibility [39, 40]. Contributions from mechanisms discussed above are speculative at this point. More work is needed to characterize actual contributions from these source and the implications on ion transmission through the MS interface.
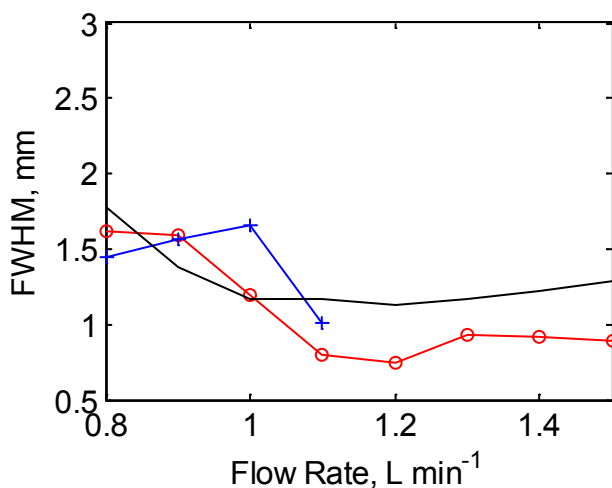

Figure 2.4 FWHM values calculated from radial cross sections at each flow rate for Sc ions recorded during (—+—) SN, (—o—) LA at 28 J cm^{-2}, and (——) LA at 60 J cm^{-2}.

2.3.1.4 Solvent

To investigate the influence of water vapor on the ion profile, sample transport tubing was configured using a Y connector to introduce water vapor produced from the pneumatic nebulizer system into the aerosol transport tube of the ablation system just upstream from the sheath gas connector. A total flow of 1.0 L min^{-1} Ar, split equally between the ablation cell and nebulizer, was kept constant throughout the experiments. Fig. 2.5 presents images obtained at various conditions. Image (I) in Fig. 2.5, was obtained while aspirating a 50 ppm solution with the LA shutter closed (no LA aerosol present). Fig. 2.5 (II) and (IV), were obtained while introducing "dry" aerosol (no nitric acid was aspirated) generated by LA at 28 and 60 J cm^{-2}, respectively. Fig. 2.5 (III) and (V) were obtained while introducing "wet" aerosol (nitric acid was aspirated) generated by LA at 28 and 60 J cm^{-2}, respectively. Fig. 2.6 shows axial and radial cross sections of the images in Fig. 2.5. Note that in both figures, the scales on the individual images and traces were normalized to maximum values to facilitate comparisons of shapes. The SN peak intensity was five times that for LA. There were no significant intensity differences between the wet and dry aerosols. Data in Figs. 2.5 and 2.6 lead to some interesting conclusions. Clearly, the individual flows through the pneumatic nebulizer or the flow through the laser ablation chamber combine with the total flow through the torch injector tube to influence the distribution of ions in an ICP. For example, none of the traces in Fig. 2.6 matches either of the traces in Fig. 2.3 obtained at a central channel flow of 1 L min^{-1}. With only half of the total flow passing through each of the aerosol production sources, the ion distributions are much more similar than is the case when the total flow is directed through either source individually. It is possible that the additional tubing and the Y connector required for this experiment act as a particle size filter that makes the two aerosol sources more similar than they are if they are connected individually in

their normal configurations. Perhaps the most significant result is the small effect that added

water has on the LA aerosol. The addition of water causes only a slight downstream shift in the

axial profiles, and the effect on the radial profiles and peak intensities is negligible. Given the

changes reported in ref. 14, it is unclear why similar effects were not observed here.
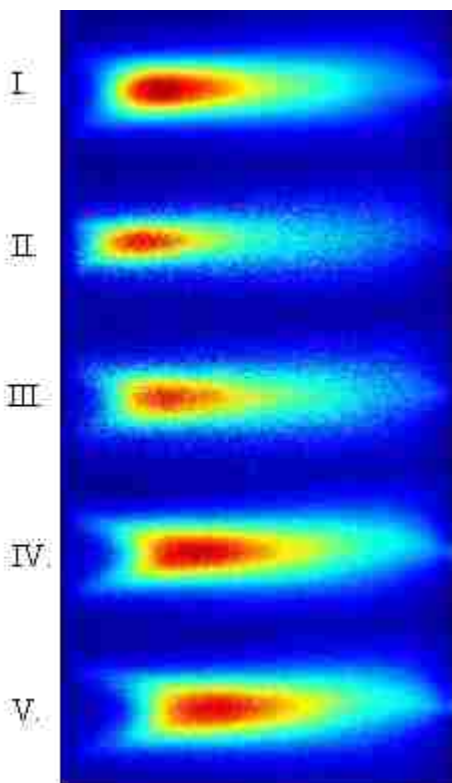
Figure 2.5 LIF images showing the influence of solvent on Sc ion densities in the ICP. In each image, 1.0 L mn^{-1} of Ar was split equally between the LA and SN systems. Image (I) was obtained while aspirating 50 ppm Sc without LA aerosol. Images (II) and (III) were obtained during LA at 28 J cm^{-2} without and with aspirating 2% nitric acid, respectively. Images (IV) and (V) were identical to (II) and (III) but performed at 60 J cm^{-2}. Due to the significant difference in the signal intensities of each image, the color scales for each image are different.
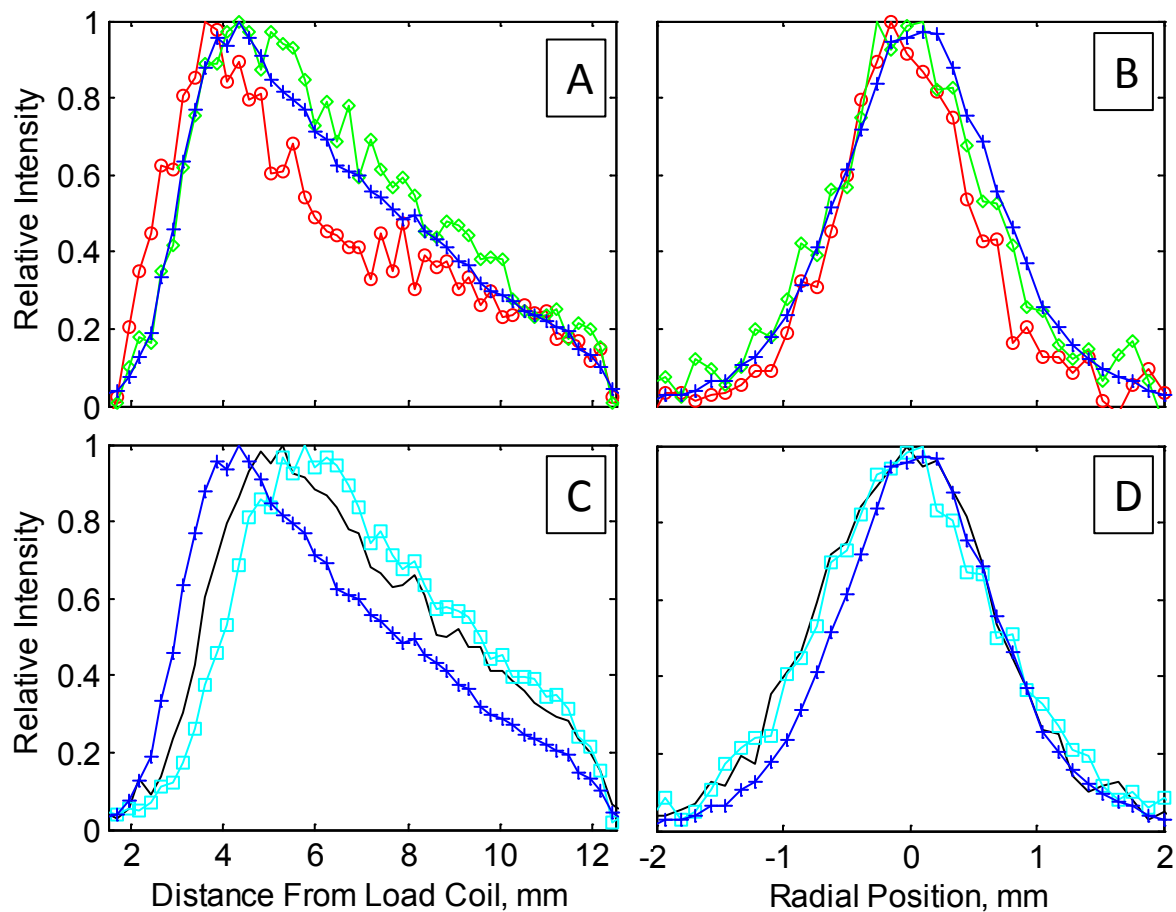
Figure 2.6 Axial (a) and radial (b) cross sections of images I, II, and II in Fig. 2.5, labeled as follows: (—+—) 50 ppm Sc, (—o—) dry and: (—◇—) wet aerosol produced during LA at 28 J cm^{-2}. Axial (c) and radial (d) cross sections of images I, IV, and V in Fig. 5, labeled as follows: (—+—) 50 ppm Sc, (——) dry and (—□—) wet aerosol produced during LA at 60 J cm^{-2}.

2.3.1.5   Laser fluence

Images in Fig. 2.7a were obtained at various fluences for two different Ar gas flow rates, 1.2 (left) and 1.3 L min^{-1} (right). Raw and normalized axial cross sections of the images obtained at 1.3 L min^{-1} are presented in Fig. 2.7b and 2.7c, respectively. FWHM values are plotted as a function of fluence and are presented in Fig. 2.7d. As seen in these images, increasing fluence led to a significant increase in the number of ions formed in the ICP, a downstream shift in the axial position of peak ion fluorescence, and an increase in the width of the radial distribution of

36

ions. These results are consistent with the initial differences observed between images obtained during LA at 28 and 60 J cm^{-2}. It has been reported that increasing laser fluence leads to greater ablation rates [27], an overall greater number of aerosol particles, and, in some cases, an increase in the fraction of large particles [16]. The significant increase in the fluorescence signal observed at greater fluence certainly reflects more particles produced at greater ablation rates. Moreover, a shift in the ablation mechanism from surface vaporization to phase explosion at fluences greater than 7 J cm^{-2} leads to a sharp increase in ablation rates [27]. Such a shift could account for the sharp increase in the signal intensity observed between 12 to 28 J cm^{-2}, presented quantitatively in the axial profiles presented in 2.7b.

Inspection of the normalized axial profiles presented in Fig. 2.7c reveals that increasing fluence shifts the axial position of peak fluorescence downstream and leads to a more gradual decline in the downstream end of fluorescence peak. An increase in the fraction of large particles would account for both observations. However, greater mass loads associated with an increase in the overall number of particles, regardless of changes in the size distribution, could lead to cooling effects that also might account for the observations. It is unclear at this point which mechanism is more pertinent.

As seen qualitatively in Fig. 2.7a and quantitatively in Fig. 2.7d, increasing fluence led to a significant increase in the widths of radial distributions of ions formed in the ICP. It is unlikely that changes in ICP environment, such as local cooling associated with an increased fraction of large particles, or greater mass loads contribute to this effect. Rather, it suggests that changes in the aerosol properties or flow patterns are leading to the changes in the radial profiles observed. It is possible that micron-sized agglomerates, preferentially formed at greater fluence, undergo vaporization mechanisms that lead to wider radial distributions.
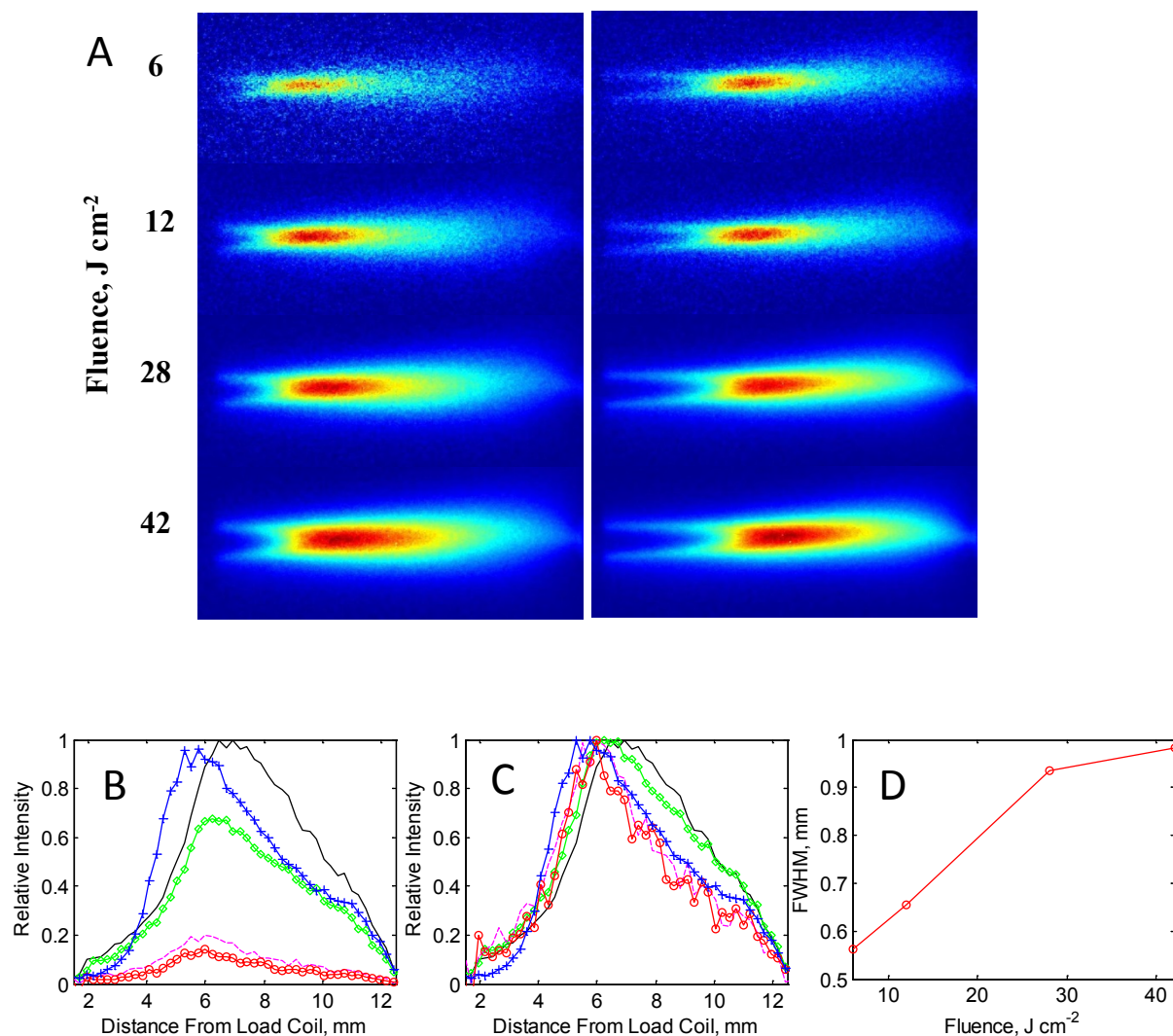
Figure 2.7 (a) Images of Sc ion densities obtained at various fluences during ablation with Ar flow rates of 1.2 L mn^{-1} (left) and 1.3 L mn^{-1} (right). (b) and (c) axial cross sections of the images obtained at 1.3 L min^{-1} presented in Fig. 7a. The profiles in (c) have been scaled to their maximum value to facilitate comparisons of the shapes and positions of the curves. The legends are as follows: (—o—) 60 J cm^{-2}, (— —) 130 J cm^{-2}, (—◇—) 360 J cm^{-2}, (——) 540 J cm^{-2}. (—+—) SN at 0.9 L min^{-1}, included for comparison. (d) FWHM calculated from the radial cross sections at each fluence during ablation with an Ar flow rate of 1.3 L min^{-1}.

2.3.1.6 Helium addition

The addition of He to the carrier gas significantly affects the ablation event, transport to the ICP, and conditions in the plasma [27, 41-43]. Helium could also change ion transport efficiency through the vacuum interface of the ICP-MS, although to our knowledge the effects of plasma gas composition on ion transport efficiency in the vacuum interface have not been studied. The presence of He during ablation leads to a greater fraction of smaller aerosol particles than is produced in pure Ar [44]. Also, because He is lighter than Ar, larger particles that do form are less likely to be transported to the ICP. The overall effect is fewer large particles that can lead to signal spikes [45, 46]. However, because the severity of these effects depends on a variety of factors, including laser pulse duration, wavelength, ablation cell design, and sample type [44], fundamental studies of He/Ar mixtures can lead to conflicting results. The addition of He also significantly affects ICP environment, increasing gas-kinetic temperatures of the central channel and diffusion rates. The changes with the addition of He are attributed to its high thermal conductivity and low mass [1, 47-48]. The addition of He to the carrier gas should lead to aerosol vaporization lower in the plasma as well as increased diffusion, and such changes have been observed experimentally [26].

Consistent with the observations noted above, the addition of He to the carrier gas in our experiments led to aerosol vaporization much lower in the plasma than equivalent total flow rates of pure Ar. As seen in Fig. 2.2 and 2.3d, Sc ion densities do not reach their maximum near the sampling cone until 2.0 L min^{-1} He has been added, making a total flow rate of 2.7 L min^{-1}. This observation suggests increasing gas temperatures caused by the addition of He more than compensate for cooling associated with increasing gas flow rates. A significant reduction in the number of large particles produced or transported with He addition would also contribute to the

upstream shift in vaporization observed. Reduced local cooling, associated with large particles vaporizing in the ICP, would enhance the upstream shift in small and medium sized particle vaporization [31].

Not all changes observed in the ion densities associated with the use of He were expected. Increased sensitivities are typically associated with the addition of He to the ablation cell. Improvements in sensitivity have been attributed to greater transport efficiencies of aerosol particles from the ablation cell to the ICP [49]. Our signal intensities obtained with added He were significantly lower than signals obtained during LA at 28 J cm^{-2} using Ar only. Consistent with our observations, other groups have reported sensitivity decreases associated with He addition [50]. The decrease in sensitivity was attributed to a reduction in the number of medium sized particles in the aerosol. A key point in reconciling our observations that He reduces fluorescence intensity with reports that He addition improves ICP-MS sensitivity is recognition that different quantities are being measured. We are measuring ion densities in the plasma and other investigators are measuring ion counts in mass spectrometers. It is entirely possible that ion transport through the vacuum interface improves with the addition of helium, and that lower ion densities in the plasma could still lead to higher mass spectrometric signals. For example, gas velocities in the first stage of the vacuum interface are inversely proportional to the square root of mass [51], and analyte ions move at the speed of the bulk gas flow [52]. Because of the higher gas speeds and reduced residence time in the first vacuum stage, analyte losses to ion-electron recombination should be lower in He than in Ar [53]. There are analyte losses due to scattering in shocks at the tip of the skimmer cone [54], and one would expect those losses to be lower in He than in Ar. Finally, it is possible that non-ideal beam behavior caused by space charge effects would be less severe in a He ion beam than in an Ar ion beam.

We have considered and rejected the possibility that reduction in fluorescence intensity with the addition of He was due to a reduction in fluorescence quantum efficiency rather than a reduction in analyte ion density. Quenching of excited atoms by noble gases is inefficient. Detailed quenching cross sections are not available, but using published upper limits for analogous transitions in potassium atoms [55], we estimate that the collisional quenching rates in He at 5500 K are approximately 2×10^5 s^{-1}, orders of magnitude less than the radiative rates for the transitions used in the fluorescence measurements.

2.3.2   Calcium

2.3.2.1   Solution nebulization vs. laser ablation

Silicate reference materials are commonly used as calibration standards and have consequently been used as samples in numerous fundamental studies. Because these materials exhibit ablation patterns markedly different than metals, comparing results from glasses with those reported above for the aluminum alloy would be desirable [29]. Glasses with concentrations of elements that could be effectively imaged by LIF were not available, so we chose crystalline optical windows as a substitute. CaF_2, which we used to generate Ca images, has shown ablation patterns similar to silicate materials [23].
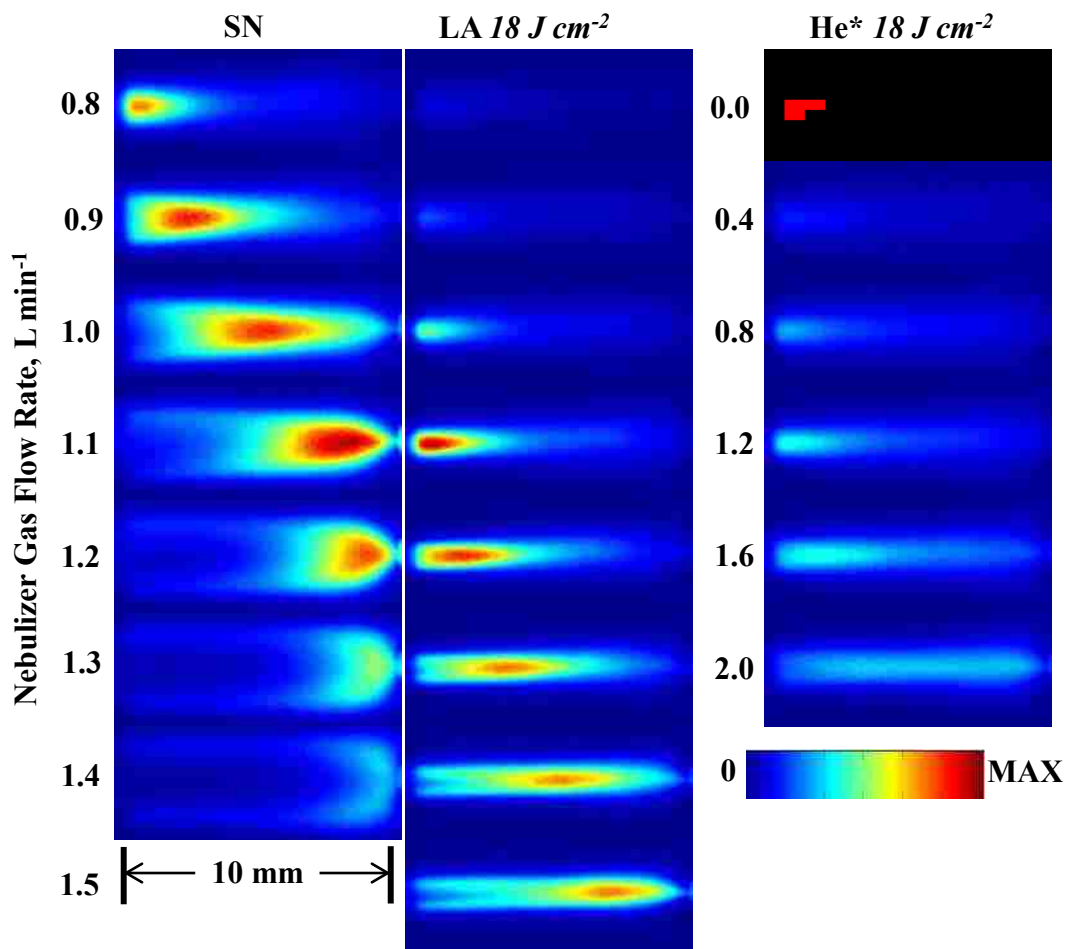
Figure 2.8 LIF images of Ca ions obtained using planar LIF. The orientation of each image and patterns of gas flow are identical to those described previously for Sc in Fig. 2.2.
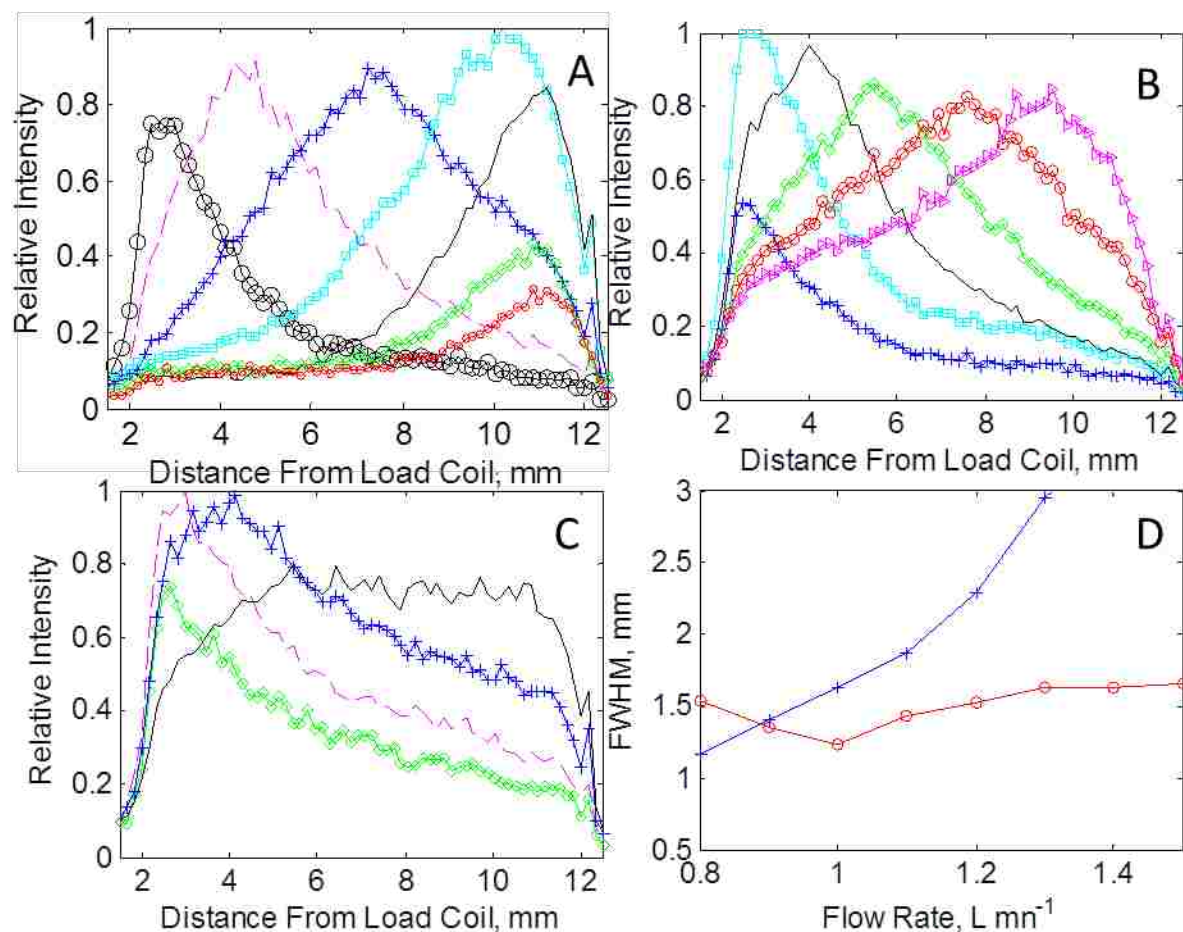
Figure 2.9 Cross-sectional plots of the axial distribution of Ca ions along the center axis taken during (a) SN, (b) LA at 18 J cm^{-2} (c) LA at 18 J cm^{-2} with added He. Flow rates for (a) and (b) are labeled as follows: (—o—) 0.8 L min^{-1}, (— —) 0.9 L min^{-1}, (—+—) 1.0 L min^{-1}, (—□—) 1.1 L min^{-1}, (——) 1.2 L min^{-1}, (—◇—) 1.3 L min^{-1}, (—o—) 1.4 L min^{-1}, and (—▶—) 1.5 L min^{-1}. Increments of 0.4 L min^{-1} He were added to a constant flow of 0.7 L min^{-1} Ar. He additions plotted in (c) are labeled as follows: (—◇—) 0.8 L min^{-1}, (— —) 1.2 L min^{-1}, (—+—) 1.6 L min^{-1}, and (——) 2.0 L min^{-1}. Also, FWHM calculated from radial cross sections at each flow rate for (—+—) SN and (—o—) LA with Ar at 18 J cm^{-2} are plotted in (d).

2.3.2.2 Axial profiles

Images of Ca ions, obtained during SN, LA at 18 J cm^{-2}, and LA 18 J cm^{-2} with added He are presented in Fig. 2.8. Axial cross sections similar to those described for Sc in section 2.3.1.2 above are plotted in Fig. 2.9. Differences between SN and LA followed the same general trend seen with Sc: aerosol produced during LA leading to significant ions densities formed lower in the ICP, spread over a greater axial distance, and restricted to a narrower radial distance. When

compared to Sc, the increase in the length of the axial profile during LA, relative to SN, was more pronounced in Ca, especially on the upstream section of the profile. This is consistent with greater ablation rates reported for CaF_2, 2.0 μm per pulse compared to 1.04 μm per pulse for Al [18, 29]. An increase in the number density of particles produced during the ablation event leads to more collisions between those particles and the formation of large "cotton like" soft agglomerations [23]. These large agglomerations could account for the increased length in the axial profile for Ca. SN also led to ion densities distributed over a larger axial distance for Ca when compared to SN of Sc, indicating that, in addition to the particle size distribution, the identity of the analyte affects the distribution of ions in the ICP. As was the case with Sc, LA of CaF_2 led to much narrower Ca ion radial distributions than SN, illustrated in Fig. 2.9d.

2.3.2.3 Fluence

Images of Ca ions, taken during LA at fluences of 60, 130, 360, and 540 J cm^{-2}, are presented in Fig. 2.10a at nebulizer gas flow rates of 1.1 L min^{-1} (left) and 1.3 L min^{-1} (right). This figure covers a range over much higher fluences than evaluated with Sc. Axial and radial cross sections, and their calculated FWHM, for the images obtained at 1.3 L min^{-1} are presented in Fig. 2.10b, 2.10c, and 2.10d, respectively. As with metals, increasing fluence led to increasing ablation rates, a greater number of particles, and the formation of larger agglomerates [29]. Changes in the Ca ion distributions associated with increasing fluence followed trends similar to those observed with Sc ions.
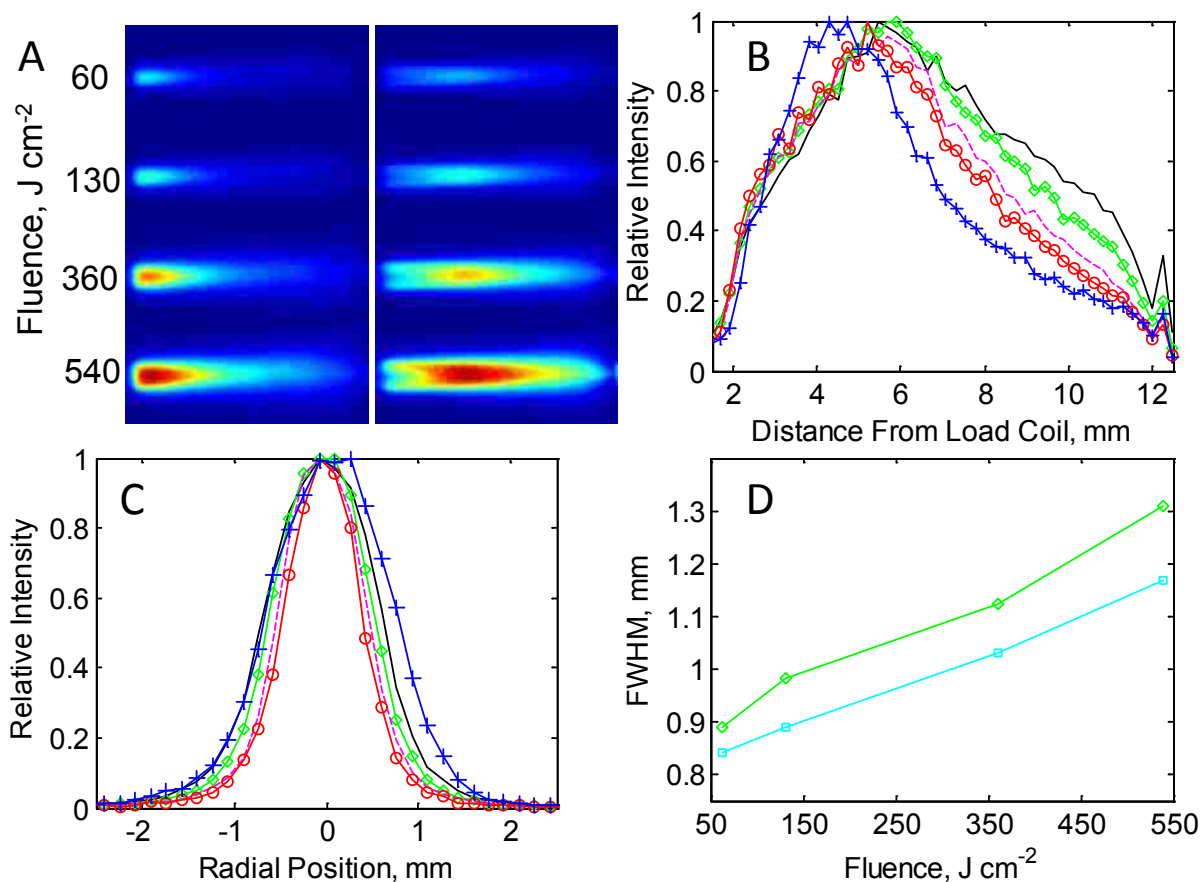
Figure 2.10 (a) Images of Ca ion densities obtained at various fluences during ablation with Ar gas flow rates of 1.1 L min^{-1} (left) and 1.3 L min^{-1} (right). (b) Axial and (c) radial cross sections of the images obtained at 1.3 L min^{-1} presented in Fig. 2.10a. The legends are as follows: (—o—) 60 J cm^{-2}, (— —)130 J cm^{-2}, (—◇—) 360 J cm^{-2}, (——) 540 J cm^{-2}. (—+—) SN at 0.9 L min^{-1}, included for comparison. (d) FWHM calculated from the radial cross sections at each fluence during ablation with Ar flow rates of (—□—) 1.1 L min^{-1} and (—◇—) 1.3 L min^{-1}.

2.3.2.4 Helium addition

Results obtained during LA with He addition during LA of the CaF$_2$ windows were very similar to those presented for Sc in Fig. 2.2. Although He addition led to significant signal supression for both Sc and Ca, the effect was slightly less pronounced with Ca. Also notable is the axial profile, plotted in Fig. 2.9c, produced when 2.0 L min^{-1} He was added to 0.7 L min^{-1} Ar. Unlike ion profiles produced during LA in pure Ar, which have a definite peak fluorescence

signal, the signal produced here plateaus over roughly 5 mm. It is unclear whether changes in the size distribution of aerosols entering the ICP or changes in ICP conditions are producing this effect. Such a plateauing effect could, in part, account for improvements in accuracy that have observed when adding He to the carrier gas. This effect was less pronounced when the ablation target was the Al-Sc alloy. However, transport losses in He depend on particle size distributions, and the distributions for the Sc-containing Al alloy should be significantly different than those for the crystalline CaF_2.

2.3.3   Barium

BaF_2 and CaF_2 have very similar optical and mechanical properties. Not surprisingly, images of Ba ions obtained during SN, LA at 18 J cm^{-2}, and LA 18 J cm^{-2} with He addition, presented in Fig. 2.11 are remarkably similar to those of Ca ions presented in section 2.3.2 above. The differences in ionization potentials and atomic masses between Ba and Ca do not significantly affect the results.
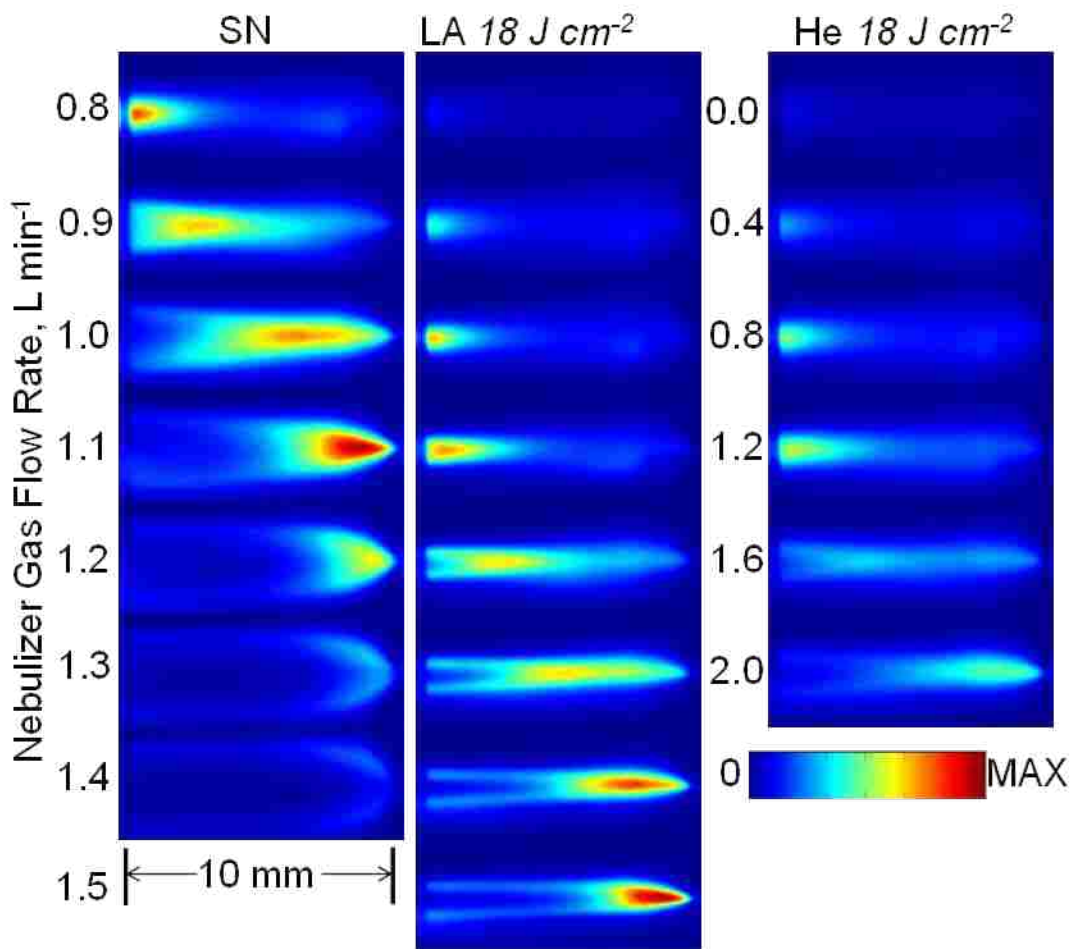
Figure 2.11 Images of Ba ions obtained using planar LIF. The orientation of each image and patterns of gas flow are identical to those described previously for Sc in Fig. 2.2.

2.3.3.1 Additional studies with helium

To further address the effects of He on analyte ion distributions, incremental amounts of He were added to 1.0 and 1.3 L min^{-1} Ar. Whereas previously described additions of He to 0.7 L min^{-1} often led to ion formation upstream from the imaging region, addition of He to 1.0 and 1.3 L min^{-1} Ar enabled direct comparison of ion profiles within the imaging region. The images obtained during the addition of various flows of He to 1.0 and 1.3 L min^{-1} Ar are presented in Fig. 2.12a. Axial cross sections of each image obtained at 1.0 and 1.3 L min^{-1} Ar are plotted in Fig. 2.12b and 2.12c, respectively. As expected, the addition of increasing amounts of He shifts

the ion profile downstream. These data reemphasize the point made earlier that, when it comes to setting the axial position of the ion density maximum, argon and helium flows are not equivalent, and that the total flow required to achieve optimum ICP-MS sensitivity depends strongly on the composition of the nebulizer gas.

The dependence of optimum flow rate on central gas composition complicates the comparison of ICP-MS sensitivities. Lacking a mass analyzer on our instrument, we selected combinations of Ar and He that produced maximum ion densities 2-3 mm upstream from the sampling cone. The results are presented in Fig. 2.13a. Clearly the pure Ar gives the highest peak ion density, and the peak value decreases as percentage of He increases. The axial distributions for the five flow combinations are similar, as shown in Fig 2.13b. Increasing amounts of He cause radial broadening, as shown in Fig. 2.13c.
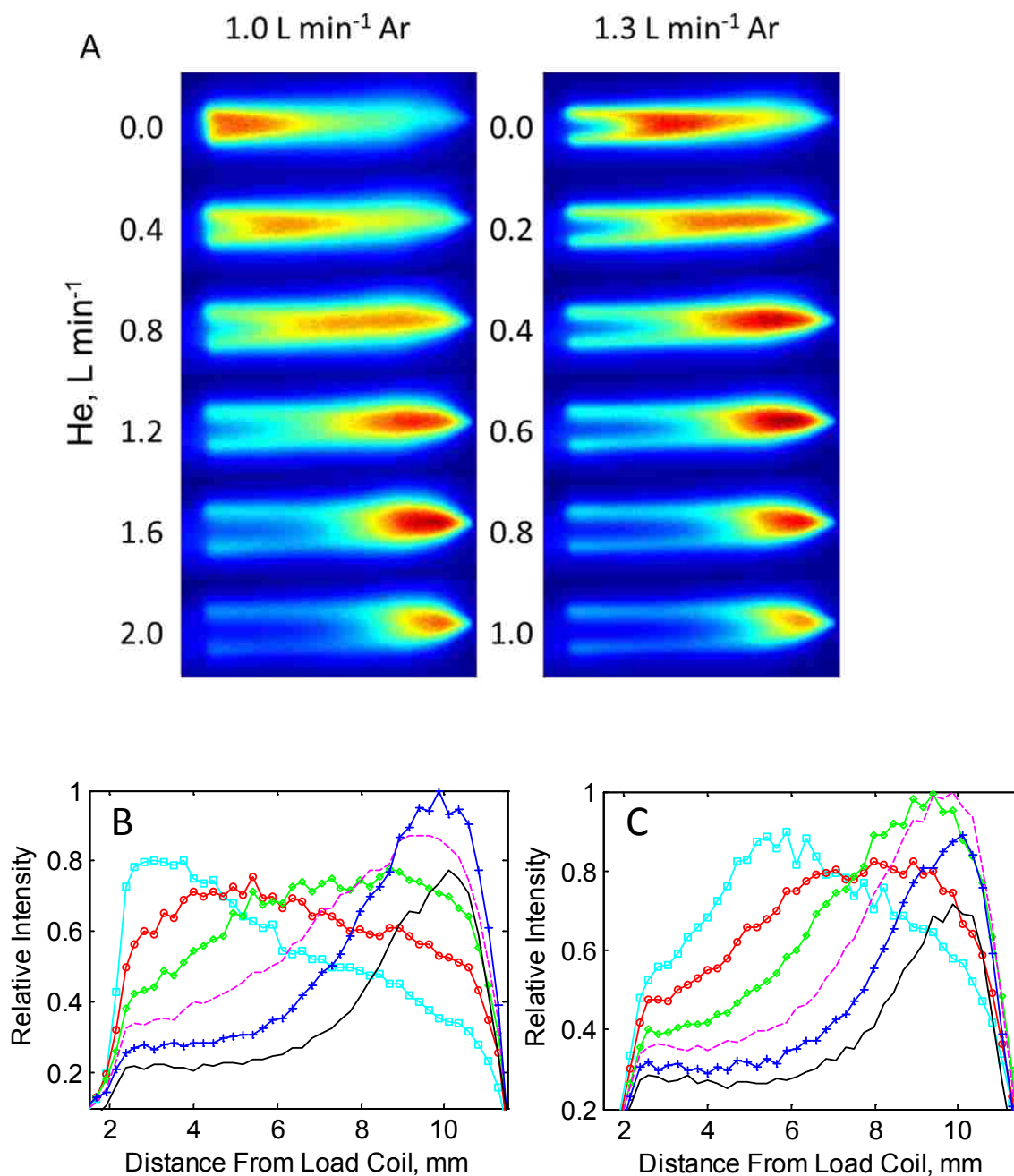
Figure 2.12 (a) Images of Ba ion densities obtained with incremental additions of He to 1.0 L min⁻¹ and 1.3 L min⁻¹ of Ar. (b) and (c) axial cross sections of the images obtained at 1.0 L min⁻¹ and 1.3 L min⁻¹ of Ar, respectively. The legends for the helium flows in the axial plots match the values in the images from top to bottom in the order: (—□—), (—○—), (—◇—), (— —), (—₊—), (——). The vertical scales in plots (b) and (c) are scaled to the maximum value in each set of curves.

49
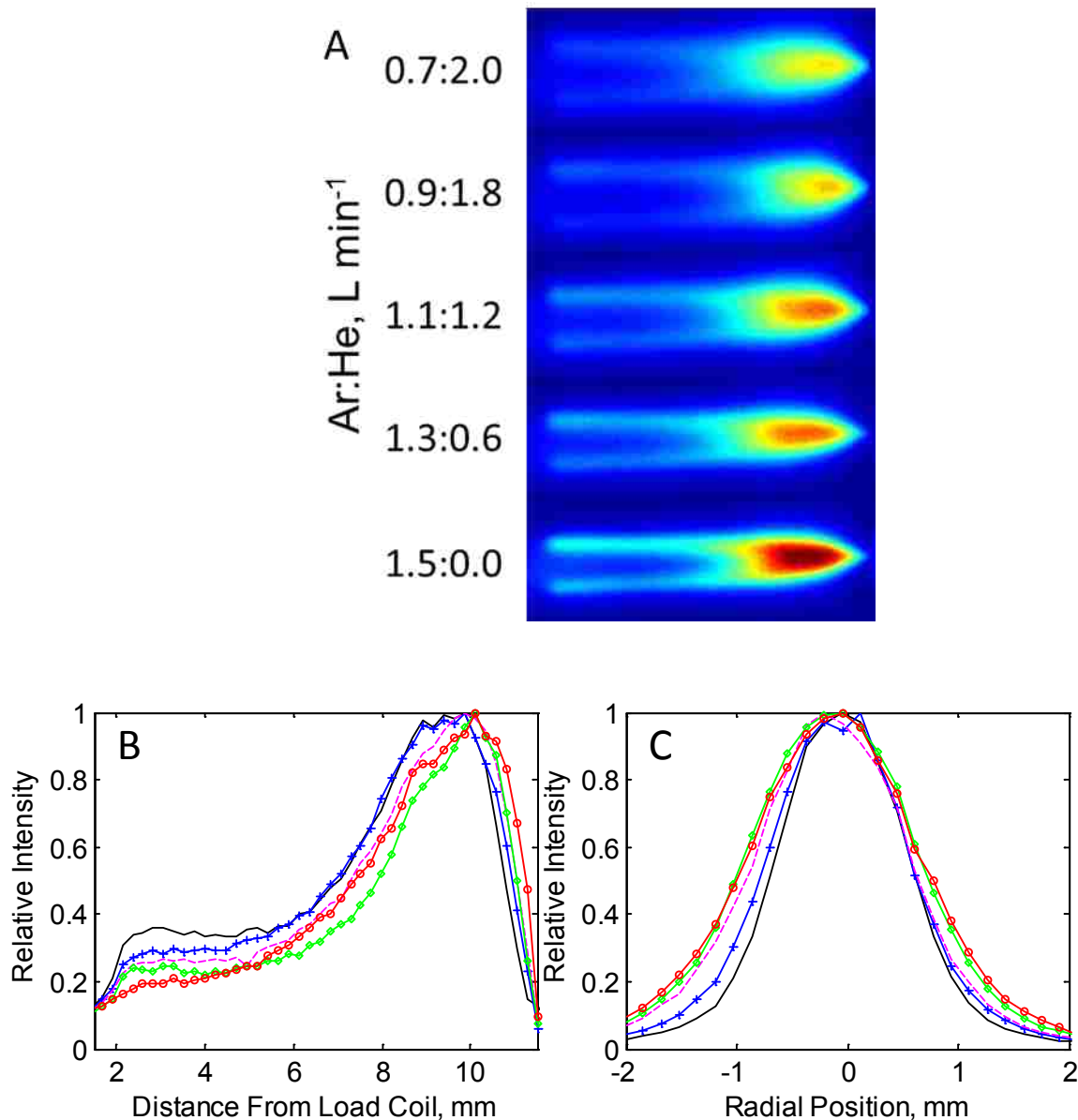
Figure 2.13 (a) Images of Ba ion densities obtained with various combinations of Ar and He flow rates. For each argon flow rate, the He flow rate was adjusted to give the maximum fluorescence intensity hear the sampling cone. (b) axial and (c) radial cross sections of the images in Fig. 14a, respectively. The intensity for each cross section is scaled to its maximum value to facilitate comparison of shapes. The Ar:He flow rates in the plots are: (—o—) 0.7:2.0 L min^{-1}, (—◇—) 0.9:1.8 L min^{-1}, (— —), 1.1:1.2 L min^{-1}, (—+—) 1.3:0.6 L min^{-1}, and (——) 1.5:0.0 L min^{-1}.

2.4   Conclusions

Significant differences in the spatial profiles of ion densities of aerosol produced during SN and LA were observed. When compared to SN, aerosol produced during LA led to ions formed

farther upstream in the plasma, with broader axial distributions and narrower radial distributions. These differences reflect fundamental differences between the aerosols and their complex interactions with the ICP. Delayed ion formation, observed with SN aerosol, was attributed to the rate-limited desolvation of droplets from the nebulizer. In preliminary experiments, solvent added independent of the analyte had very little effect of the ion profile beyond shifting it slightly downstream. Images were inspected for evidence of any size effects common to LA aerosol. Most notably, significant ion densities formed over large axial distances for LA aerosol were attributed to broad particle size distributions produced by LA. This picture is consistent with previously published work. Differences in the radial profiles generated by SN and LA aerosol warrant further investigation. We found that laser fluence positively correlated with the radial width of the ion distribution.

The addition of He to the nebulizer gas flow led to ion formation farther upstream in the plasma than occurred with pure Ar as the nebulizer gas at a given total flow rate. The upstream shift likely reflects a combination of He effects: fewer large particles transported to the ICP and increased gas-kinetic temperatures in the ICP. Varying the point in the flow stream at which He and Ar are mixed should help clarify contributions of He to the ablation process and ICP conditions.

Clearly, measurements of ion distributions in the ICP with LA sample introduction add important insights into signal production in LA-ICP-MS that cannot be obtained from mass spectrometric signals alone.

2.5   References

[1] Z. Wang, B. Hattendorf, D. Guenther, Analyte Response in Laser Ablation Inductively Coupled Plasma Mass Spectrometry, J. Am. Soc. Mass Spectrom., 17 (2006) 641-651.
[2] J.H. Macedone, D.J. Gammon, P.B. Farnsworth, Factors affecting analyte transport through the sampling orifice of an inductively coupled plasma mass spectrometer, Spectrochim. Acta,

Part B, 56B (2001) 1687-1695.

[3] J.H. MacEdone, A.A. Mills, P.B. Farnsworth, Optical measurements of ion trajectories through the vacuum interface of an inductively coupled plasma mass spectrometer, Appl Spectrosc, 58 (2004) 463-467.

[4] M. Gäckle, D. Merten, Study of plasma parameters influencing fractionation in laser ablation-inductively coupled plasma-mass spectrometry, Spectrochimica Acta Part B: Atomic Spectroscopy, 65 (2010) 991-1001.

[5] K. Niemax, Considerations about the detection efficiency in inductively coupled plasma mass spectrometry, Spectrochim. Acta, Part B, 76 (2012) 65-69.

[6] B.S. Duersch, P.B. Farnsworth, Characterization of the ion beam inside the skimmer cone of an inductively coupled plasma mass spectrometer by laser excited atomic and ionic fluorescence, Spectrochim. Acta, Part B, 54B (1999) 545-555.

[7] A.A. Mills, J.H. Macedone, P.B. Farnsworth, High resolution imaging of barium ions and atoms near the sampling cone of an inductively coupled plasma mass spectrometer, Spectrochimica Acta Part B: Atomic Spectroscopy, 61 (2006) 1039-1049.

[8] W.N. Radicic, J.B. Olsen, R.V. Nielson, J.H. Macedone, P.B. Farnsworth, Characterization of the supersonic expansion in the vacuum interface of an inductively coupled plasma mass spectrometer by high-resolution diode laser spectroscopy, Spectrochimica Acta Part B: Atomic Spectroscopy, 61 (2006) 686-695.

[9] H. Ma, N. Taylor, P.B. Farnsworth, The effect of the sampling interface on spatial distributions of barium ions and atoms in an inductively coupled plasma ion source, Spectrochimica Acta Part B: Atomic Spectroscopy, 64 (2009) 384-391.

[10] A.J. Edmund, S.D. Bergeson, M. Lyon, N. Taylor, I. Kalinitchenko, P.B. Farnsworth, Evaluation of space charge effects in the second vacuum stage of a commercial inductively coupled plasma mass spectrometer by planar laser-induced fluorescence imaging, Spectrochimica Acta Part B: Atomic Spectroscopy, 76 (2012) 109-118.

[11] D. Gunther, C. A. Heinrich, Enhanced sensitivity in laser ablation-ICP mass spectrometry using helium-argon mixtures as aerosol carrier, Journal of Analytical Atomic Spectrometry, 14 (1999).

[12] C. O' Connor, B.L. Sharp, P. Evans, On-line additions of aqueous standards for calibration of laser ablation inductively coupled plasma mass spectrometry: theory and comparison of wet and dry plasma conditions, Journal of Analytical Atomic Spectrometry, 21 (2006).

[13] M. Walle, J. Koch, D. Gunther, Analysis of brass and silicate glass by femtosecond laser ablation inductively coupled plasma mass spectrometry using liquid standard calibration, Journal of Analytical Atomic Spectrometry, 23 (2008) 1285-1289.

[14] L. Flamigni, J. Koch, D. Gunther, The effect of carrier gas humidity on the vaporization of laser-produced aerosols in inductively coupled plasmas, Journal of Analytical Atomic Spectrometry, 29 (2014) 280-286.

[15] R. Hergenroder, Laser-generated aerosols in laser ablation for inductively coupled plasma spectrometry, Spectrochimica Acta Part B-Atomic Spectroscopy, 61 (2006) 284-300.

[16] J.J. Gonzalez, C. Liu, S.-B. Wen, X. Mao, R.E. Russo, Metal particles produced by laser ablation for ICP-MS measurements, Talanta, 73 (2007) 567-576.

[17] N.J. Saetveit, S.J. Bajic, D.P. Baldwin, R.S. Houk, Influence of particle size on fractionation with nanosecond and femtosecond laser ablation in brass by online differential mobility analysis and inductively coupled plasma mass spectrometry, Journal of Analytical Atomic Spectrometry, 23 (2008).

[18] J.J. Gonzalez, C. Liu, S.B. Wen, X. Mao, R.E. Russo, Glass particles produced by laser ablation for ICP-MS measurements, Talanta, 73 (2007) 577-582.
[19] H.-R. Kuhn, D. Gunther, Laser ablation-ICP-MS: particle size dependent elemental composition studies on filter-collected and online measured aerosols from glass, Journal of Analytical Atomic Spectrometry, 19 (2004).
[20] M. Holá, V. Konečná, P. Mikuška, J. Kaiser, V. Kanický, Influence of physical properties and chemical composition of sample on formation of aerosol particles generated by nanosecond laser ablation at 213 nm, Spectrochimica Acta Part B: Atomic Spectroscopy, 65 (2010) 51-60.
[21] C.C. Garcia, H. Lindner, K. Niemax, Laser ablation inductively coupled plasma mass spectrometry-current shortcomings, practical suggestions for improving performance, and experiments to guide future development, J. Anal. At. Spectrom., 24 (2009) 14-26.
[22] S.H. Jeong, O.V. Borisov, J.H. Yoo, X.L. Mao, R.E. Russo, Effects of Particle Size Distribution on Inductively Coupled Plasma Mass Spectrometry Signal Intensity during Laser Ablation of Glass Samples, Anal. Chem., 71 (1999) 5123-5130.
[23] H.-R. Kuhn, D. Gunther, The agglomeration state of nanosecond laser-generated aerosol particles entering the ICP, Anal Bioanal Chem, 383 (2005) 434-441.
[24] M. Wälle, J. Koch, L. Flamigni, S. Heiroth, T. Lippert, W. Hartung, D. Günther, Detection efficiencies in nano- and femtosecond laser ablation inductively coupled plasma mass spectrometry, Spectrochimica Acta Part B: Atomic Spectroscopy, 64 (2009) 109-112.
[25] B. Hattendorf, C. Latkoczy, D. Gunther, Laser ablation-ICPMS, Anal Chem, 75 (2003) 341A-347A.
[26] Z. Wang, B. Hattendorf, D. Guenther, Vaporization and ionization of laser ablation generated aerosols in an inductively coupled plasma mass spectrometer-implications from ion distribution maps, J. Anal. At. Spectrom., 21 (2006) 1143-1151.
[27] D. Bleiner, Z. Chen, D. Autrique, A. Bogaerts, Role of laser-induced melting and vaporization of metals during ICP-MS and LIBS analysis, investigated with computer simulations and experiments, Journal of Analytical Atomic Spectrometry, 21 (2006) 910-921.
[28] A.H.A. Lutey, An improved model for nanosecond pulsed laser ablation of metals, Journal of Applied Physics, 114 (2013) -.
[29] I. Horn, M. Guillong, D. Gunther, Wavelength dependant ablation rates for metals and silicate glasses using homogenized laser beam profiles - implications for LA-ICP-MS, Applied Surface Science, 182 (2001) 91-102.
[30] J.W. Olesik, Investigating the fate of individual sample droplets in inductively coupled plasmas, Appl. Spectrosc., 51 (1997) 158A-175A.
[31] S. Groh, C.C. Garcia, A. Murtazin, V. Horvatic, K. Niemax, Local effects of atomizing analyte droplets on the plasma parameters of the inductively coupled plasma, Spectrochim. Acta, Part B, 64B (2009) 247-254.
[32] A.C. Lazar, P.B. Farnsworth, Matrix Effect Studies in the Inductively Coupled Plasma with Monodisperse Droplets. Part II: The Influence of Matrix on Spatially Integrated Ion Density, Applied Spectroscopy, 53 (1999) 465-470.
[33] T.M. Witte, R.S. Houk, Origins of polyatomic ions in laser ablation-inductively coupled plasma-mass spectrometry: An examination of metal oxide ions and effects of nitrogen and helium in the aerosol gas flow, Spectrochim. Acta, Part B, 69 (2012) 9-19.
[34] L. Flamigni, J. Koch, D. Günther, Experimental and theoretical investigations about the vaporization of laser-produced aerosols and individual particles inside inductively-coupled plasmas — Implications for the extraction efficiency of ions prior to mass spectrometry,

Spectrochimica Acta Part B: Atomic Spectroscopy, 76 (2012) 70-76.

[35] J. Koch, M. Waelle, R. Dietiker, D. Guenther, Analysis of Laser-Produced Aerosols by Inductively Coupled Plasma Mass Spectrometry: Transport Phenomena and Elemental Fractionation, Anal. Chem. (Washington, DC, U. S.), 80 (2008) 915-921.

[36] D. Bleiner, D. Gunther, Theoretical description and experimental observation of aerosol transport processes in laser ablation inductively coupled plasma mass spectrometry, Journal of Analytical Atomic Spectrometry, 16 (2001) 449-456.

[37] D. Autrique, A. Bogaerts, H. Lindner, C.C. Garcia, K. Niemax, Design analysis of a laser ablation cell for inductively coupled plasma mass spectrometry by numerical simulation, Spectrochimica Acta Part B: Atomic Spectroscopy, 63 (2008) 257-270.

[38] M.M. Fraser, D. Beauchemin, Evidence supporting the occurrence of Coulomb fission during conventional sample introduction in inductively coupled plasma mass spectrometry, Journal of Analytical Atomic Spectrometry, 24 (2009).

[39] H. Lindner, A. Murtazin, S. Groh, K. Niemax, A. Bogaerts, Simulation and Experimental Studies on Plasma Temperature, Flow Velocity, and Injector Diameter Effects for an Inductively Coupled Plasma, Analytical Chemistry, 83 (2011) 9260-9266.

[40] H. Lindner, A. Bogaerts, Multi-element model for the simulation of inductively coupled plasmas: Effects of helium addition to the central gas stream, Spectrochimica Acta Part B: Atomic Spectroscopy, 66 (2011) 421-431.

[41] D. Autrique, Z. Chen, V. Alexiades, A. Bogaerts, B. Rethfeld, A multiphase model for pulsed ns-laser ablation of copper in an ambient gas, AIP Conf. Proc., 1464 (2012) 648-659.

[42] J.-F.Y. Gravel, D. Boudreau, Study by focused shadowgraphy of the effect of laser irradiance on laser-induced plasma formation and ablation rate in various gases, Spectrochim. Acta, Part B, 64B (2009) 56-66.

[43] J. Koch, M. Wälle, S. Schlamp, T. Rösgen, D. Günther, Expansion phenomena of aerosols generated by laser ablation under helium and argon atmosphere, Spectrochimica Acta Part B: Atomic Spectroscopy, 63 (2008) 37-41.

[44] I. Horn, D. Gunther, The influence of ablation carrier gasses Ar, He and Ne on the particle size distribution and transport efficiencies of laser ablation-induced aerosols: implications for LA-ICP-MS, Appl. Surf. Sci., 207 (2003) 144-157.

[45] I. Kroslakova, D. Guenther, Elemental fractionation in laser ablation-inductively coupled plasma-mass spectrometry: evidence for mass load induced matrix effects in the ICP during ablation of a silicate glass, J. Anal. At. Spectrom., 22 (2007) 51-62.

[46] J.W. Olesik, N. Casey, Investigation of vaporization of laser ablation generated aerosol and monodisperse particles in a dry Ar ICP using time-resolved mass spectrometry, Spec. Publ. - R. Soc. Chem., 301 (2005) 164-174.

[47] L. Flamigni, J. Koch, H. Wiltsche, R. Brogioli, S. Gschwind, D. Guenther, Visualization, velocimetry, and mass spectrometric analysis of engineered and laser-produced particles passing through inductively coupled plasma sources, J. Anal. At. Spectrom., 27 (2012) 619-625.

[48] N.N. Sesi, A. Mackenzie, K.E. Shanks, P. Yang, G.M. Hieftje, Fundamental studies of mixed-gas inductively coupled plasmas, Spectrochimica Acta Part B: Atomic Spectroscopy, 49 (1994) 1259-1282.

[49] D. Bleiner, A. Bogaerts, Computer simulations of sample chambers for laser ablation– inductively coupled plasma spectrometry, Spectrochimica Acta Part B: Atomic Spectroscopy, 62 (2007) 155-168.

[50] D.C. Perdian, S.J. Bajic, D.P. Baldwin, R.S. Houk, Time-resolved studies of particle effects

in laser ablation inductively coupled plasma-mass spectrometry: Part 2. Investigation of MO+ ions, effect of sample morphology, transport gas, and binding agents, J. Anal. At. Spectrom., 23 (2008) 336-341.

[51] D.R. Miller, Free Jet Sources, in: G. Scoles (Ed.) Atomic and Molecular Beam Methods, Oxford University Press, Oxford, UK, 1988.

[52] S.D. Tanner, Plasma Temperature from Ion Kinetic Energies and Implications for the Source of Diatomic Oxide Ions in Inductively-Coupled Plasma-Mass Spectrometry, J Anal Atom Spectrom, 8 (1993) 891-897.

[53] J.H. Macedone, P.B. Farnsworth, Changes in plasma composition during the expansion into the first vacuum stage of an inductively coupled plasma mass spectrometer, Spectrochimica Acta, Part B: Atomic Spectroscopy, 61B (2006) 1031-1038.

[54] N. Taylor, P.B. Farnsworth, Experimental characterization of the effect of skimmer cone design on shock formation and ion transmission efficiency in the vacuum interface of an inductively coupled plasma mass spectrometer, Spectrochim Acta B, 69 (2012) 2-8.

[55] C.T.J. Alkemade, Metal vapours in flames, 1st ed., Pergamon Press, Oxford Oxfordshire ; New York, 1982.

3 EVALUATION OF PARTICLE SIZE DISTRIBUTIONS PRODUCED DURING ULTRA-VIOLET NANOSECOND LASER ABLATION AND THEIR RELATIVE CONTRIBUTIONS TO ION DENSITIES IN THE ICP

This chapter has been submitted for publication in Spectrochimica Acta Part B.

3.1 Introduction

The ICP is a critical juncture in LA-ICP-MS instruments. Efficient, stoichiometric ion production in the ICP and transmission through the MS interface is essential to achieving high levels of sensitivity, precision, and accuracy. In SN-ICP-MS, significant progress has been made in characterizing the vaporization, atomization, and ionization patterns of monodisperse droplets. The spatial distribution of ions, resulting from vaporization, atomization, ionization, and diffusion, relative to the sampling cone has a significant impact on detection. Consequently, instrument parameters that influence these key ICP processes, including injector gas flow rates, injector inner diameter, type of injector gas, etc., have also been studied [1]. However, there are significant differences in the aerosol generated during LA and aerosol formed through SN. The PSD of aerosol generated during UV-ns-LA is much broader than traditional SN systems [2-4]. Intuitively, differences in relative penetration depths experienced by nanometer- and micrometer-sized particles would fundamentally limit sampling efficiencies. Attempts to reduce the number of incompletely vaporizing particles would inevitably increase loss due to off-axis diffusion [5]. Given that, for UV-ns-LA, micron-sized particles constitute a large fraction of the total aerosol volume, it is plausible that loss due to off-axis diffusion of ions formed from nanometer-sized particles is trivial [6, 7]. However, because penetration depths depend heavily on ICP conditions and particle composition, reports on threshold sizes for completely vaporizing particles have varied widely [5, 8-11]. The research described here focuses on characterizing the

relative contributions of differently-sized particles to overall ion densities in the ICP.

In chapter 2, high resolution images obtained using LIF were used to investigate the influence of laser fluence, carrier gas, and the presence of water on various ion distributions in the ICP in LA-ICP-MS. Significant contributions to the observed changes in images reported in chapter 2 were suspected to be related to particle size effects. In this chapter, to examine the relative contributions of the various sizes of particle produced during ablation to the resulting distribution of ions formed in the ICP, polycarbonate filters of various pore sizes were placed in-line to selectively remove particles above a given diameter. Contributions of those particle sizes to the overall ion distribution were assigned by comparing images obtained using LIF with different pore size filters in-line. SEM was used to qualitatively characterize the sizes and shapes of particles filtered for each image. Although time consuming, SEM allows very accurate analysis over a large range of particle sizes without limitations characteristic of alternative techniques such as differential mobility analyzers (DMA) and optical particle counters (OPC) [12]. The results indicate that most ions generated in our system originated from micron-sized particles. Differences in penetration depths for nanometer- and micrometer-sized particles were roughly 2 mm, 1 mm, and less than 1 mm for Ca, Ba, and Sc, respectively.

3.2   Experimental

3.2.1   Sample

CaF_2 windows (Exuberance Opto-electronics Technology Co,.Ltd, Beijing, China), BaF_2 windows (Laser Optex, Beijing, China), and 2% scandium-aluminum alloy disks (AMG Aluminum, Robards, KY) were used for the LA studies. The scandium aluminum alloy disks were polished with 1000 grit sandpaper, leaving the surface highly reflective. This was done to

reduce the number of particles generated, especially micron-sized spherical particles, to prevent

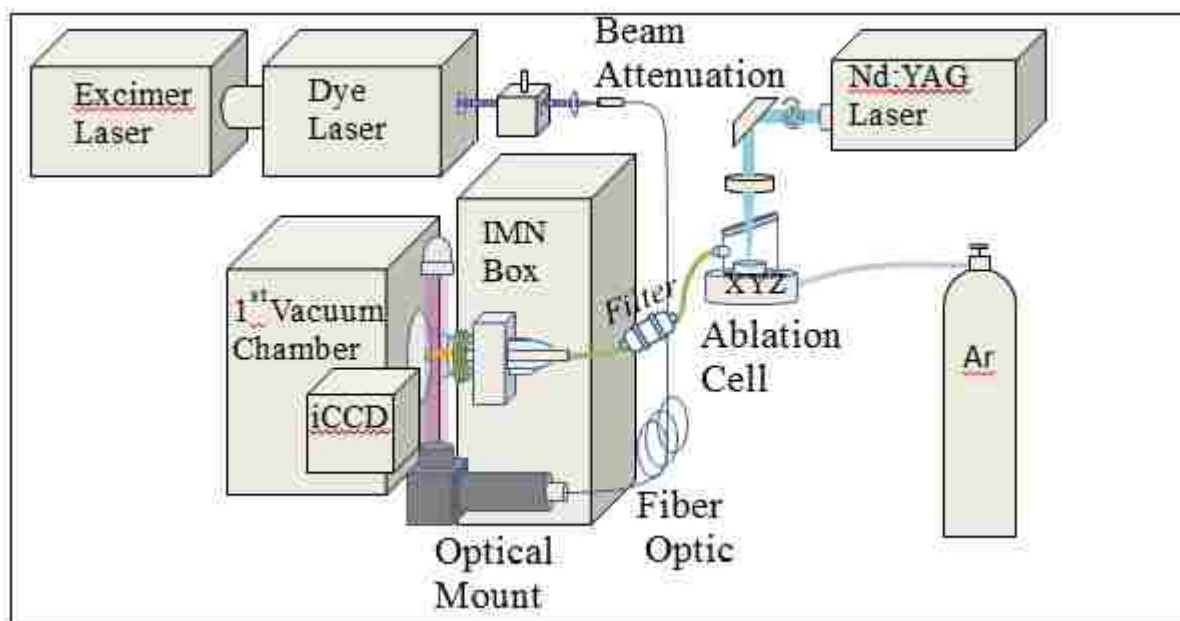clogging of the filters. No pre-ablation was performed on the CaF_2 or BaF_2 windows.

Figure 3.1 General overview of the instrumental setup.

3.2.2   Experimental

Important instrument settings are listed in Table 3.1. A detailed review of the

instrumentation used for these experiments was presented in chapter 2. A brief overview,

including modifications, will be provided here. A modified Varian Redtop ICP-MS (Varian,

Australia) instrument was used. A XeCl excimer laser (LPX 110, Lambda-Physik, Acton, MA)

was used to pump a Scanmate 2 Dye laser (Lambda-Physik, Acton, MA) tuned to a transition

line of the ion being studied. The fluorescence schemes can be found in Table 2.1. The

fluorescence was capture on a gated iCCD (7361-0001, Princeton Instruments, Trenton, NJ). For

Ca and Sc, LIF images were time averaged; hundreds of laser shots were integrated to achieve

acceptable levels of signal to noise within a reasonable exposure time. For Ba, both time-

averaged and single shot images were recorded. For the single shot images, 170 images taken of

fluorescence from a single excitation laser pulse were recorded consecutively to produce a short video.

Pulses from a Nd:YAG laser (Brilliant B, Quantel, France) were used to ablate samples sealed in an ablation cell with a volume of roughly 50 cm^3. All ablation experiments were performed in rastering mode with argon gas flow rates of 1.32, 1.4, and 1.3 L min^{-1} for Sc, Ca, and Ba, respectively. Ablated aerosol was transported through a 2 meter, 7-mm I.D. tygon tube to the sheath torch connector of the ICP. At about 1 meter downstream from the ablation cell, a custom-built filter assembly, with a plastic mesh support ring, was added in-line. No signal loss due to the presence of the mesh support ring was observed. Thin, track-etched, polycarbonate filter disks, 47 mm in diameter, of various pore sizes installed in the filter assembly were used to collect aerosol particles. Because filters with pore sizes below 1 μm were prone to clogging, they could not be used in these experiments. For CaF_2 and scandium aluminum, glass wool was utilized upstream from the filter assembly in lieu of a 1 μm filter. With the glass wool in place, an image was taken with and without a 0.4 μm filter in the filter assembly. Because no ion signals were present with the 0.4 μm pore filter in place, ions formed in the images with the glass wool in-line can be completely assigned to particles collected on the 0.4 μm pore filter. That is, particles below 0.4 μm did not contribute significantly to ion signals. Particles collected on the filter disks were characterized using SEM (Helios NanoLab 600i, Hillsboro, Or). A 10 nm coating of gold and platinum was applied to the surface. SEM settings are displayed within each SEM image. Fig. 3.1 shows the general setup of the instrumentation.

Table 3.1. Experimental conditions

Ablation Laser	Brilliant B
Nd:YAG	266 nm
Pulse length	5 ns
Fluence (Ca/Ba)	18 J cm^{-2}
Fluence (Sc)	50 J cm^{-2}
Spot size	90-120 μm
Rep rate	10 Hz
Raster speed	0.1 mm s^{-1}
Beam profile	Gaussian
ICP-MS	Varian Redtop
Sampling depth	12 mm
ICP forward power	1300 W
Carrier gas	See Text
Plasma gas	16 L min^{-1}
Auxiliary gas	2.0 L min^{-1}
Sheath gas	0.2 L min^{-1}

3.2.3   Image processing

For all but the single shot images, background emission was subtracted from the

corresponding fluorescence images using the Winview software, (Princeton Instrument, Roper

Scientific Inc. Trenton, NJ). Background-subtracted images were converted to ASCII format and

processed with Matlab. The color scales were normalized to each image independently to allow

better qualitative inspection of each ion distribution. Matlab was also used to plot the various

cross sections and FWHMs. Axial cross sections were plotted along the center axis. Five rows

above and below the radial center of the image were summed to improve the signal-to-noise in

the axial profiles, corresponding to a physical dimension of .23 mm. FWHM values were

calculated by counting the total number of pixels with intensity at least half of the peak

maximum. This approach was chosen to avoid calculation difficulties associated with non-

Gaussian peak shapes or significant noise. Matlab was also used to create avi files for the movies

from the single shot experiments. Additionally, relative standard deviations (RSDs) for each

pixel over the 170 images were calculated and used to generate a contour plot.

3.3   Results and discussion

3.3.1   Barium

3.3.1.1   SEM images

SEM images revealed that aerosol generated during ablation of BaF_2 consisted of

irregularly-shaped particles, soft-agglomerates of primary particles, and spherical particles.

Examples of each particle type are presented in Fig. 3.2a. The sizes of soft-agglomerates, which

likely form in the ablation cell [3,13], were difficult to characterize. However, soft-

agglomerations well into the micrometer range, such as the ones pictured in Figs. 3.2b and c,

were common. The sizes of spherical particles were much more readily defined. As seen in Fig.

3.2c, the diameters spherical particles ranged from as low as 100 nm to greater than 1 μm.

Particles larger than 1 μm were mostly irregularly-shaped particles, which often appeared to

have been mechanically ejected, or exfoliated, from the surface, as seen in Fig. 3.2d. However,

large, irregularly-shaped particles that have undergone some melt process, as those in Figs. 3.2e

and f, were also fairly common. Mechanisms likely responsible for producing these large,

irregularly-shaped particles have been described [14,15-16]. The somewhat poor selectivity of

the filters can be seen in, for example, the 8 μm filter shown in Fig. 3.2g. Although particles

below 8 μm were occasionally non-selectively filtered, it is apparent when comparing Fig 3.2g

with the 1 μm filter, shown in Fig. 3.2h, that the filters achieved a fairly high level of
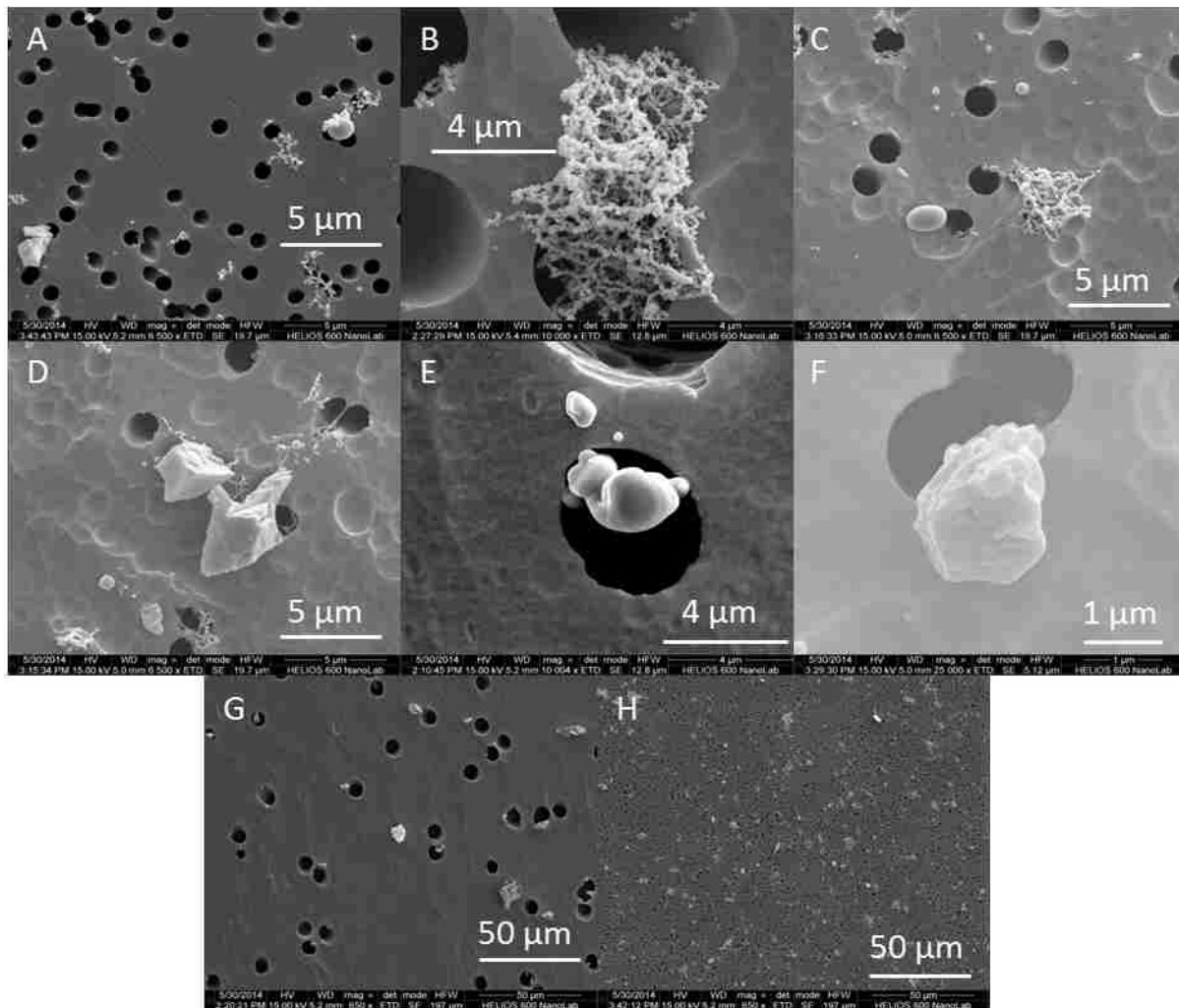
discrimination.

Figure 3.2 SEM images of aerosol particles generated during ablation of BaF$_2$, collected on polycarbonate filter disks with 1, 5, 2, 2, 5, 3, 0.4, and 0.4 μm pore sizes presented in a-h, respectively.

3.3.1.2 LIF images

3.3.1.2.1 Signal intensity

Fluorescence images obtained using various filters are presented in Fig. 3.3a. Cross-sectional plots of the axial distribution of Ba ions along the center axis for each image are presented in Fig. 3.3b. Comparing the images and cross sections taken with different filters in-line yields valuable insights into the relative contribution of various particle sizes to the ion distribution. A 39, 59, 80, 94, and 99% decrease in the peak signal intensity resulted when 8, 5, 3, 2, and 1 μm

filters were added in-line, respectively. Although some particles below 1 μm were filtered by the 1 μm filter, micron-sized particles clearly contributed to the vast majority of ions generated in the ICP.

3.3.1.2.2 Axial ion distribution

In Fig 3.3c, each axial cross section is normalized to its maximum value to more accurately compare changes in the shapes of the axial profiles. Information about the sizes of particles captured on each filter, gained from the SEM images presented in Fig. 3.2 can be used to understand the changes observed in each image.

A 39% decrease in the peak ion signal was observed with the 8-μm filter in-line. Although the selectivity of the filters was poor, practically all of the particles collected on the 8 μm filter were large micron-sized exfoliated particles, many around 5-10 μm in diameter. Removing these particles led to a decrease in the relative ion signal in the downstream tail of the axial cross section displayed in Fig. 3.3c. This suggests that at least the smaller particles filtered by the 8 μm filter were completely vaporized in the ICP. Although the 5-μm filter led to a 59% decrease in the overall ion signal, the axial ion distribution did not change significantly from the 8 μm filter. This is likely due to the large number of 5-8 μm particles non-selectively filtered by the 8 μm filter.

Again, a decrease in the relative ion signal in the downstream tail of the axial cross section accompanied the 80% ion signal decrease associated with the 3 μm filter in-line. This trend was similar for the 2- and 1-μm filters. These trends are consistent with the significant number of irregularly-shaped particles in the range of 1-5 μm. Additionally, there were a large number of spherical particles around 1-2 μm. As large micron-sized particles are more effectively filtered, the relative contributions to the ion signal of particles 1-2 μm and below increases. This is seen

in increasing relative ion intensities on the rise of the peaks in Fig. 3.3c with decreasing pore size.
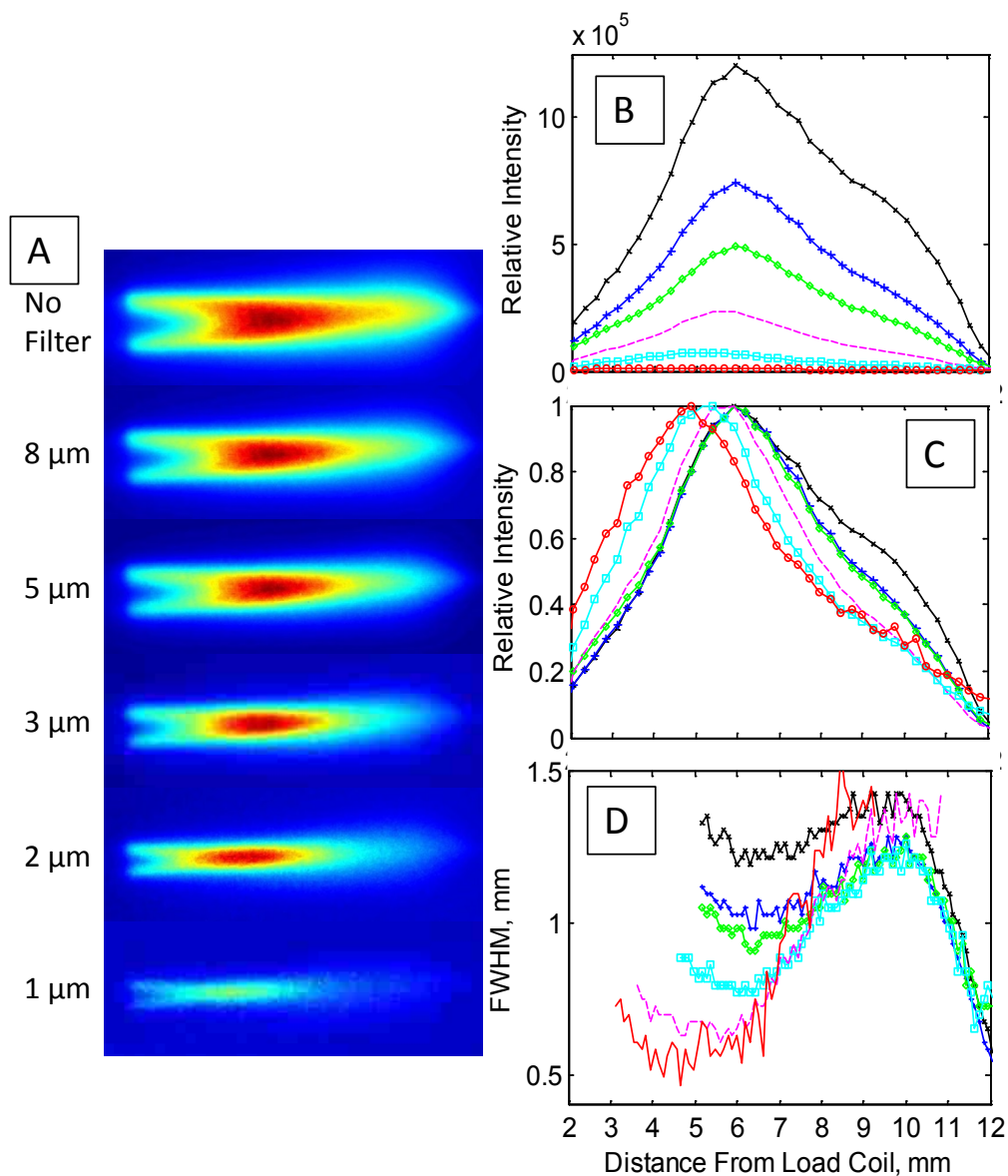
Figure 3.3 LIF images of Ba ion distributions formed in the ICP from aerosol particles generated during LA with filters of various pore sizes, as labelled in (a). Raw (b) and (c) normalized cross-sectional plots of the axial distributions of Ba ions along the center axis for each image. (d) FWHM calculated from radial cross-sections of Ba ion intensities. Legends are as follows: (—x—) no filter, (—+—) 8 μm filter, (—◇—) 5 μm filter, (—□—) 3 μm filter, (— —) 2 μm filter, and (——) 1 μm filter.

3.3.1.2.3 Radial diffusion

To investigate variability in the radial distribution of each image in Fig. 3.3a, FWHM values calculated for each image are plotted in Fig. 3.3d. The decreases in FWHM from upstream positions near the onset of vaporization to the axial position of peak signal intensity likely occurs as vaporization rates exceed rates of diffusion. The increases in FWHM values downstream from the minima towards the sampling cone indicate that diffusion rates overcame vaporization rates. The second decrease just upstream from the sampling cone occurs as ions are focused by gas flow being "pinched" by the sampling orifice.

Interestingly, smaller pore size filters led to significantly smaller FWHM near the axial position of peak ion intensity. Two mechanisms could likely explanation these results: first, initial trajectories of large particles are slightly off-axis compared to smaller particles, or secondly, vaporization patterns of large particles tend towards greater off-axis ion formation compared to smaller particles. To further investigate this phenomenon, LIF images corresponding to a single excitation pulse were taken consecutively to produce a movie. Although the time resolution of the images did not allow a single vaporizing particle to be tracked, the movies provide a general sense of how ion formation evolves in time. Additionally, RSDs for each pixel were calculated from the complete set of images. Contour plots of the RSDs for images taken with no filter and a 1 μm filter are presented in Fig. 3.4a and b, respectively. The largest RSDs with no filter were off-axis and at distances 2-3 mm downstream from the load coil. Also, the RSDs are greater on the lower half of the image. Conversely, RSDs from images taken with a 1 μm filter in-line were mirrored ion densities in the time-averaged image. These results suggest that micron-sized particles are more prone to vaporize off-axis. The asymmetry of

the RSDs is consistent with previous observations in our lab that flow patterns of the carrier gas affect trajectories of particles entering the plasma.
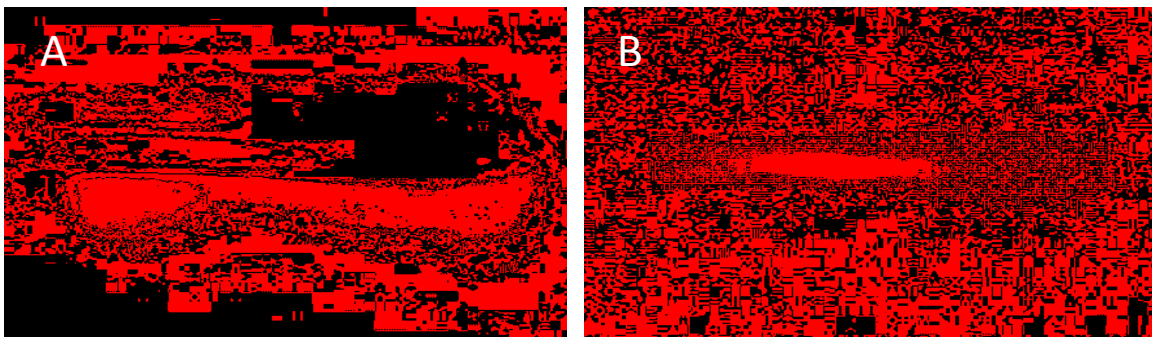

Figure 3.4 Contour plots of RSDs for each pixel calculated over 170 images with no filter (a) and with a 1 μm filter in-line (b). Color scales are different for the two images.

3.3.2 Calcium

3.3.2.1 SEM images

Similar to BaF_2, aerosol generated during ablation of CaF_2 consisted of irregularly-shaped particles, soft-agglomerates of primary particles, and spherical particles (Fig. 3.5a-d). These are consistent with other SEM images of LA generated particles of fluorite reported by Kuhn et al. [3]. However, compared to BaF_2 described in section 3.3.1.1., there were more irregularly-shaped particles in the range of 5-10 μm, such as those shown in Fig. 3.5a and b. Particles collected downstream from the glass wool are shown in Fig. 3.5e. Only small soft-agglomerations passed through the glass wool.
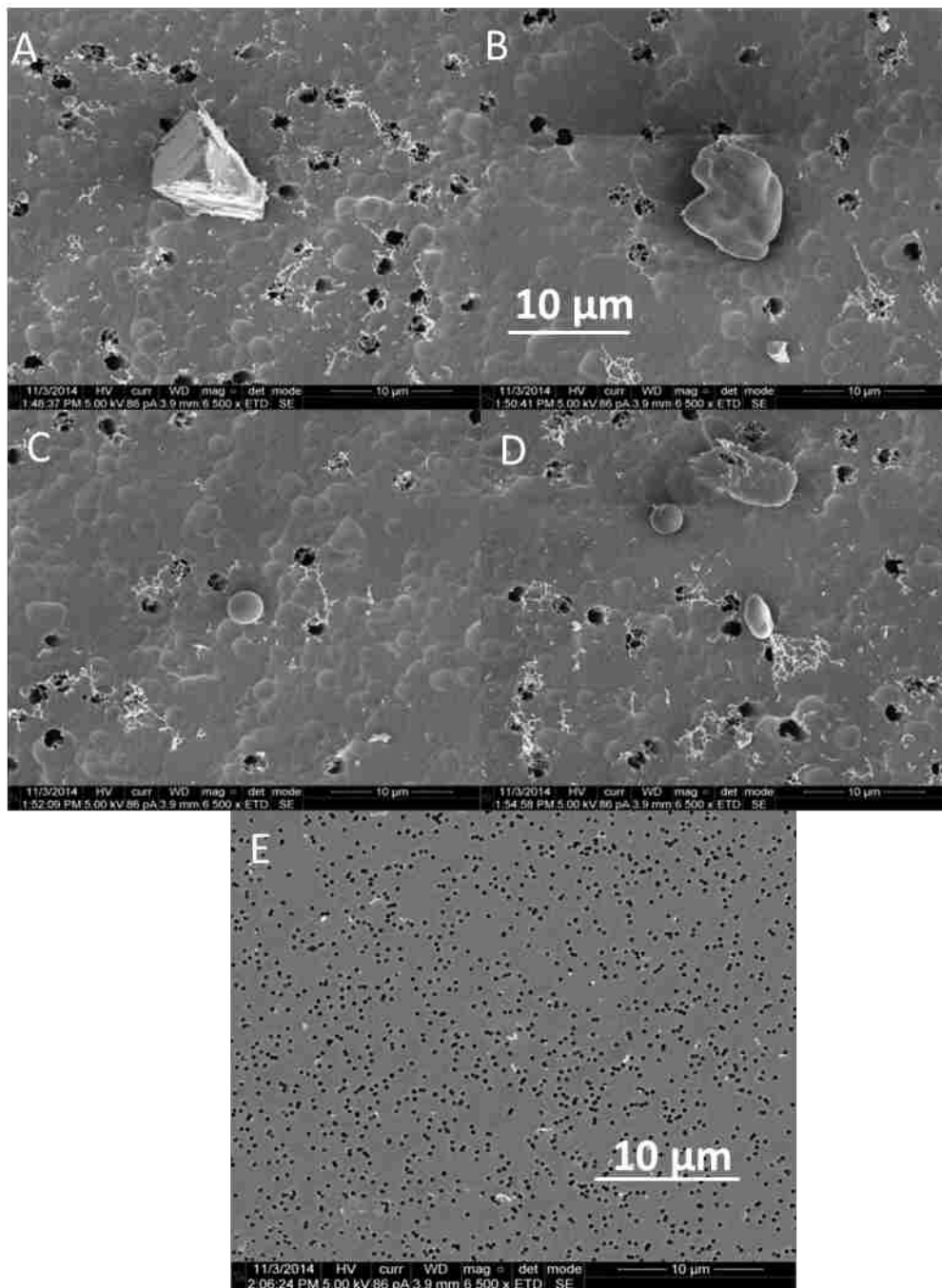
Figure 3.5 SEM images of aerosol particles generated during ablation of CaF$_2$, collected on 2 μm polycarbonate filter disks (a-d). The scaling shown in (b) is the same for (a-d). Particles collected on a 0.4 μm with glass wool added upstream to the transport tubing (e).

3.3.2.2 LIF images

Images obtained using various filters are presented in Fig. 3.6a. The ion densities along the center axis are plotted for each of these images in Fig 3.6b. Results were very similar to BaF_2. A 29, 55, 75, and 92% decrease in the peak signal intensity resulted when placing the 8, 5, 3, and 2 μm pore size filter in-line, respectively. Likewise, a 97% decrease was observed when placing the glass wool upstream from the filter assembly.

Trends in the normalized axial cross section presented in Fig. 3.6c follow much the same patterns as BaF_2. Unlike the 8-μm filter for BaF_2, no significant change in the peak shape was observed for CaF_2. This suggests that the massive irregularly-shaped particles in the 8-10 μm range were not completely vaporized within the axial length imaged. It is an interesting possibility that the decrease in the ion density downstream from the axial position of the signal maximum partly results from a decrease in the rate of ion production associated with decreasing mass of the particle, as suggested by Olesik et al. [11].

Axial cross sections of the 2 μm filter and the glass wool in-line were very similar. This could suggest that very few particles larger than the soft-agglomerates in Fig. 3.6e and smaller than 2 μm were present to contribute to the ion signal. As mentioned in section 3.2.2, because no ion signals were detected with both the glass wool and 0.4 μm pore filter in-line, the signal in the image obtained with just the glass wool present can be assigned to the particles collected on the 0.4 μm filter. Again, this indicates that particles below 0.4 μm do no significantly contribute to the images presented here.

FWHM calculated for the images in Fig. 3.6a are plotted in Fig. 3.6d. Trends in the FWHM values were very similar to BaF_2. Again, smaller pore sizes led to significantly smaller FWHM.

Figure 3.6 LIF images of Ca ion distributions formed in the ICP from aerosol particles generated during LA with filters of various pore sizes in-line, as labelled in (a). Raw (b) and normalized (c) cross-sectional plots of the axial distribution of Ca ions along the center axis for each image. (d) FWHM calculated from radial cross-sections of Ca ion intensities of each image. Legends are as follows: (—x—) no filter, (—+—) 8 μm filter, (—◇—) 5 μm filter, (—□—) 3 μm filter, (— —) 2 μm filter, and (——) glass wool.

3.3.3   Scandium

3.3.3.1   SEM images

Ablation of scandium aluminum led to aerosol consisting of soft- and hard-agglomerates, both

depicted in Fig. 3.7a. Hard-agglomerates were typically micron-sized, whereas soft-agglomerates

were composed of small strands of nanometer-sized particles of varying thickness. Greater

magnifications of the soft- and hard-agglomerates are shown in Fig 3.7b and c, respectively. No

micron-sized spheres or irregularly-shaped particles were observed. This is consistent with

previous reports of ns-LA of metals, particularly at low fluence [16]. Only soft-agglomerates

were present on the 0.4 µm filter added downstream from the glass wool. As with CaF_2, the

signal in the image obtained using the glass wool can be completely ascribed to the particles

collected on the 0.4 µm filter.

Figure 3.7 SEM images of aerosol particles generated during ablation of scandium aluminum, collected on various pore size polycarbonate filter disks. Scales are listed on each image.
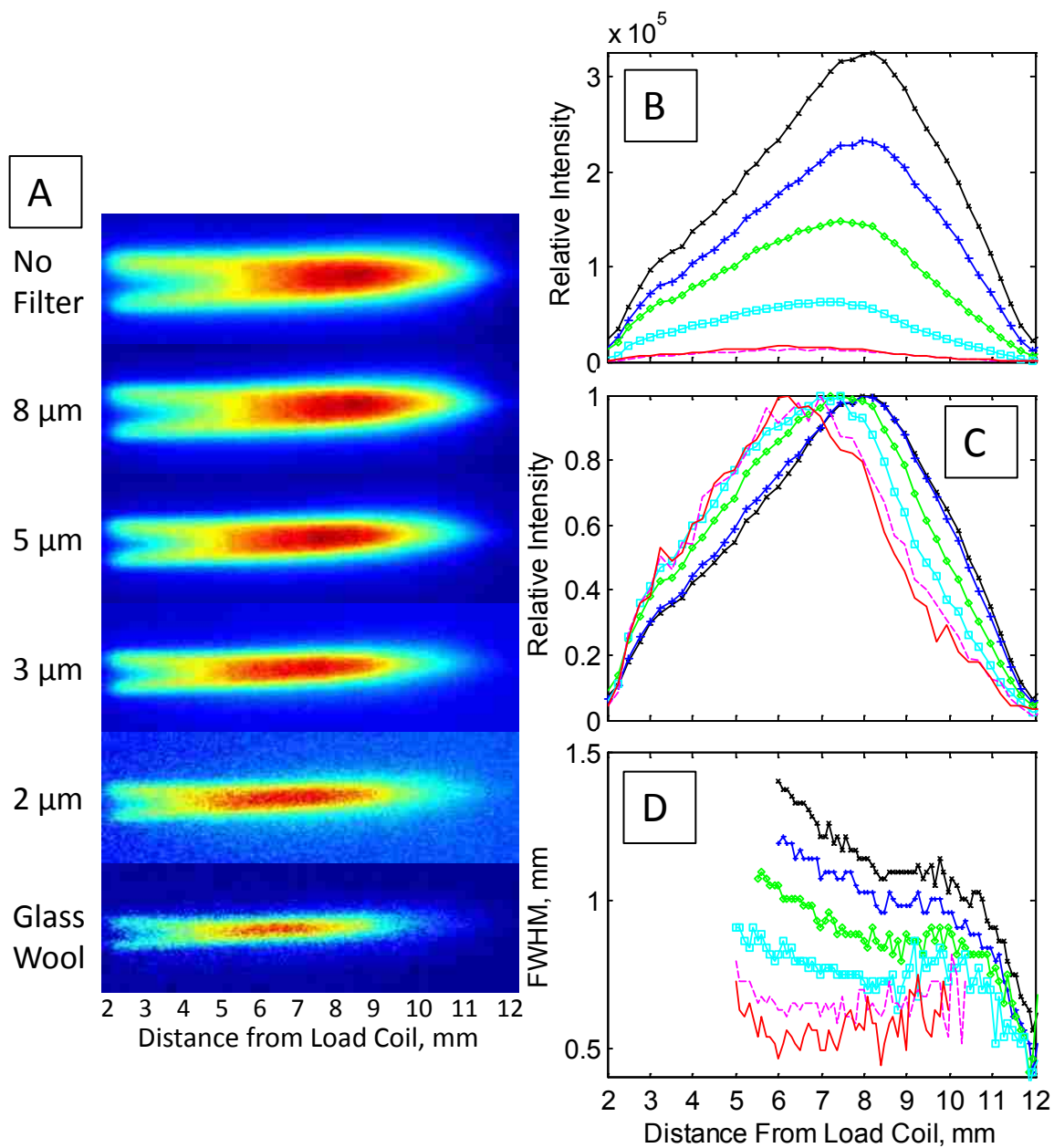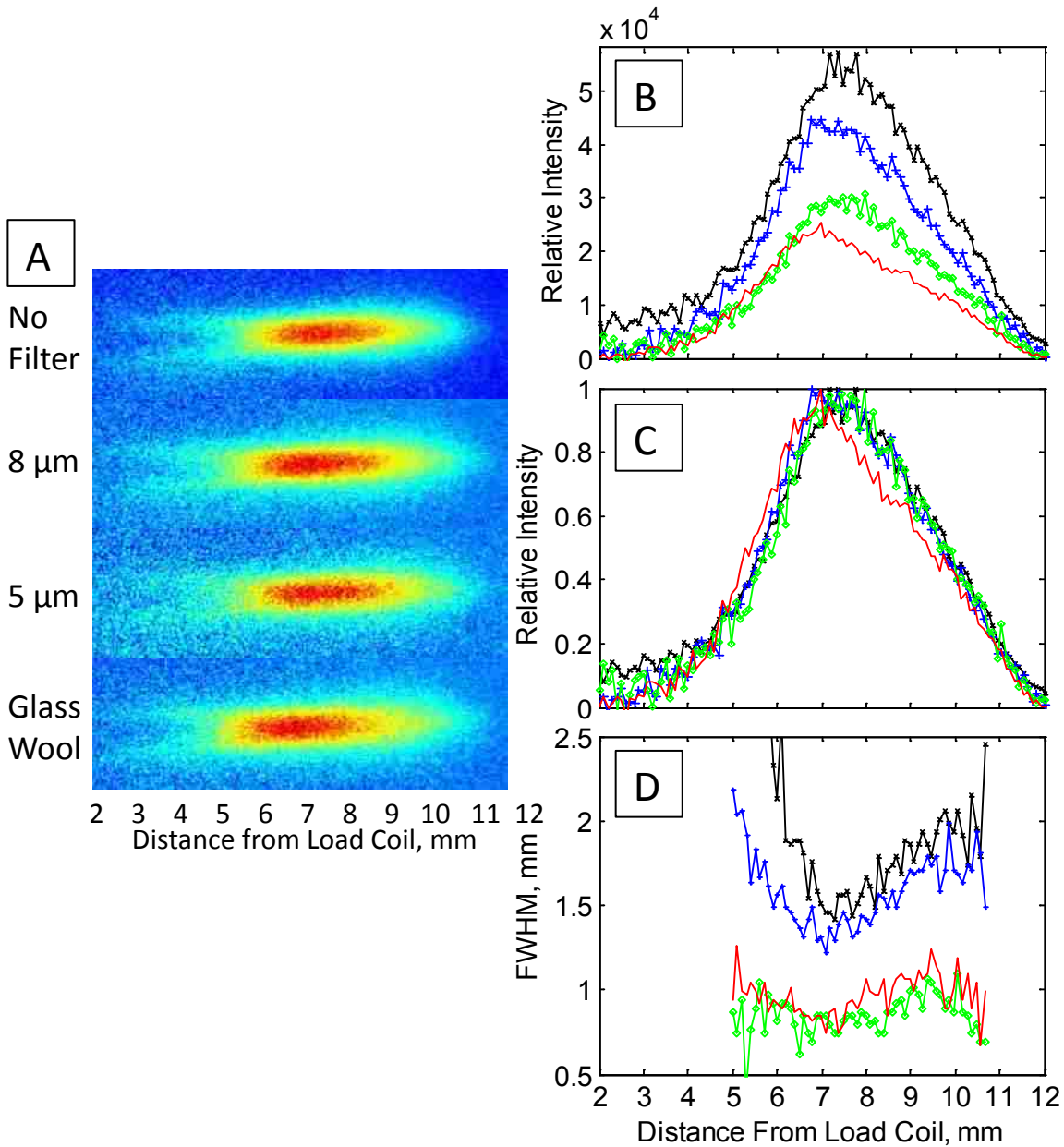
Figure 3.8 LIF images of Sc ion distribution formed in the ICP from aerosol particles generated during LA with filters of various pore sizes, as labelled in (a). Raw (b) and normalized (c) cross-sectional plots of the axial distribution of Sc ions along the center axis for each image. (d) FWHM calculated from radial cross sections of Sc ion intensities from each image. Legends are as follows: (—x—) no filter, (—+—) 8 μm filter, (—◇—) 5 μm filter, and (——) glass wool.

71

3.3.3.2 LIF images

3.3.3.2.1 Signal intensity

LIF images obtained using various filters are presented in Fig. 3.8a. The ion densities along the center axis are plotted for each image in Fig 3.8b. A 22% and 46% decrease in the peak signal intensities resulted when the 8- and 5-µm filters, respectively, were added in-line. Likewise, a 56% decrease occurred with the glass wool added upstream from the filter assembly. These decreases are much less than occurred with either Ba or Ca. This is not surprising considering that only micron-sized hard-agglomerates were generated during LA of scandium aluminum.

3.3.3.2.2 Axial ion distribution

Axial cross sections normalized to their own peak maximum are presented in Fig. 3.8c. There were practically no changes in the relative axial distributions of ions with different filters in-line. Only a slight upstream shift in the relative ion distribution was observed with the glass wool in place. Particles collected on the 0.4 µm filter indicate that only nanometer-sized soft-agglomerates passed through the glass wool. The fact that only a minor decrease in the tail-end of the ion distribution occurred with the glass wool in-line suggests that the micron-sized hard-agglomerates experience very similar vaporization patterns as the smaller nanometer-sized agglomerates. It seems likely that the micron-sized hard-agglomerates largely break up into smaller nanometer-sized agglomerates and only experience slightly greater penetration depths than the soft-agglomerates.

3.3.3.2.3 Radial diffusion

FWHM calculated for the images in Fig. 3.8a are plotted in Fig. 3.8d. Similar to Ca and Ba, FWHM values calculated for images with no filter and an 8 µm filter in-line were significantly

greater than for both the 5 μm filter and glass wool in-line. A steady increase in the FWHM downstream from the FWHM minima, around 6-7 mm from the load coil, support the idea that both soft- and hard-agglomerates break into smaller nanometer-sized particles that rapidly vaporize. If hard-agglomerates experienced greater penetration depths than nanometer-sized soft-agglomerations, we would expect their FWHM minima to occur farther downstream and the subsequent rise to be less pronounced than that of the soft-agglomerates.

3.3.4 Penetration depths

Differences in the axial position of peak ion signals for each image can be used to estimate differences in penetration depths of the particle sizes contributing to the image. A clear upstream shift in the axial position of peak ion densities occurred for both Ba and Ca with decreasing filter pore size. Based on the differences in the axial position of peak ion signals, relative differences in the penetration depths of particles around 8 μm and particles below 1 μm were about 2 mm for Ca and 1 mm for Ba. Alternatively, only minor differences in the penetration depths of micron-sized hard-agglomerates and nanometer-sized soft-agglomerates occurred with Sc. Given that significant decreases in the ion intensity occurred with no accompanying change in the axial ion distribution, we consider it unlikely that observed shifts were caused by reduced cooling of large micron-sized particles removed.

3.4 Conclusions

The relative contributions to ion densities in the ICP of differently-sized particles were examined. Particle sizes were characterized off-line with SEM. Aerosols generated during LA of BaF_2 and CaF_2 consisted of soft-agglomerates, spherical particles, and irregularly-shaped particles, whereas only soft- and hard-agglomerates were generated from ablation of scandium aluminum. In all cases, micron-sized particles produced most of the ions formed in the ICP. For

Ba and Ca, differences in axial positions of peak ion signal of 2- and 1- mm, respectively, were observed between nanometer- and micron-sized particles. Differences in the penetration depths of nanometer-sized soft-agglomerates and micron-sized hard-agglomerates observed in the case of scandium aluminum were much less significant. We conclude that the soft- and hard-agglomerates generated during ablation of scandium aluminum experience very similar vaporization patterns in the ICP. There was evidence that flow patterns in the transport tube influence the trajectories of aerosol particles entering the ICP. The results described here address significant gaps in the current literature regarding vaporization patterns of LA aerosol of broad PSD, such as is common with 266 nm-ns-LA.

3.5 References

[1] K. Niemax, Considerations about the detection efficiency in inductively coupled plasma mass spectrometry, Spectrochim. Acta, Part B, 76 (2012) 65-69.
[2] J.J. Gonzalez, C. Liu, S.-B. Wen, X. Mao, R.E. Russo, Metal particles produced by laser ablation for ICP-MS measurements, Talanta, 73 (2007) 567-576.
[3] H.-R. Kuhn, D. Gunther, The agglomeration state of nanosecond laser-generated aerosol particles entering the ICP, Anal Bioanal Chem, 383 (2005) 434-441.
[4] J.J. Gonzalez, C. Liu, S.B. Wen, X. Mao, R.E. Russo, Glass particles produced by laser ablation for ICP-MS measurements, Talanta, 73 (2007) 577-582.
[5] L. Flamigni, J. Koch, D. Günther, Experimental and theoretical investigations about the vaporization of laser-produced aerosols and individual particles inside inductively-coupled plasmas — Implications for the extraction efficiency of ions prior to mass spectrometry, Spectrochimica Acta Part B: Atomic Spectroscopy, 76 (2012) 70-76.
[6] M. Guillong, H.-R. Kuhn, D. Gunther, Application of a particle separation device to reduce inductively coupled plasma-enhanced elemental fractionation in laser ablation-inductively coupled plasma-mass spectrometry, Spectrochim. Acta, Part B, 58B (2003) 211-220.
[7] M. Guillong, D. Gunther, Effect of particle size distribution on ICP-induced elemental fractionation in laser ablation-inductively coupled plasma-mass spectrometry, Journal of Analytical Atomic Spectrometry, 17 (2002) 831-837.
[8] H.-R. Kuhn, D. Günther, Elemental Fractionation Studies in Laser Ablation Inductively Coupled Plasma Mass Spectrometry on Laser-Induced Brass Aerosols, Analytical Chemistry, 75 (2003) 747-753.
[9] J.W. Olesik, N. Casey, Investigation of vaporization of laser ablation generated aerosol and monodisperse particles in a dry Ar ICP using time-resolved mass spectrometry, Spec. Publ. - R. Soc. Chem., 301 (2005) 164-174.
[10] K.-S. Ho, K.-O. Lui, K.-H. Lee, W.-T. Chan, Considerations of particle vaporization and analyte diffusion in single-particle inductively coupled plasma-mass spectrometry,

Spectrochimica Acta Part B: Atomic Spectroscopy, 89 (2013) 30-39.

[11] J.W. Olesik, P.J. Gray, Considerations for measurement of individual nanoparticles or microparticles by ICP-MS: determination of the number of particles and the analyte mass in each particle, J. Anal. At. Spectrom., 27 (2012) 1143-1155.

[12] H.-R. Kuhn, J. Koch, R. Hergenroeder, K. Niemax, M. Kalberer, D. Guenther, Evaluation of different techniques for particle size distribution measurements on laser-generated aerosols, J. Anal. At. Spectrom., 20 (2005) 894-900.

[13] P. Dewalle, J. Vendel, J.-M. Weulersse, P. Herve, G. Decobert, Influence of Carrier Gas Flow Rate, Laser Repetition Rate, and Fluence on the Size Distribution and Number of Nanoparticles Generated Per Laser Shot During Paint Laser Ablation, Aerosol Science and Technology, 45 (2011) 1429-1440.

[14] V. Craciun, D. Craciun, M.C. Bunescu, R. Dabu, I.W. Boyd, Scanning electron microscopy investigation of laser ablated oxide targets, Journal of Physics D: Applied Physics, 32 (1999) 1306.

[15] R. Hergenroder, Laser-generated aerosols in laser ablation for inductively coupled plasma spectrometry, Spectrochimica Acta Part B-Atomic Spectroscopy, 61 (2006) 284-300.

[16] R.E. Russo, X. Mao, J.J. Gonzalez, V. Zorba, J. Yoo, Laser Ablation in Analytical Chemistry, Analytical Chemistry, 85 (2013) 6162-6177.

4   THE EFFECTS OF HE ON ABLATION AND ICP ENVIRONMENT IN LA-ICP-MS

This chapter has been submitted for publication in Spectrochimica Acta Part B

4.1   Introduction

LA-ICP-MS is a powerful technique used for trace elemental analysis of solids. Compared to traditional SN, LA is quasi non-destructive, offers greater spatial resolution and sensitivity, and requires little to no sample preparation. However, non-stoichiometric effects related to laser-, transport-, and ICP-induced elemental fractionation significantly limit the analytical capabilities of LA-ICP-MS when matrix-matched standards are unavailable [1]. The need for better methods to reduce or account for elemental fractionation drives much of the research devoted to LA-ICP-MS. In this effort, the use of helium as carrier gas has led to significant improvements in LA-ICP-MS performance. However, improvements in MS data likely result from a convolution of helium effects during ablation, transport, and ICP processes, including transport through the interface.

In chapter 2, the effects of adding helium to argon gas upstream of the ablation cell on ion distributions in the ICP using LIF were described. We were surprised to find that helium added to the carrier gas led to a decrease in the overall ion densities within the ICP. We considered the possibility that changes in the PSD could account for the decreased ion count in the ICP. However, the PSD of aerosol generated with ns-LA at 266 nm is considered largely immune to the choice of carrier gas [2]. Additionally, reduced deposition around ablation craters [3] and improved transport efficiencies of aerosol [2] for 266 nm ns-LA-ICP-MS during ablation in He vs Ar have been reported. Furthermore, minor increases in the fraction of small particles in the presence of helium typically lead to sensitivity gains [2, 4]. Witte et al. [5] reported 50% gains in MS signals when adding He. We concluded that more efficient transport through the interface in the presence of helium could account for the apparent inconsistency of the decreased ion signal

we observed with improved sensitivities generally reported. Significant improvements in ion signals achieved with more efficient ion transmission through the interface have been reported [6-7]. In this chapter, I describe a series of follow-up studies performed to test conclusions drawn in chapter 2.

4.2 Experimental

4.2.1 Sample

CaF$_2$ windows (Exuberance Opto-electronics Technology Co,.Ltd, Beijing, China) and 2% scandium-aluminum alloy disks (AMG Aluminum, Robards, KY) were used for this study. The 2% scandium-aluminum alloy disks were polished with 2000 grit sandpaper. No pre-ablation was performed on the CaF$_2$ windows.

4.2.2 Experimental

Important instrument settings are listed in Table 4.1. A detailed review of the instrumentation used for these experiments have been presented in chapter 2. A brief overview, including modifications to the instrumentation described in chapter 2, will be provided here. Pulses from a Nd:YAG laser (Brilliant B, Quantel, France) were used to ablate samples sealed in an ablation cell with a volume of roughly 50 cm^3. The Varian ICP-MS gas box was used to control the Ar gas flow supply to the ablation cell. A separate mass flow controller (5850, Brooks Instruments) was used to control the He gas flow. Flow from either controller could be directly connected upstream of the ablation cell, added downstream of the ablation cell via a "Y"-connector, or mixed upstream of the ablation cell by a swage "T"-connector. A 7-mm I.D. transport tube (Tygon) was used to carry particles to the sheath torch connector of the ICP. Ratios of approximately 25, 50, and 75% He/Ar, listed in Table 4.2, were chosen that either led

to ion distributions centered in the imaging region or reaching a maximum near the sampling cone.

After the images were taken for each gas condition, a filter assembly built in-house was added in-line midway from the ablation cell to the ICP torch. For each gas condition, particles generated over 100 laser pulses were collected on 0.4 μm polycarbonate filter disks. Particles collected on the filters were characterized with SEM (Helios NanoLab 600i, Hillsboro, Or). A 10 nm coating of gold and platinum was applied to the surface. Images were taken at 650x magnification with power of 5.00 KV, current of 86 pA, and working distances around 4 mm.

A XeCl excimer laser (LPX 110, Lambda-Physik, Acton, MA) was used to pump a SCAN mate 2 Dye laser (Scanmate 2, Lambda-Physik, Acton, MA) tuned to a transition line for the ion being studied. The fluorescence schemes can be found in Table 2.1. Fluorescence was captured on a gated iCCD (7361-0001, Princeton Instruments, Trenton, NJ). The iCCD gain and number of exposures were adjusted to produce acceptable signal levels within a reasonable exposure time. Fig. 4.1 shows the general setup of the instrumentation.
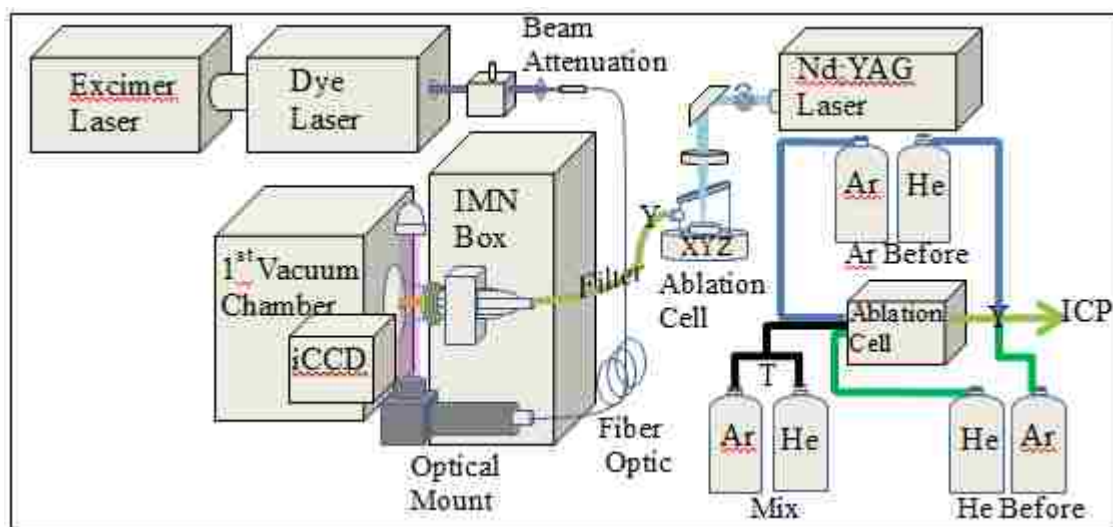

Figure 4.1 General overview of the instrumental setup. The three different setups used for the different gas conditions are depicted.

Table 4.1 Experimental conditions	
Ablation Laser	*Brilliant B*
Nd:YAG	266 nm
Pulse length	5 ns
Fluence (Sc)	50 J cm^{-2}
Fluence (Ca)	18 J cm^{-2}
Spot size	90 μm
Rep rate	10 Hz
Raster speed	0.1 mm s^{-1}
Beam profile	Gaussian
ICP-MS	*Varian*
Redtop	
Sampling depth	12 mm
ICP forward power	1300 W
Carrier gas	See Table 4.2
Plasma gas	16 L min^{-1}
Auxiliary gas	2 L min^{-1}
Sheath gas	0.2 L min^{-1}

Table 4.2 Carrier Gas Flow Rates (L min^{-1})				
He/Ar Ratio		*25%*	*50%*	*75%*
Ca II	Ar	1.3	1.05	0.66
	He	0.43	1.05	2
Sc II	Ar	1.17	1	0.58
Fig 4.6	He	0.39	1	2
Sc II	Ar	1.28	1.1	0.72
Fig 4.8	He	0.42	1.1	2

4.2.3   Image processing

The background emission was subtracted from the corresponding fluorescence image using the Winview software, (Princeton Instrument, Roper Scientific Inc. Trenton, NJ). Background-subtracted images were converted to ASCII format and processed with Matlab. The color scales were normalized to each image independently to allow greater qualitative inspection of each ion distribution. Matlab scripts were created to plot the various cross sections and FWHMs. Axial

cross sections were plotted along the center axis. Five rows above and below the radial center axis, corresponding to a physical dimension of .23 mm, were averaged to improve the signal-to-noise in the axial profiles. FWHM values were calculated by counting the total number of pixels along each radial cross section with intensity at least half of the peak maximum. This approach was chosen to avoid calculation difficulties associated with non-Gaussian peak shapes or significant noise. FWHM were not calculated at axial positions where the presence of the cooled central channel caused a dip in the ion signal along the center axis.

4.3 Results and discussion

4.3.1 Calcium

4.3.1.1 Ablation

As seen in the SEM image in Fig. 4.2a, ablation in 1.3 L min^{-1} Ar produced spherical particles, exfoliated fragments, and soft-agglomerates of various sizes and densities. Images of these particles taken at greater magnifications were presented in chapter 3. Particles collected during ablation at 0.66 L min^{-1} Ar, presented in Fig. 4.2b, include micron-sized spheres, exfoliated particles, and filamentary soft agglomerates. Due to the scarcity of micron-sized particles, the exfoliated particle seen in the inset was superimposed from another section of the image. Insets in the remaining images are similarly drawn from other sections of the filter to illustrate the variety of particles collected on the filter.

Much larger and denser soft-agglomerations were generated during ablation in 2.00 L min^{-1} He (Fig. 4.2c) compared to either flow rate in Ar. Hard-agglomerates, spheres, and fragments, though smaller, were present in numbers similar to 1.3 L min^{-1} Ar. The numbers and sizes of soft-agglomerates formed at 0.43 L min^{-1} He (Fig. 4.2d) were intermediate between those formed in Ar and those observed with 2.00 L min^{-1} He. Only a few small micron-sized spheres and

fragments were observed during ablation in 0.43 L min^{-1} He. We assume that the changes in

particle distributions observed as a function of gas flow rates are primarily due to changes in

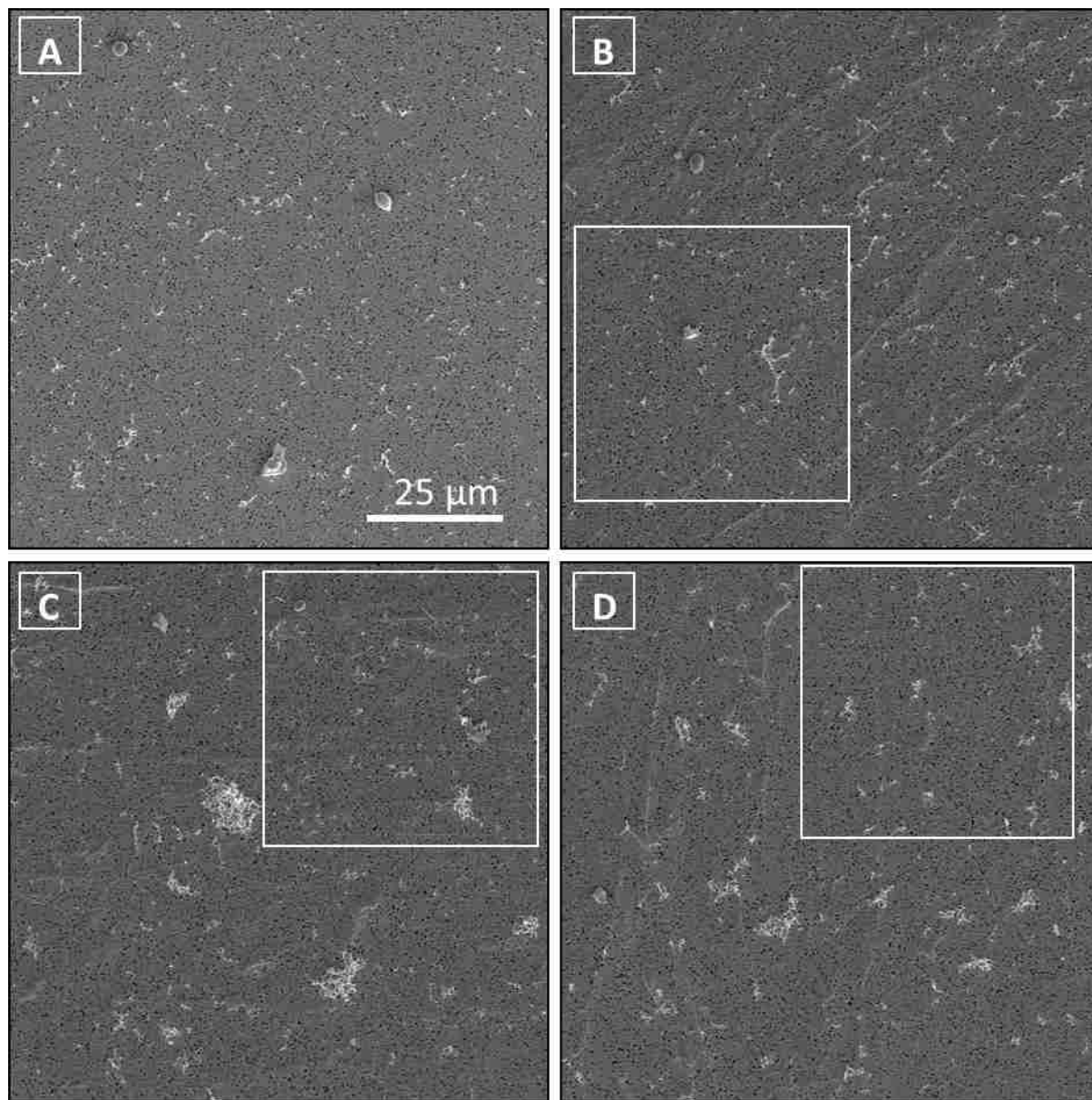transport efficiency, and not due to fundamental changes in the ablation process.

Figure 4.2 SEM images of aerosol particles, generated during ablation of CaF$_2$, impacted on 0.4 μm pore size polycarbonate filter disks. Images were taken of particles impacted during ablation in 1.3 L min^{-1} Ar (a), 0.66 L min^{-1} Ar (b), 2.00 L min^{-1} He (c), and 0.43 L min^{-1} He (d). These flows correspond to the flows used for images presented in Fig. 4.3 for ablation in argon or helium at 25 and 75% He/Ar. The scale for each image, bottom-right of (a), is the same for each image.

4.3.1.2 ICP

4.3.1.2.1 Axial ion distributions

General qualitative differences in the ion distributions formed during ablation in different Ar/He gas conditions are presented in the LIF images in Fig 4.3. The intensities of ions along the center axis for each image are plotted in the axial cross-sections in Fig. 4.4a, b, and c for He/Ar mixtures of 25, 50, and 75%, respectively. For each He/Ar ratio, the gas composition in the ablation cell had little effect on the overall ion signal intensities, despite differences in the PSDs described in section 4.3.1.1. It appears that the increase in the amount of soft-agglomerations during ablation in helium compensated for the reduced size and number of micron-sized particles compared to argon. This is consistent with reports of identical ablation rates in helium and argon [8]. Although overall intensities were similar, some differences in the ion distributions were evident for the 25% He/Ar mixture. The shape of the trace for ablation in argon is consistent with the vaporization pattern for large particles, in contrast to the pattern expected for the filamentary particles that dominate in Fig. 2d. In general, however, it can be said that the effects of ablation gas on ion distributions for CaF_2 are minor.

In contrast, the overall composition of the gas has a major impact on ion distributions in the plasma. The ion signal intensity for 75% He/Ar is about a half that for 25% He/Ar. These results are consistent with the results described in chapter 2. Given that a greater number of micron-sized particles and agglomerates were observed during ablation in 2.00 L min^{-1} He compared to 0.43 L min^{-1} He, particle effects do not account for the decrease. In addition to affecting aerosol production, increasing He/Ar ratios also influence ICP conditions [9]. Higher gas-kinetic temperatures have been reported with added helium [5]. At higher gas-kinetic temperatures, the ionization efficiency of the ICP should improve and unfavorable shifts in the Saha balance are

not likely [10]. Enhanced off-axis diffusion of ions at higher He/Ar ratios could account for lower on-axis signals. Broadening in the radial distributions of ions in the presence of He, previously reported, were attributed to higher mass and electrical conductivities of helium compared to argon [11],[12]. Moreover, an upstream shift in the axial position where vaporization begins [13] at higher He/Ar ratios would exacerbate ion loss due to off-axis diffusion. The disappearance of the cooled central channel at 75% He/Ar in the LIF images in Fig. 4.3 is indicative of an upstream shift in vaporization. An upstream shift in vaporization was suggested to account for a decrease in LIF signal that occurred when adding a matrix element (lithium) in a SN-ICP-MS study [14].
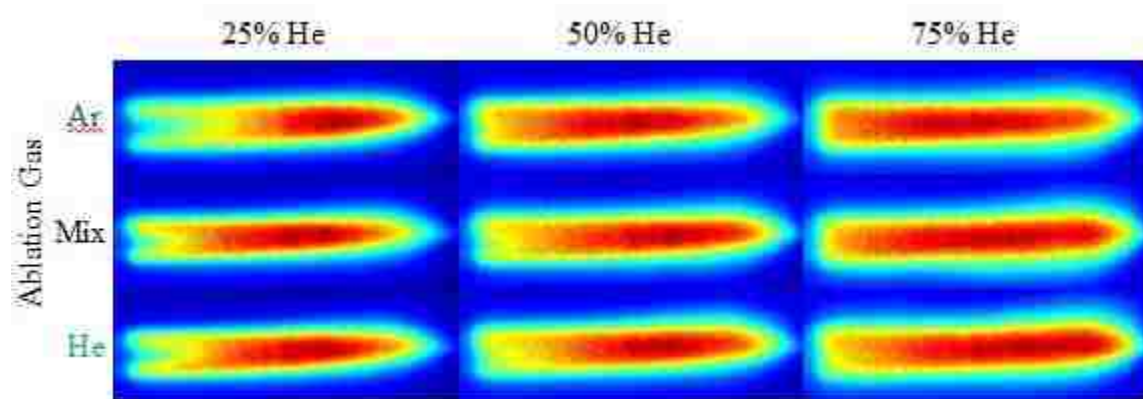

Figure 4.3 LIF images of Ca ion distributions formed in the ICP from aerosol particles generated during LA in various ablation gas conditions. As labelled, images were obtained during ablation in 25 (left column), 50 (center column), and 75% He/Ar (right column). For each He/Ar ratio, argon (top row), a mixture of argon and helium (middle row), or helium (bottom row) was added to the ablation cell. Actual flow rates used for each image are listed in Table 4.2. Each image is oriented similarly with the load coil out of the image to the left and the sampling cone just protruding into the right side.
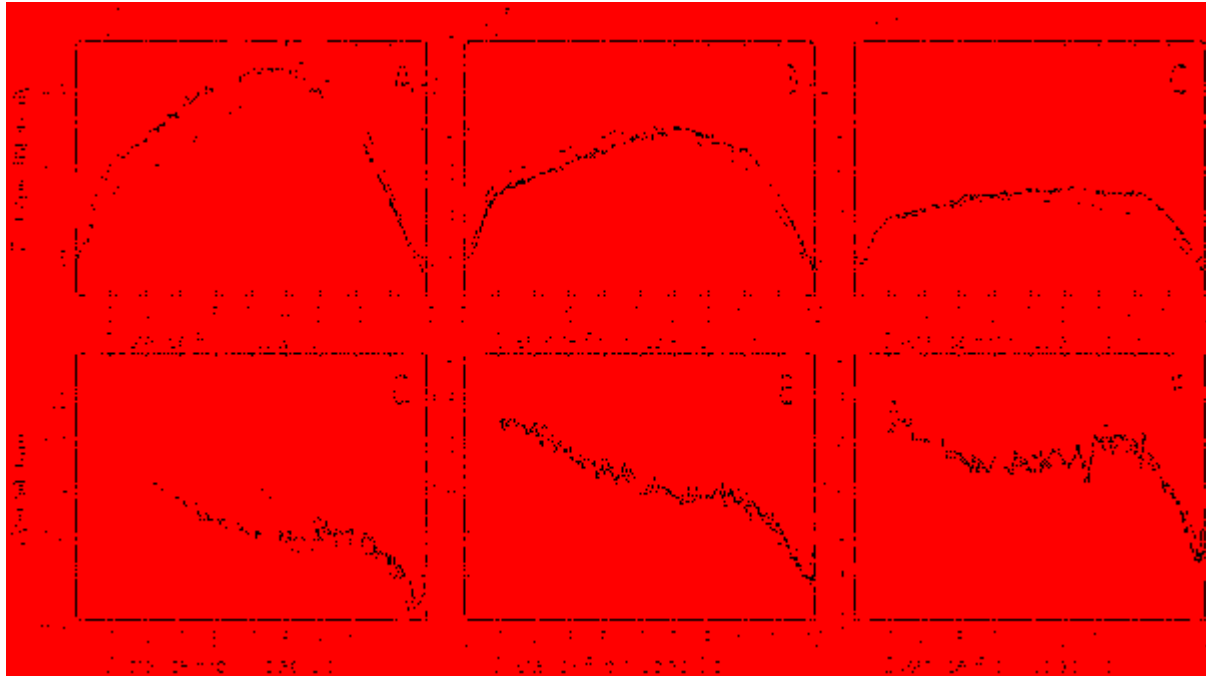
Figure 4.4 Cross-sectional plots of the axial distribution of Ca ions along the center axis for each image presented in Fig. 4.3. Plots from images taken with nebulizer gas compositions of 25, 50, and 75% He/Ar are presented in 4.4a, b, and c, respectively. Additionally, FWHM calculated from radial cross-sections of Ca ion intensities are presented in 4.4d, e, and f, for nebulizer gas compositions of 25, 50, and 75% He/Ar, respectively. For each He/Ar ratio, plots are presented for ablation in (– –) argon, (——) mixtures, and (——) helium.

4.3.1.2.2 Radial ion distributions

FWHMs calculated from radial cross sections of images taken during ablation in 25, 50, and 75% He/Ar are presented in Fig. 4.4d, e, and f, respectively. Higher He/Ar ratios produced significantly larger FWHM values, most notably at downstream positions near the sampling cone. The general trend of FWHM values along the axial length was similar for each plot. The initial decline in the FWHM to a minimum indicates that vaporization rates exceed rates of off-axis diffusion. A vaporizing particle acts as a local source of atoms, which are ionized faster than they diffuse off-axis. A minimum and subsequent rise occurs as rates of off-axis diffusion exceed vaporization rates. At higher He/Ar ratios, the axial positions where the minima occur are shifted

upstream. The upstream shift is consistent with an upstream shift in the axial position where vaporization begins. However, higher vaporization rates [4] could also contribute to the shift.

4.3.2 Scandium

4.3.2.1 Ablation

As seen in the SEM image in Fig. 4.5a, ablation in 1.3 L min^{-1} Ar produced micron-sized hard-agglomerates, spherical particles, and soft-agglomerates of various densities. Fewer spheres and more hard-agglomerates were generated compared to CaF_2. Ablation in 0.6 L min^{-1} Ar (Fig. 4.5b) led to more abundant, larger soft-agglomerates compared to 1.3 L min^{-1} Ar. No micron-sized spheres or fragments were observed at the lower flow rate.

Micron-sized spheres and hard-agglomerates were collected during ablation in 2.00 L min^{-1} He (Fig. 4.5c), though smaller and fewer in number compared to 1.3 L min^{-1} Ar. Soft-agglomerations were more abundant and appeared to be more densely packed than those formed in Ar. During ablation in 0.4 L min^{-1} He (Fig. 4.5d) soft-agglomerations were formed, though not as dense or abundant as at 2.00 L min^{-1} He. There were no micron-sized particles collected during ablation in 0.4 L min^{-1} He. Chimney formations attributed to inefficient removal of large particles during ablation have been reported for metals [8], so the absence of large particles at low He flow rates in the ablation cell could be due to transport losses. However, the presence of large particles under similar conditions with the CaF_2 samples indicates that other factors are also in play.
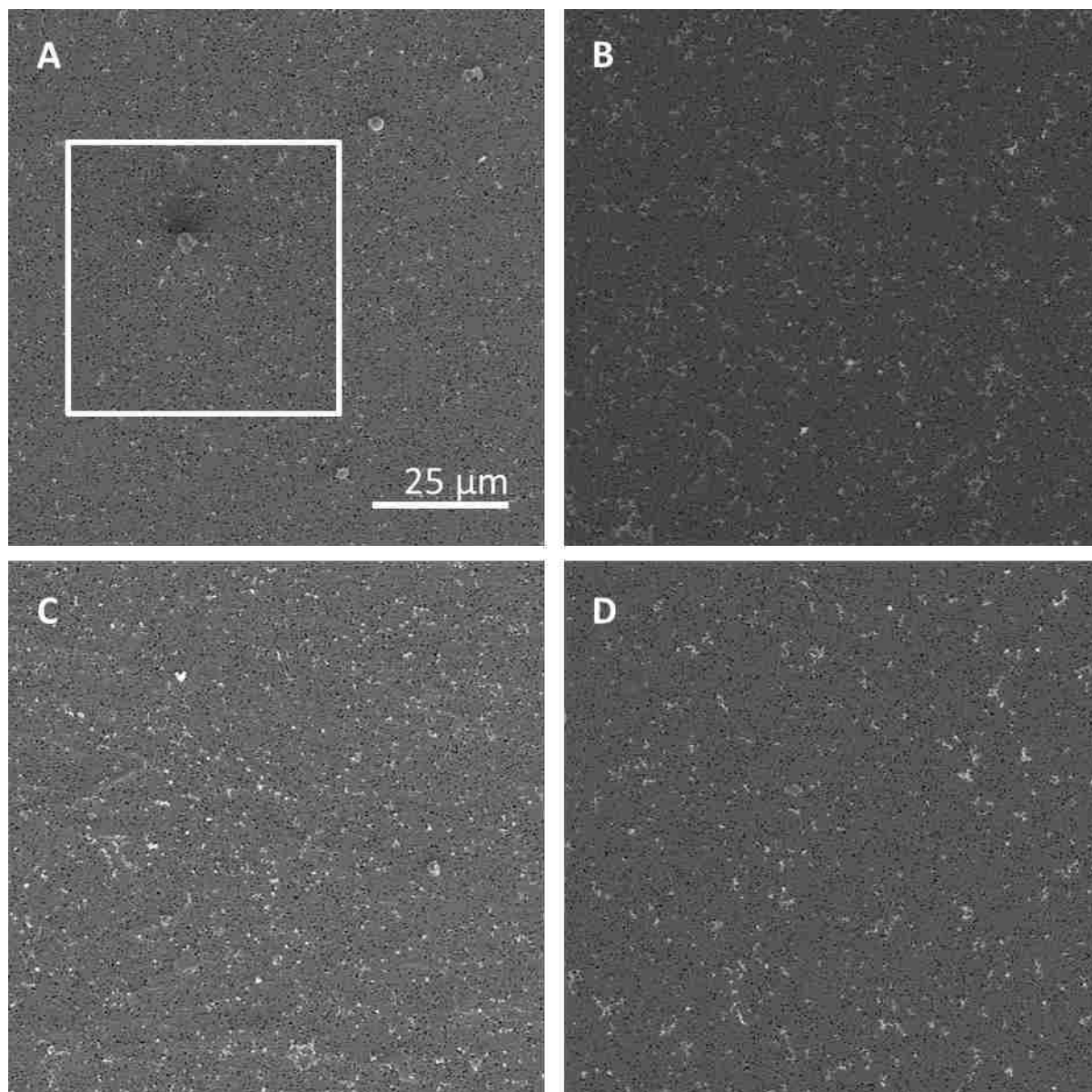
Figure 4.5 SEM images of aerosol particles, generated during ablation of scandium aluminum, impacted on 0.4 μm pore-size polycarbonate filter disks. Images were taken of particles impacted during ablation in 1.3 L min^{-1} Ar (a), 0.6 L min^{-1} Ar (b), 2.00 L min^{-1} He (c), and 0.4 L min^{-1} He (d). These flows reflect nominal flows used for images presented in Fig. 6 and 8 for ablation in argon or helium at 25 and 75% He/Ar.
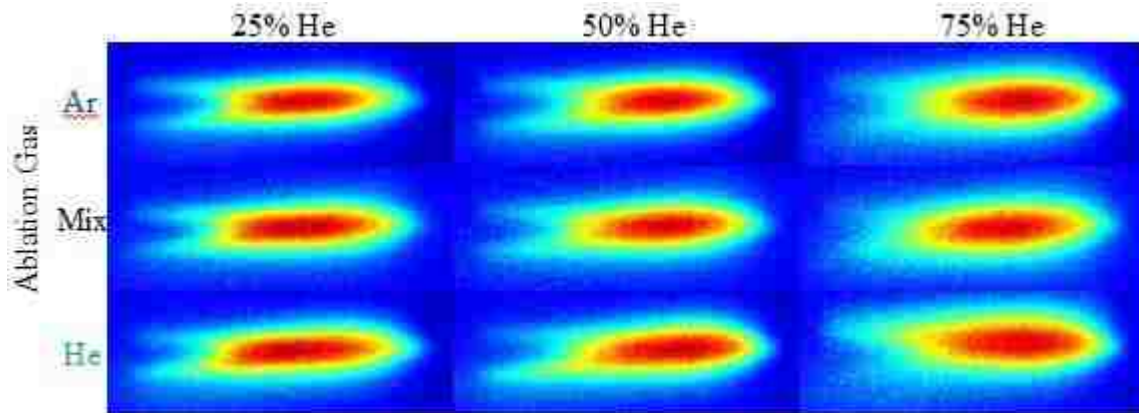
Figure 4.6 LIF images of Sc ion distributions formed in the ICP from aerosol particles generated during LA in various ablation gas conditions. As labelled, images were obtained during ablation in 25 (left column), 50 (center column), and 75% He/Ar (right column). For each He/Ar ratio, argon (top row), a mixture of argon and helium (middle row), or helium (bottom row) was used added to the ablation cell. Actual flow rates used for each image are listed in Table 4.2.
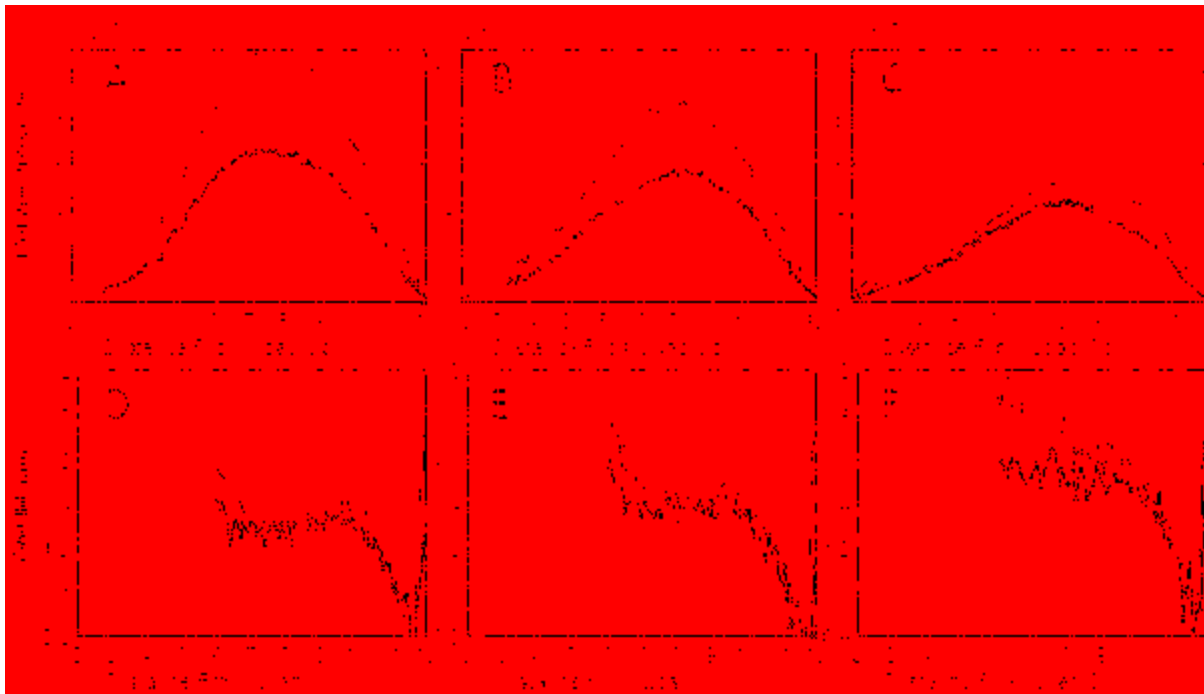

Figure 4.7 Cross-sectional plots of the axial distribution of Sc ions along the center axis for each image presented in Fig. 4.6. Plots from images taken during ablation in 25, 50, and 75% He/Ar are presented in 4a, b, and c, respectively. Additionally, FWHM calculated from radial cross-sections of Sc ion intensities are presented in 4.7d, e, and f, for ablation in 25, 50, and 75% He/Ar, respectively. For each He/Ar ratio, plots are presented for ablation in (– –) argon, (——) mixtures, (——) and helium.

4.3.2.2 ICP

4.3.2.2.1 Axial ion distributions

LIF images of Sc ions taken during various ablation gas conditions are presented in Fig. 4.6. Gas flows were chosen that led to peak ion densities 7-8 mm downstream from the load coil. Cross sections of the ion densities along the center axis are plotted for 25, 50, and 75% He/Ar in Fig. 4.7a, b, and c, respectively. Unlike the case of CaF_2, overall ion signal intensities were significantly dependent on ablation gas composition for the scandium aluminum alloy, most notable at lower He/Ar ratios. It is clear from the data that ion densities in the plasma are not a simple linear function of the composition of the gas in the ablation cell, as would be the case if gas density were the critical gas property.

The ion signals produced with 75% He/Ar are approximately half those for 25% He/Ar when either He or Ar is used as the ablation gas. As with CaF_2, the decrease is not consistent with changes in the PSD. Rather, ICP effects must be considered. Again, off-axis diffusion could account for the decrease in ion density with the increase in helium content in the nebulizer gas. Since calcium and scandium are almost identical in mass, they should experience very similar rates of diffusion. However, the plateauing effect observed in the ion signal for CaF_2 at greater He/Ar ratios did not occur in scandium aluminum. Scandium is a much more refractory element than calcium. Recalling that lower nebulizer gas flow rates lead to higher central channel temperatures, note that the Sc ion density with an Ar flow rate of 1.17 L min^{-1} peaked at the same axial position as Ca ion density with a flow of 1.3 L min^{-1} Ar. It is possible that the plateauing effect in the Ca ion distribution observed for high helium fractions was related to the upstream shift in vaporization and is not as significant for the more refractory scandium aluminum particles.

4.3.2.2.2 Radial ion distributions

FWHMs calculated from vertical cross sections of images taken during ablation in 25, 50, and 75% He/Ar are presented in Fig. 4.7d, e, and f, respectively. Similar to Ca, FWHMs increased with increasing He/Ar ratios. It is interesting that the FWHM continually decreased along the axial length for 75% He/Ar, indicating that particles vaporized along the entire axial length of the ICP. It should be noted that the axial position of peak ion signal for 75% He/Ar is 1 mm downstream from that of that of 25% He/Ar. Therefore, it is possible that diffusional effects are masked by convergence of the gas flow at the sampling cone. It is also possible that an "expansion-driven acceleration" of particles in 75% He/Ar led to incomplete vaporization of larger particles [15]. Higher velocities would mean aerosol particles would experience shorter residence times in the ICP. Incomplete vaporization not only accounts for the FWHM trend, but could also account for a portion of the decreased ion signal that occurred with 75% He/Ar.

4.3.2.2.3 Sampling cone

To investigate the influence of the vacuum interface on ion distributions in different He/Ar mixtures, flow rates were adjusted to produce peak ion densities just upstream from the sampling cone. LIF images of Sc ions taken at those flow rates are presented in Fig. 4.8. Cross sections of the ion densities along the center axis are plotted for 25, 50, and 75% He/Ar in Fig. 4.9a, b, and c, respectively. At 25% He/Ar, ablation in argon again leads to the greatest ion signal. However, at 50 and 75% He/Ar, ablation in helium produces the largest ion signal. It is unlikely that significant changes in the PSD occurred over the minor changes in flow rates required to shift the ion signal towards the sampling cone. Thus changes in the vaporization/ionization rates of particles near the sampling cone should be considered.

The evidence suggests that more complete vaporization of soft-agglomerates, predominately generated in helium, compared to micron-sized particles, generated in argon, account for the change in trend. Because flow rates were increased to position the Sc ion signal peak just upstream from the sampling cone, particles vaporize over a shorter axial length and are less likely to completely vaporize. Indeed, FWHM plotted in Fig 4.9d, e, and f, for 25, 50, and 75% He/Ar indicate incomplete vaporization in all cases. Intuitively, the vaporization efficiency of soft-agglomerates would be less affected by accelerated velocities associated with greater He/Ar ratios than micron-sized particles. An increased steepness in the decline of FWHMs corresponding to ablation in helium compared to argon is further support of this conclusion.
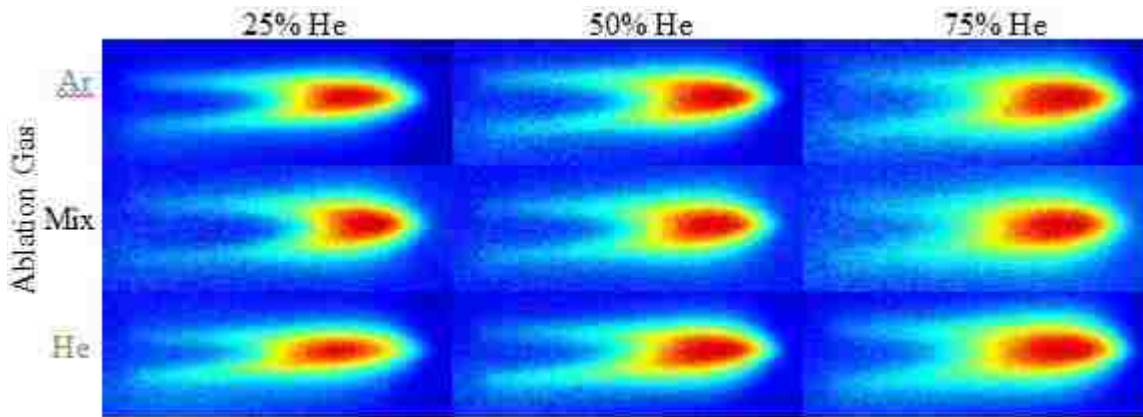

Figure 4.8 LIF images of Sc ion distributions formed in the ICP from aerosol particles generated during LA with gas flows adjusted to produce peak ion signals 2-3 mm upstream from the sampling cone. As labelled, images were obtained during vaporization in 25 (left column), 50 (center column), and 75% He/Ar (right column). For each He/Ar ratio, argon (top row), a mixture of argon and helium (middle row), or helium (bottom row) flowed through the ablation cell. Actual flow rates used for each image are listed in Table 4.2.
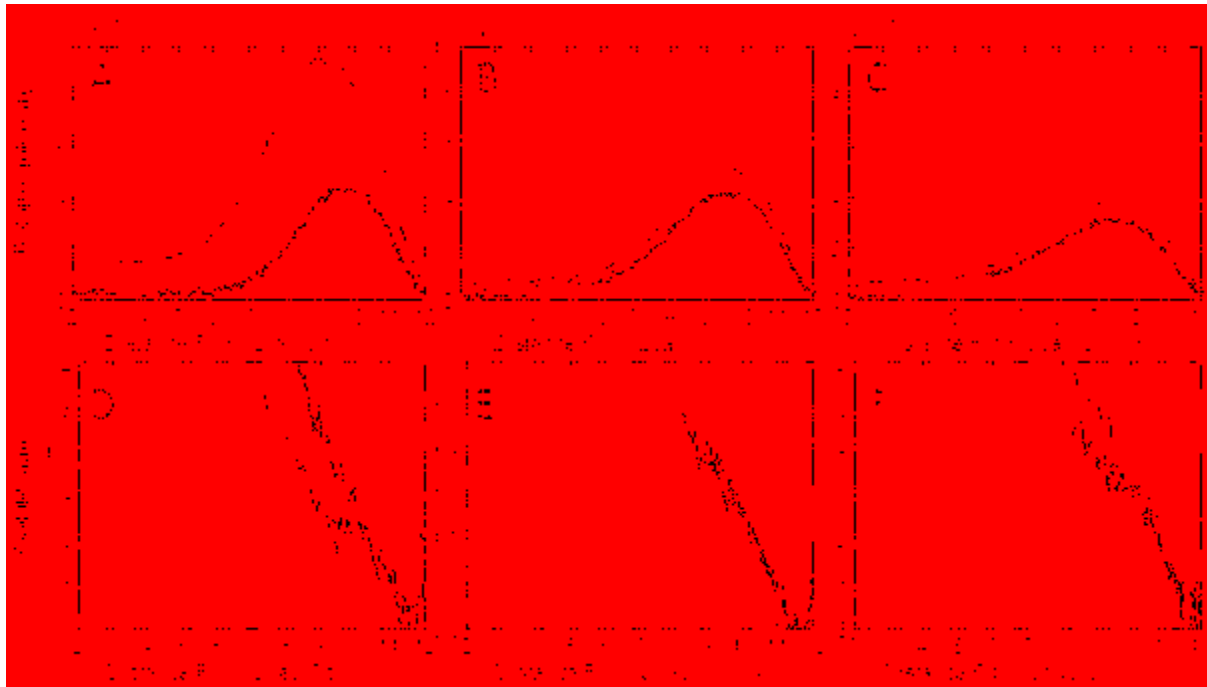
Figure 4.9 Cross-sectional plots of the axial distribution of Sc ions along the center axis for each image presented in Fig. 4.8. Plots from images taken with nebulizer gas compositions of 25, 50, and 75% He/Ar are presented in 4.9a, b, and c, respectively. Additionally, FWHM calculated from radial cross-sections of Ca ion intensities are presented in 4.9d, e, and f, for nebulizer gas compositions of 25, 50, and 75% He/Ar, respectively. For each He/Ar ratio, plots are presented for ablation in (— —) argon, (——) mixtures, and (——) helium.

4.4   Conclusions

The effects of adding helium upstream and downstream of the ablation cell were investigated. Differences in the PSD of aerosol generated during ablation in argon and helium at low and high flows were characterized off-line with SEM. In general, ablation in helium led to larger, more densely packed soft-agglomerates, and fewer and smaller micron-sized particles than in argon. However, Ca ion signals generated from particles produced during ablation of CaF_2 were largely independent of the gas added upstream from the ablation cell. It seemed that an increase in the amount of soft-agglomerations during ablation in helium compensated for the reduced size and number of micron-sized particles compared to argon. In the case of scandium aluminum, ablation in argon typically led to larger Sc ion signals in the ICP. For both CaF_2 and

91

scandium aluminum, increasing the He/Ar ratio from 25 to 75% led to lower ion densities.

Changes in the PSD could not account for the decrease. We propose that increased rates of off-axis diffusion at greater He/Ar ratios caused the decrease. Increasing FWHM values at higher He/Ar ratios supported this conclusion. When flow rates were increased to shift ion production near the sampling cone, slightly higher Sc ion signals were formed from particles generated in helium than in argon. We concluded that the vaporization efficiencies of soft-agglomerates were less affected by accelerated particle velocities at greater He/Ar ratios than micron-sized particles.

4.5   References

[1] R.E. Russo, X. Mao, J.J. Gonzalez, V. Zorba, J. Yoo, Laser Ablation in Analytical Chemistry, Analytical Chemistry, 85 (2013) 6162-6177.
[2] I. Horn, D. Gunther, The influence of ablation carrier gasses Ar, He and Ne on the particle size distribution and transport efficiencies of laser ablation-induced aerosols: implications for LA-ICP-MS, Appl. Surf. Sci., 207 (2003) 144-157.
[3] D. Gunther, C.A. Heinrich, Comparison of the ablation behavior of 266 nm Nd:YAG and 193 nm ArF excimer lasers for LA-ICP-MS analysis, J. Anal. At. Spectrom., 14 (1999) 1369-1374.
[4] Z. Wang, B. Hattendorf, D. Guenther, Analyte Response in Laser Ablation Inductively Coupled Plasma Mass Spectrometry, J. Am. Soc. Mass Spectrom., 17 (2006) 641-651.
[5] T.M. Witte, R.S. Houk, Origins of polyatomic ions in laser ablation-inductively coupled plasma-mass spectrometry: An examination of metal oxide ions and effects of nitrogen and helium in the aerosol gas flow, Spectrochim. Acta, Part B, 69 (2012) 9-19.
[6] L. Lin, Z. Hu, L. Yang, W. Zhang, Y. Liu, S. Gao, S. Hu, Determination of boron isotope compositions of geological materials by laser ablation MC-ICP-MS using newly designed high sensitivity skimmer and sample cones, Chemical Geology, 386 (2014) 22-30.
[7] C. Latkoczy, D. Gunther, Enhanced sensitivity in inductively coupled plasma sector field mass spectrometry for direct solid analysis using laser ablation (LA-ICP-SFMS), Journal of Analytical Atomic Spectrometry, 17 (2002) 1264-1270.
[8] I. Horn, M. Guillong, D. Gunther, Wavelength dependant ablation rates for metals and silicate glasses using homogenized laser beam profiles - implications for LA-ICP-MS, Applied Surface Science, 182 (2001) 91-102.
[9] H. Lindner, A. Bogaerts, Multi-element model for the simulation of inductively coupled plasmas: Effects of helium addition to the central gas stream, Spectrochimica Acta Part B: Atomic Spectroscopy, 66 (2011) 421-431.
[10] H. Niu, R.S. Houk, Fundamental aspects of ion extraction in inductively coupled plasma mass spectrometry, Spectrochimica Acta Part B: Atomic Spectroscopy, 51 (1996) 779-815.
[11] Z. Wang, B. Hattendorf, D. Guenther, Vaporization and ionization of laser ablation generated aerosols in an inductively coupled plasma mass spectrometer-implications from ion distribution maps, J. Anal. At. Spectrom., 21 (2006) 1143-1151.
[12] N.N. Sesi, A. Mackenzie, K.E. Shanks, P. Yang, G.M. Hieftje, Fundamental studies of

mixed-gas inductively coupled plasmas, Spectrochimica Acta Part B: Atomic Spectroscopy, 49 (1994) 1259-1282.

[13] L. Flamigni, J. Koch, D. Günther, Experimental and theoretical investigations about the vaporization of laser-produced aerosols and individual particles inside inductively-coupled plasmas — Implications for the extraction efficiency of ions prior to mass spectrometry, Spectrochimica Acta Part B: Atomic Spectroscopy, 76 (2012) 70-76.

[14] A.A. Mills, J.H. Macedone, P.B. Farnsworth, High resolution imaging of barium ions and atoms near the sampling cone of an inductively coupled plasma mass spectrometer, Spectrochimica Acta Part B: Atomic Spectroscopy, 61 (2006) 1039-1049.

[15] L. Flamigni, J. Koch, H. Wiltsche, R. Brogioli, S. Gschwind, D. Guenther, Visualization, velocimetry, and mass spectrometric analysis of engineered and laser-produced particles passing through inductively coupled plasma sources, J. Anal. At. Spectrom., 27 (2012) 619-625.

5 CONCLUSIONS

5.1 Summary

5.1.1 Fluorescence imaging of ion distributions in an inductively coupled plasma with laser ablation sample introduction

In chapter 2, I compared the spatial distributions of ions generated from aerosol produced during SN with aerosol produced during LA under varying fluence and carrier gas make-up. "Dry" aerosol produced during LA, which did not require desolvation, led to ions formed farther upstream in the plasma compared to "wet" aerosol produced during SN. Broader axial distributions of ions formed from LA generated aerosols, compared to SN aerosol, were attributed to broad particle size distributions produced by LA. Although LA generated aerosol led to narrower radial distributions than SN, I was unable to explain the difference. However, I found that laser fluence positively correlated with the radial width of the ion distribution. In preliminary experiments, solvent added independent of the analyte had very little effect of the ion profile beyond shifting it slightly downstream. The addition of He to the nebulizer gas flow led to reduced ion signals at axial positions farther upstream in the plasma compared to pure Ar as the nebulizer gas at a given total flow rate. It was difficult to distinguish between He effects related to changes in the PSD or ICP environment.

5.1.2 Evaluation of particle size distributions produced during ultra-violet nanosecond laser ablation and their relative contributions to ion densities in an ICP

In chapter 3, I characterized the relative contributions to ion densities in the ICP of particles of various sizes. Particles observed using SEM consisted of hard- and soft- agglomerates, spherical particles, and irregularly-shaped particles. Although soft-agglomerates and spherical particles were common to aerosols generated during LA of glass and metals, hard-agglomerates

94

appeared to be unique to metals while irregularly-shaped particles were unique to glass. For glass and metals, a significant fraction of the ions formed in the ICP originated from micron-sized particles. Based on differences in the axial position of peak ion signal, differences in the penetration depths of nanometer-sized agglomerates and micron-sized particles were about 2 mm for Ca and 1 mm for Ba. Differences in the penetration depths of nanometer and micron-sized agglomerates observed in the case of aluminum scandium were much less significant. This suggests that micron-sized hard-agglomerates and nanometer-sized soft-agglomerates experience very similar vaporization patterns. Additionally, there was evidence that flow patterns in the transport tube affect the trajectories of particles entering the plasma.

5.1.3   Differentiating the effects of He on ablation and ICP environment in LA-ICP-MS

In chapter 4, I investigated the effects of adding helium upstream and downstream of the ablation cell. Using SEM, I found that ablation in helium generally led to larger, more densely packed soft agglomerates, and fewer and smaller micron-sized particles than in argon. Ca ion signals generated from particles produced during ablation of CaF_2 were largely independent of the gas added upstream from the ablation cell. It seemed that an increase in the amount of soft-agglomerations during ablation in helium compensated for the reduced size and number of micron-sized particles compared to argon. In the case of scandium aluminum, ablation in argon typically led to greater Sc ion signals in the ICP. For both Ca and Sc, increasing the He/Ar ratio from 25 to 75% led to lower ion signals. Changes in the PSD could not account for the decrease. It was proposed that increased rates of off-axis diffusion at greater He/Ar ratios caused the decrease. Increasing FWHM at higher He/Ar ratios supported this conclusion. When flow rates were increased to shift ion production near the sampling cone, larger Sc ion signals were formed from particles generated in helium. I speculated that the vaporization efficiencies of soft-

agglomerates were less affected by accelerated particle velocities at greater He/Ar ratios than micron-sized particles.

5.2   Future work

Very little research on vaporization patterns of LA generated aerosol has been published. Consequently, there are a large number of worthwhile experiments that could be performed with little to no modifications to the existing instrumental setup. In the course of developing methods for the experiments described in this paper, I noticed a number of interesting phenomena that could be studied further. 1) The focus position of the Nd:YAG relative to the sample surface had a tremendous influence on the ion signal. 2) The reflectivity of the scandium aluminum surface, which varied greatly depending on the sandpaper grit used for polishing, heavily influenced ablation rates, particles formed, and the resulting LIF ion signal. 3) The time evolution of ions forming in the plasma as ablation begins and the decrease during the wash-out after ablation ends showed interesting characteristics. For example, helium led to significantly shorter wash-out times than argon. 4) The presence of the filter assembly or Y connector downstream from the ablation cell appeared to cause distributions of ions over larger radial distances. Overall, I suspect flow patterns through the transport tube influences the MS signal more than is currently thought. 5) Varying laser fluence affected the LIF ion signal differently for ablation in Ar vs. He.

There are a number of interesting experiments that would require some modifications to the instrumental setup. 1) It would be interesting to image ions formed from LA aerosol in the first and second vacuum chambers. Changes in transmission patterns between argon and Ar/He mixed plasmas would help clarify results we observed using helium. 2) It would be very instructive if particles of only a narrow size range could be transported to the ICP. The filters used in my studies could only filter particles below a certain size and were not very selective at that. 3) It

96

would not take a great deal of modifications to perform experiments similar to the ones described here operating the Nd:YAG at the first and second harmonics, 1064 nm and 532 nm. These fundamental studies are key to improving the analytical capabilities of LA-ICP-MS